UNIVERSITY OF Southampton

University of Southampton Research Repository

University of Southampton

Faculty of Physical Sciences and Engineering

Optoelectronics Research Centre

High Power Pulsed Thulium Doped Fibre Lasers And Their Applications

by

Sijing Liang

Thesis for the degree of Doctor of Philosophy

May 2019

ABSTRACT

HIGH POWER PULSED THULIUM DOPED FIBRE LASERS AND THEIR APPLICATIONS

By Sijing Liang

This thesis presents the development of a high-peak-power, gain-switched diode-seeded, thulium doped fibre master oscillator power amplifier (MOPA), along with its various applications in nonlinear frequency conversion.

To exploit the peak power scalability of a large-mode-area (LMA) thulium doped fibre (TDF), a three-stage MOPA structure was first demonstrated to produce 1-MHz, 52-ps pulses with a maximum average/peak output power of 3.94 W/76 kW. A four-stage configuration was proposed to enhance the overall nonlinear threshold of the system, thereby scaling the pulse peak power to a higher level. Eventually, 35-ps pulses with a record-breaking peak power of 295 kW and a maximum average output power of 10.34 W were obtained from this nearly all-fibre thulium doped fibre MOPA system.

The presented high-peak-power thulium doped fibre MOPA systems were used to demonstrate stable and flexible laser sources with a combined operation window from the visible to the mid-infrared. 2-µm-pumped supercontinuum (SC) generation in fluoride fibres has demonstrated an ultra-broadband spectral output from 750 nm to 5 µm with a total output power of 1.76 W. Frequency up-conversion of the high-power thulium doped fibre MOPA was also investigated based on periodically-poled-lithium-niobate (PPLN). Maximum output powers of 2.4 W and 0.69 W were achieved in second harmonic generation (SHG) and fourth harmonic generation (FHG), respectively. Besides, an optical parametric generator (OPG) and an optical parametric amplifier (OPA) based on orientation-patterned GaAs (OP-GaAs) were demonstrated to produce signal and idler pulses with wide wavelength-tuning ranges from 2550 nm to 2940 and from 5800 nm to 8300 nm, respectively.

Table of Contents

List of Tables

List of Figures

List of Abbreviations

AR	Anti-reflection
ASE	Amplified spontaneous emission
CPA	Chirped pulse amplifier
CR	Cross relaxation
CSA	Communication signal analyser
CW	Continuous wave
DBR	Distributed Bragg reflector
DC	Direct current
DCA	Digital communications analyser
DFG	Difference-frequency generation
DW	Dispersive wave
EDFA	Erbium doped fibre amplifier
EOM	Electro-optic modulator
ESA	Excited state absorption
EYFL	Erbium and ytterbium co-doped fibre laser
FBG	Fibre Bragg grating
FHG	Fourth harmonic generation
FP	Fabry-Perot
FSR	Free spectral range
FWHM	Full width half maximum
FWM	Four-wave mixing
GVD	Group velocity dispersion
HDFA	Holmium doped fibre amplifier
HDFL	Holmium doped fibre laser
HWP	Half-wave plate
LIDAR	Light detection and ranging
LMA	Large-mode-area
LPF	Long pass filter
MA	Mode adaptor

MFD	Mode field diameter
MI	Modulation instability
MOPA	Master oscillator power amplifier
NA	Numerical aperture
NLS	Nonlinear Schrödinger equation
OSA	Optical spectrum analyser
OSNR	Optical signal-to-noise ratio
OPA	Optical parametric amplifier
OPG	Optical parametric generator
OPO	Optical parametric oscillator
OP-GaAs	Orientation-patterned GaAs
PC	Polarisation controller
PCF	Photonic crystal fibre
PER	Polarisation extinction ratio
PPLN	Periodically poled lithium niobite
QPM	Quasi phase-matching
RF	Radio-frequency
SC	Supercontinuum
SFG	Sum-frequency generation
SHG	Second harmonic generation
SMSR	Side mode suppression ratio
SPM	Self-phase modulation
SSFS	Soliton self-frequency shift
TDFA	Thulium doped fibre amplifier
TDFL	Thulium doped fibre laser
TEC	Thermoelectric cooler
TPA	Two-photon absorption
ZBLAN	ZrF_4-BaF_2-LaF_3-AlF_3-NaF
ZDW	Zero-dispersion wavelength

Academic Thesis: Declaration Of Authorship

I, Sijing Liang, declare that this thesis entitled "High Power Pulsed Thulium Doped Fibre Lasers And Their Applications" and the work presented in it are my own and has been generated by me as the result of my own original research.

I confirm that:

1. This work was done wholly or mainly while in candidature for a research degree at this University;
2. Where any part of this thesis has previously been submitted for a degree or any other qualification at this University or any other institution, this has been clearly stated;
3. Where I have consulted the published work of others, this is always clearly attributed;
4. Where I have quoted from the work of others, the source is always given. With the exception of such quotations, this thesis is entirely my own work;
5. I have acknowledged all main sources of help;
6. Where the thesis is based on work done by myself jointly with others, I have made clear exactly what was done by others and what I have contributed myself;
7. Parts of this work have been published as: [see List of Publications]

Signed: ....

Date: ....

Acknowledgements

The four years' time in Southampton has been unforgettable and meaningful. I really appreciate the valuable opportunity to study in ORC, in the pulsed fibre laser group.

I would like to thank my supervisors, Dr. Shaif-ul Alam and Prof. David Richardson, for all the instructions, supports and feedback. It is my pleasure to be a student under the supervision of these two brilliant researchers. Apart from being generous in imparting knowledge and skills, they are responsible supervisors who are always there to help. I particularly appreciate their understandings when I was having a hard time with my family. I thank them both for their great efforts and valuable time in proofreading and polishing all my writings – reports, manuscripts and this thesis.

I would like to thank Dr. Yongmin Jung, Dr. Di Lin, Dr. Jonathan Price and Prof. David Shepherd for their helpful advice during my studies. Yongmin, our group's "splice expert", has taught me a lot in making good splices for different fibres and given me many suggestions about free space optical alignment. Di has kindly shared his experiences in technical operations and his knowledge about high power fibre lasers. Jonathan has reinforced my understandings of supercontinuum generation with his rich research experiences. And I also thank him for offering me an opportunity to be a part-time research assistant in a new project in my final year – developing laser sources for CARS imaging, which is a different field and an exciting challenge. Dave is a nice and patient man whom I always enjoy having discussions and conversations with. I appreciate Dr. Lin Xu particularly for spending much of his time in our discussions and for sharing his knowledge and experiences regarding nonlinear optics and free space optics.

I would like to thank Dr. Zhihong Li, Dr. Nikita Simakov and Dr. Qiongyue Kang for their kind guidance when I began my studies in the first year. I would also like to thank my group colleagues, Dr. Saurabh Jain, Dr. Hans Christian Mulvard, Ms. Neda Baktash, Mr. Krzysztof Herdzik, Mr. Qiang Fu and Mr. Zhengqi Ren, who have been very helpful in our labs during these four years. And thanks to all the technicians and supporting staffs in ORC.

Last but not the least, I thank my parents and my friends for their love and supports throughout my life. I genuinely appreciate my parents for their understandings and

To my parents

Chapter 1 Introduction

This chapter starts with a literature review of the-state-of-the-art thulium doped fibre lasers (TDFLs) and their applications in section 1.1. Our motivations of conducting research activities in this particular field are given in section 1.2. An outline of this thesis is provided in section 1.3.

1.1 The topic area

1.1.1 Thulium doped fibre sources

Laser emissions from rare earth ions doped materials were first observed in bulk glasses in the 1960s [1–3]. Since the first neodymium doped fibre laser was reported later on [4], there has been extensive research in fibre lasers and fibre amplifiers. The next three decades saw a rapid development and many important breakthroughs in this field, thanks to the development of mature fibre fabrication techniques and the availability of high brightness laser diodes [5]. Laser diodes emitting at 9xx nm have accelerated the development of fibre lasers and fibre amplifiers doped with Yb^{3+} and Er^{3+} working at 1 μm and 1.55 μm, as shown in figure 1.1 [6].

In the last twenty years, there has been a surge of research studies in thulium doped fibre lasers operating in the 2-μm region where there is a wealth of applications. In addition to the well-known advantages of fibre-based laser sources (e.g., compactness and long-term stability), TDFLs have another merit that they are "eye safer" as compared to 1-μm lasers, because laser radiation at 2 μm can be absorbed in the vitreous body of eyes so that it does not reach the retina. Hence the threshold of untreatable eye damage is significantly higher [7]. Moreover, the longer emission wavelength allows using thulium doped fibres with a larger core area while maintaining fundamental-mode operation. This results in an up to 4-times increase in the power scalability of TDFLs in comparison with 1-μm fibre lasers [8].

> Each active fiber works within a specific wavelength range determined by the RE ion, and the pump light is a shorter wavelength than the lasing wavelength.
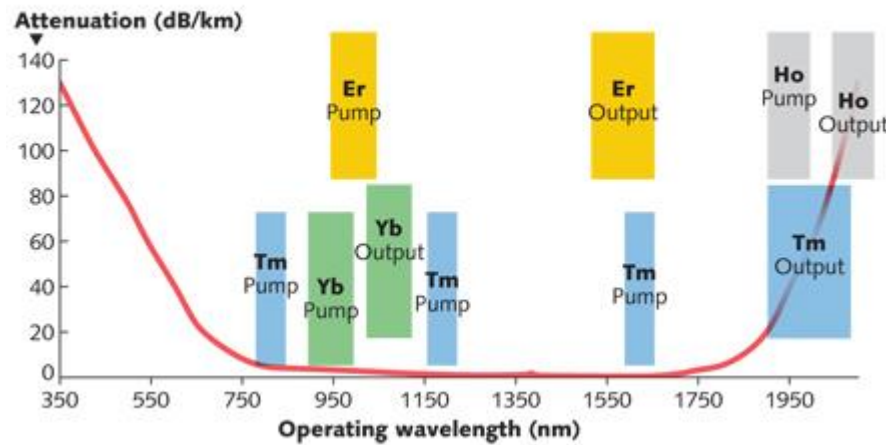
Figure 1.1. Silica fibre attenuation as a function of operating wavelength (red line) and the operation windows of fibre lasers doped with different rare earth ions [6].

Driven by the rapid progress in fibre-component technology at 2 µm, substantial results have been achieved in developing continuous wave (CW) and pulsed thulium doped fibre lasers [9]. In the CW regime, TDFLs with average output powers as high as 1 kW have been demonstrated from LMA fibres, owing to the access to high-power pump diodes at ~790 nm in conjunction with two-for-one cross relaxation (CR) process enabled by heavily doped TDFs [10, 11]. This kW-level output power was achieved in 2010 from an all-fibre two-stage power amplifier and it remains the highest average power reported to date [11]. Since then, wavelength tunability of CW TDFLs has become the focus of researchers' attentions, with numerous demonstrations of CW TDFLs delivering hundreds of watt output power over a wide wavelength range [12–15]. For example, K. Yin *et al.* reported an all-fibre high power TDFL producing an output power of ~300 W from 1910 nm to 2050 nm [13]. Another all-fibre thulium doped fibre MOPA demonstrated tuneable operation from 1966 nm to 2001 nm with an output power of >250 W [14].

Table 1.1 summarises the maximum average powers and peak powers achieved from the reported pulsed TDFLs based on both LMA fibres and photonic crystal fibres (PCFs), to the best of our knowledge. In the nanosecond regime, high-energy pulse generation has been demonstrated in TDFLs with different structures, using techniques like Q-switching, gain-switching, MOPA approaches and so on [16–18]. Recently, nanosecond pulses with a maximum average output power of 238 W were generated from a fully-fiberised high-power thulium doped fibre MOPA [19]. In this

work, pulse energy and peak power of nanosecond pulses were scaled up to 0.749 mJ and 12.1 kW, respectively. Further energy scaling to beyond 1 mJ has been achieved in [20] and [21]. Nanosecond pulses with a highest peak power of 54 kW were obtained from an LMA-fibre-based thulium doped fibre MOPA seeded by a gain-switched TDFL [21]. With mature fabrication techniques and stable output performances, LMA thulium doped fibres have proved themselves good candidates for building lasers that deliver high average output powers.

Thulium doped photonic crystal fibre, on the other hand, is more favourable for scaling the peak power of laser pulses due to its low nonlinearity, irrespective of the special care required in handling such fibres. By using a rod-type thulium-doped PCF with an 80-µm core diameter, peak power of nanosecond pulses was successfully enhanced to ~1 MW [22]. Generally speaking, large-core thulium-doped photonic crystal fibres are more often used in the quest for high peak powers, therefore the maximum average output power reported from a PCF-based nanosecond-pulsed TDFL is far less than that from an LMA-fibre-based TDFL.

		Nanosecond	*Picosecond*	*Femtosecond*
LMA	Max. Avg. Power	238 W [19]	240 W [32]	15.6 W [25]
	Max. Peak Power	54 kW [21]	130 kW [30]	200 MW [25]
			(295 kW *)	
PCF	Max. Avg. Power	7 W [22]	6 W [31]	152 W [27]
	Max. Peak Power	1 MW [22]	230 kW [31]	4 GW [26]

Table 1.1. Maximum average powers and peak powers of pulsed TDFLs reported in literatures. (Power noted by the asterisk is the highest peak power achieved in this thesis).

Femtosecond-pulsed TDFL is a good option for applications demanding ultrashort pulses with extremely high peak power. The first demonstration of femtosecond pulses from an LMA thulium doped fibre amplifier was reported in 2005, which obtained 108-fs pulses with 230-kW peak power without using an external pulse compressor [23]. Chirped pulse amplification (CPA) provides an easier route to scale the pulse peak power to MW level, because high-peak-power-induced nonlinear effects can be avoided in fibre amplifiers by temporally stretching the seed pulses. Amplified pulses are then compressed to shorter pulses with higher peak power at the output, for example by an external grating compressor [24]. P. Wan *et al.* reported the current highest peak power (~200 MW) of femtosecond

pulses generated from an LMA-TDF-based MOPA system, with a pulse duration of 780 fs and pulse energy of 156 µJ after compression [25]. Recently, the peak power of femtosecond pulses yielded from a Tm-doped-PCF chirped-pulse amplification system was enhanced by employing a gas-filled hollow-core glass capillary for nonlinear pulse compression, reaching 4 GW [26]. Interestingly, a high-average-power thulium doped fibre CPA system was demonstrated by F. Stutzki *et al.* in 2014, producing sub-700-fs pulses with a record average output power of 152 W and a peak power of 4 MW from a thulium doped PCF with a 50-µm core diameter [27]. Such CPA systems can easily generate femtosecond pulses with peak power in excess of MW, but they require dispersion management and external devices for pulse compression, which makes the system configuration more complicated.

Picosecond pulse generation was less explored in the prior work and the peak power record stood at only ~10 kW [28, 29]. But the peak power was lately increased to ~130 kW in a gain-switched diode-seeded MOPA system based on an LMA thulium doped fibre [30]. This high-power diode-seeded MOPA system can provide picosecond pulses offering material processing benefits comparable to femtosecond laser systems but with additional advantages of flexibility and lower cost. S. Guillemet *et al.* recently demonstrated 520-ps pulses with a peak power of up to 230 kW from a thulium doped PCF with a core diameter of 80 µm [31]. An all-fibre linearly-polarised picosecond thulium doped fibre MOPA system reported the current highest average output power of 240 W, which is comparable to the average power of many nanosecond-pulsed TDFLs [32].

1.1.2   Applications of TDFLs

Thulium doped fibre lasers have been utilised for a variety of applications, which include sensing, spectroscopy, laser surgery, material processing, nonlinear frequency conversion and so on [7, 33–37].

TDFLs can be employed in the detection and analysis of many atmospheric gases such as H_2O and CO_2, because many absorption lines of these gases are located around 2 µm, as illustrated in figure 1.2 [38]. In many atmospheric transmission windows near 2 µm, pulsed fibre laser sources enable geographical detection including direction, position and distance, by measuring the back scattered light. In such LIDAR (LIght Detection And Ranging) applications, 2-µm short-pulse fibre lasers with appreciable power are ideal for practical usage [7]. LIDAR operating in

the 2-μm region has an exceptional benefit that it allows using pulsed TDFLs with almost 4-times higher pulse energy as compared to 1-μm fibre lasers [38].
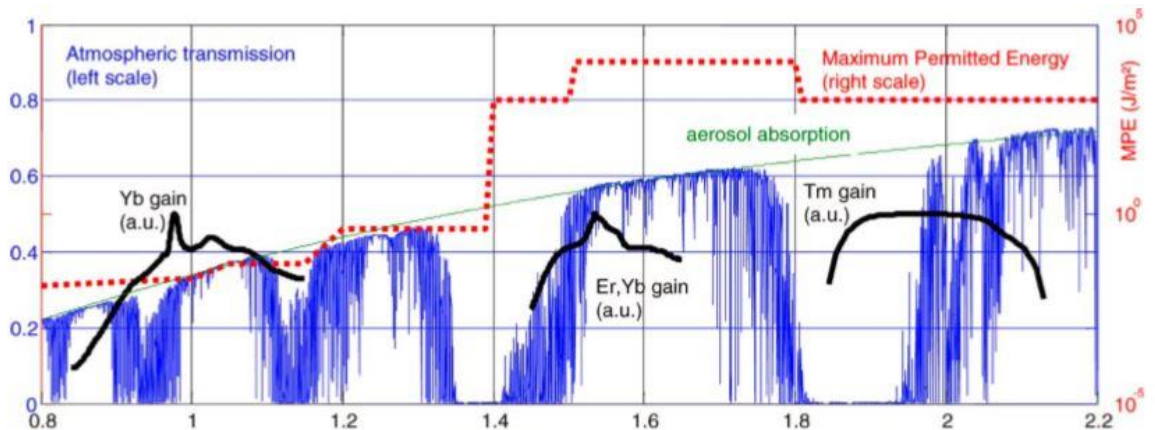
Figure 1.2. Atmospheric transmission over the 0.8–2.2 μm wavelength range for 6-km propagation measured at 1000-m height from ground level [38].

TDFLs are very promising in surgical applications due to strong water absorption at 2 μm. As indicated in figure 1.3, the penetration depth is reduced to a few hundred μm when using 2-μm lasers, leading to minimal damage around the exposed area caused by ablation effects. TDFLs also allow precise cutting of biological tissue since substantial heat can be generated in small areas of the highly-hydrated tissue [7, 35].
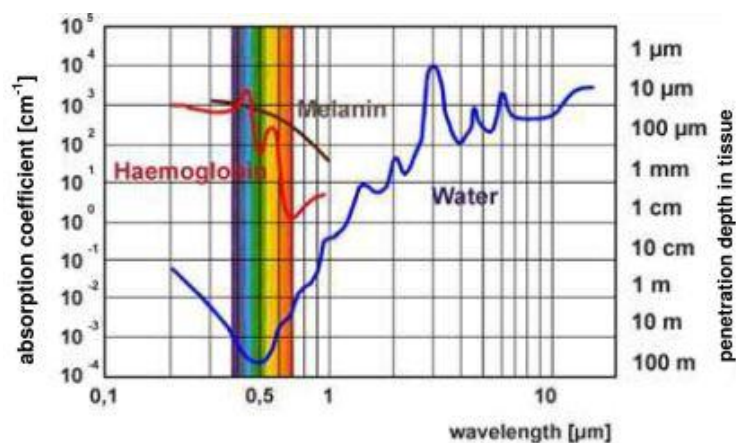
Figure 1.3. Absorption and penetration depth in biological tissue as a function of wavelengths [7].

Material processing, especially plastics processing, can take advantage of 2-μm fibre lasers that deliver high output power and good beam quality. Plastic materials exhibit strong absorption around 2 μm, allowing direct processing with 2-μm fibre lasers. Hence using reliable high-power TDFLs can simplify the process of cutting, welding and marking plastic materials [7, 34].

Thulium doped fibre possessing broad gain bandwidth in the 2-μm region is attractive to optical communication because of its potential to extend the current telecommunication window, thereby increasing the transmission capacity and addressing the "capacity crunch" problem in the near future [39]. In the past few years, considerable achievements were obtained in developing high-gain thulium doped fibre amplifiers (TDFAs) with a wide operation window. Diode-pumped TDFAs provide high gain and low noise amplification over a 250-nm wavelength range from 1800 nm to 2050 nm, which strongly supports the exploitation of a new transmission window for communications at 2 μm [40]. The amplification window has lately extended down to 1.65 μm [41, 42] whilst a TDFL based on a Tm/Ge co-doped fibre has recently demonstrated ultra-short-wavelength operation in the 1620-1660nm waveband [43], both indicating the possibility to bridge the gap between erbium doped fibre amplifiers (EDFAs) and TDFAs.

In addition to the applications described above, TDFLs are also interesting for generating mid-infrared lasers via nonlinear frequency conversion, particularly in the field of SC generation where appreciable results have been achieved [44–46]. Mid-infrared SC laser sources offering advantages such as high brightness, good spatial coherence and broad spectral bandwidth are desirable for many applications, including molecular spectroscopy, optical frequency metrology, optical coherence tomography and so on [47]. In particular, high-power mid-infrared SC generation is very useful for gas sensing, since absorption lines of a variety of gases reside in the mid-infrared region, as depicted by figure 1.4 [48].
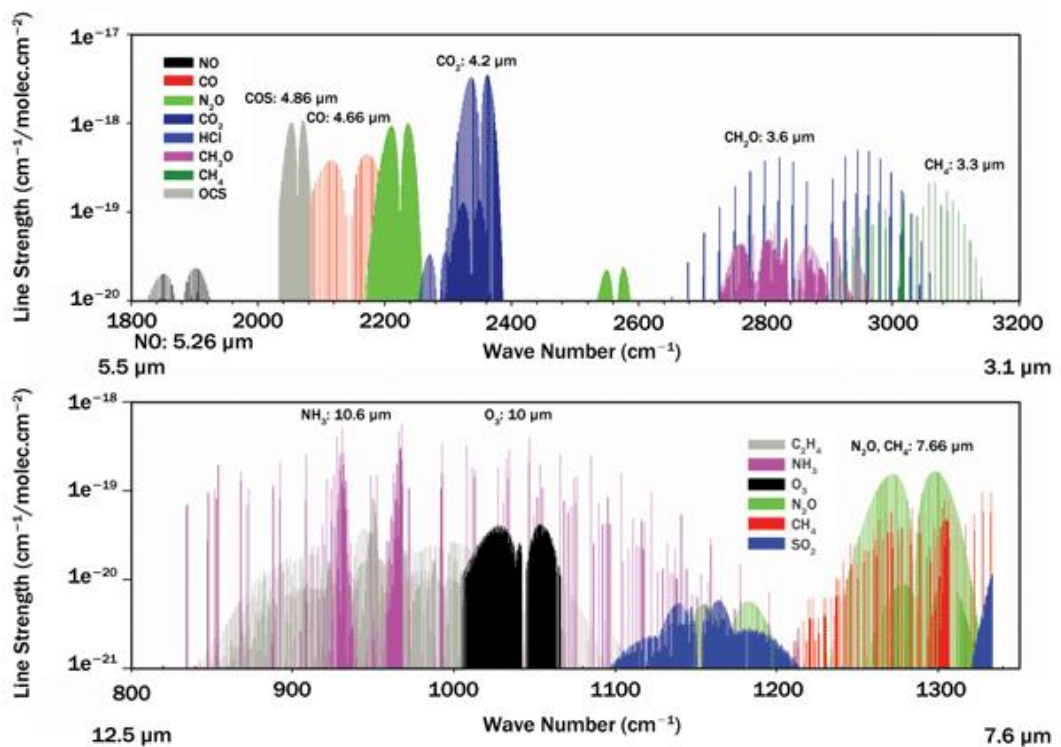
Figure 1.4. Mid-infrared molecular absorption spectra from HITRAN database [48].

Hagen *et al.* reported the first SC generation in ZBLAN fibres in 2006 [49]. Before the advent of high-power pulsed TDFLs, SC generations in ZBLAN fibres were mostly achieved by 1.55-µm fibre lasers, producing broadband laser emissions from ~1.5 µm to ~3.5 µm [49, 50]. By shifting the pump wavelength from 1.55 µm to 2 µm, TDFL-pumped ZBLAN fibres have extended the mid-infrared SC generation to ~4.5 µm and enabled higher power conversion efficiency from pump to SC generation [45, 46].

To date, ZBLAN-based SC generation with excellent output performances can be implemented in fully-fiberised structures, producing broad output spectrum, good spectral flatness and watt-level output power for mid-infrared wavelengths. SC generation covering 750–4000 nm with a high degree of spectral flatness in the long wavelength region has been achieved by pumping ZBLAN fibres with 2-µm picosecond pulses [37]. A record average output power of 21.8 W over a span from 1.9 µm to beyond 3.8 µm has been demonstrated from a thulium-fibre-laser-pumped ZBLAN fibre [51]. Another high-brightness SC laser source based on ZBLAN fibres was reported generating 8.1 W and 1.08 W of power for wavelengths beyond 3.0 µm and 3.8 µm, respectively [46]. All-fibre turn-key ZBLAN-based SC lasers

delivering watt-level output power with excellent stability are now commercially available [52].

However, the exponentially growing attenuation of ZBLAN fibres beyond 4 µm inhibits SC generation extending to longer wavelengths. But further mid-infrared SC generation can be addressed by fluoroindate fibres which are more transparent over 4–5 µm. As compared to ZBLAN fibres, SC generation in fluoroindate fibres is less widely reported. The first demonstration of SC generation in such fluoroindate fibres pumped by a femtosecond laser was reported by Théberge *et al.* in 2013 [53]. A 20-dB spectral flatness from 2.7 µm to 4.7 µm was achieved in this work, implying the possibility to extend mid-infrared SC generation to 5 µm or more. In another experiment, an 8-m-long fluoroindate fibre with a core/cladding diameter of 16.7/125 µm was pumped by 2-µm pulses, producing a supercontinuum from 1.7 µm to 3 µm. The spectral broadening was limited to ~3 µm, mainly because of the reduced nonlinearity in a larger-core fibre [45].

Recent results of SC generation in fluoroindate fibres have shown an improvement in spectral coverage and spectral flatness. Mid-infrared SC generation from 2.4 µm to 5.4 µm was achieved in a low-loss fluoroindate fibre pumped by an erbium doped fluoride fibre laser [54], while a picosecond-OPG-pumped SC laser based on a small-core fluoroindate fibre produced a 5-dB spectral flatness over a span from 2 µm to 5 µm [55]. Nevertheless, the reported output powers of all these SC laser sources using fluoroindate fibres were just in the tens of milliwatt regime, which is significantly lower than that achieved in ZBLAN fibres. Further spectral extension into the mid-infrared region is expected in the near future with more powerful pump sources and better fibre designs/materials.

1.2   Motivations

Combined with characteristics like compactness, robustness, good beam quality and maintenance-free potential, fibre lasers operating in the 2-µm wavelength range can easily find many applications in remote sensing, surgery, material processing and frequency conversion to different wavelengths. Driven by these promising applications, it is interesting to develop thulium doped fibre laser sources, especially the high-power pulsed TDFLs, which could serve as practical pump sources for many nonlinear frequency conversion applications.

We investigate the power amplification of picosecond pulses in a 25-μm-core LMA thulium doped fibre, instead of using rod-type thulium doped PCFs with larger core size and chirped pulse amplification so as to avoid adding difficulties to system operation. The development of our high-power thulium doped fibre MOPA systems is also meant for creating novel laser sources emitting at wavelengths that are difficult to reach with traditional solid-state lasers.

Owing to some applications requiring high-power broadband lasers, we study supercontinuum generation in fluoride fibres pumped by our high-power thulium doped fibre MOPA. We employ a ZBLAN fibre to demonstrate SC generation from 1 μm to 4 μm so as to accommodate our needs in labs such as characterisation of mid-infrared hollow-core fibres. Meanwhile, we aim to enhance the output power and extend the spectral bandwidth of mid-infrared SC generation to beyond 4 μm by exploiting fluoroindate fibres pumped with 2-μm high-peak-power pulses.

As shown in figure 1.4, there lies a tremendous amount of molecular absorption lines in the "molecular fingerprint" region (7–12 μm), which cannot be accessed by our fluoride-fibre-based SC lasers working at the 1–5 μm window. To fill the vacancy in laser emission beyond 5 μm, we study optical parametric generation and amplification in OP-GaAs crystals pumped by our high-power thulium doped fibre MOPA. On the other hand, we also investigate frequency up-conversion in 2-μm-pumped PPLN crystals so as to attain high-power picosecond pulses at exotic wavelengths.

In general, we develop the high-power thulium doped fibre MOPA and use it for different kinds of nonlinear frequency conversion in the hope of providing access to laser sources operating over a wide wavelength range.

1.3   Outline of thesis

This thesis is structured as follows.

Chapter 2 provides a comprehensive theoretical background which includes spectroscopy of thulium doped fibres, the basic laser physics and the enabling technologies of fibre lasers, and the nonlinear effects that may be encountered in experiments.

Chapter 3 focuses on investigating the generation of high-peak-power picosecond pulses from a thulium doped fibre MOPA system seeded by a gain-switched laser diode. This high-power MOPA system was then employed in different frequency conversion applications.

The development of ultra-broadband mid-infrared SC generation in fluoride fibres pumped by the 2-μm high-peak-power picosecond pulses is described in chapter 4.

Chapter 5 reports frequency doubling and quadrupling of the picosecond thulium doped fibre MOPA in PPLN crystals.

Chapter 6 presents the research in optical parametric generation and amplification based on OP-GaAs crystals, using the picosecond thulium doped fibre MOPA as the pump source.

Finally, conclusions and future work are given in chapter 7.

Chapter 2 Theoretical background

This chapter discusses the theoretical background knowledge that is related to the experimental work in this thesis. Basics of thulium doped fibres are illustrated in section 2.1, including principles of fibres and spectroscopic characteristics of thulium doped silica fibres. In section 2.2, rate equations of TDFA are first described, followed by a discussion of pumping schemes and an overview of MOPA technology. Section 2.3 illustrates the nonlinearities frequently encountered in developing high power fibre lasers system as well as the underlying physics of supercontinuum generation. An introduction to second order nonlinear effects in crystal materials is provided in section 2.4.

2.1   Overview of thulium doped fibres

2.1.1   Fibre optics basics

Figure 2.1 depicts the simplest form of an optical fibre which consists of a small cylindrical core of glass surrounded by a much larger cladding. The refractive index of the core (n_1) is higher than that of the cladding (n_2), which enables light confinement in the fibre through total internal reflection. This fibre structure is known as "step-index" due to an abrupt change in refractive index at the core-cladding interface [56].
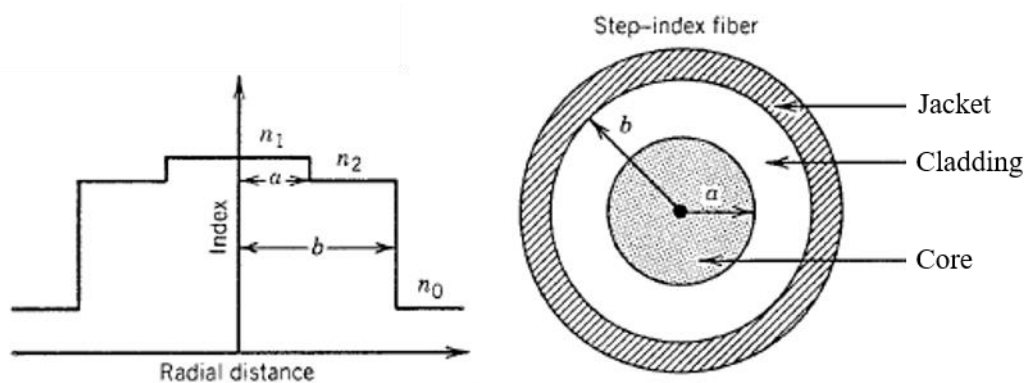
Figure 2.1. Cross section and refractive index profile for a step-index fibre [56].

Light propagation along a step-index fibre is illustrated in figure 2.2. A beam is injected into the fibre core at an angle of θ_i with respect to the fibre axis. The refractive index of air is denoted by n_0. According to Snell's law, the angle of the refracted ray θ_r is given by [57]:

$$n_0 \sin \theta_i = n_1 \sin \theta_r \tag{2.1}$$
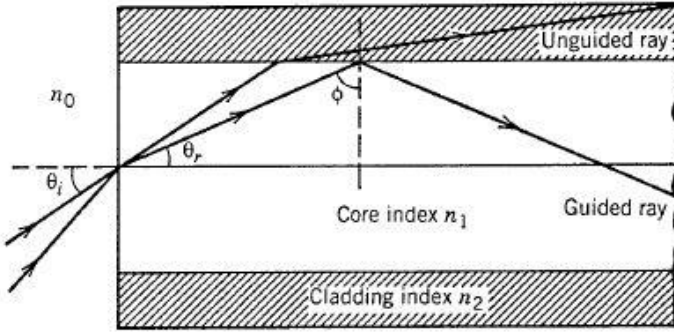
Figure 2.2. Light confinement through total internal reflection in step-index fibres [56].

The refracted ray strikes the core-cladding interface at an angle of ϕ, which can also be represented by:

$$\phi = \frac{\pi}{2} - \theta_r \tag{2.2}$$

To keep light inside the optical fibre, the angle ϕ must meet the requirement of total internal reflection that it has to be larger than a critical angle ϕ_c, which is defined by [58]:

$$\sin \phi_c = n_2/n_1 \tag{2.3}$$

With Eq. 2.1 to Eq. 2.3, we obtain the numerical aperture (NA) of the fibre, which describes the light-gathering capacity of an optical fibre.

$$NA = n_0 \sin \theta_i = n_1 \cos \phi_c = \sqrt{n_1{}^2 - n_2{}^2} \tag{2.4}$$

Step-index fibres can support the transmission of a set of different beams, which all satisfy the condition that $\phi > \phi_c$. These beams are called modes and are distinguished by their propagation angles with respect to the fibre axis [58]. The number of modes that a fibre can carry is determined by the normalised frequency parameter, which is also known as the "V number":

$$V = \frac{2\pi \cdot a}{\lambda} NA \qquad (2.5)$$

where a is the fibre core radius and λ is the light wavelength. When $V \leq 2.405$, the fibre supports only the fundamental mode and such fibre is called single mode fibre. A fibre is multimode if $V > 2.405$ [58]. For instance, an LMA thulium doped fibre with a core diameter of 25 μm and a core NA of 0.09 yields a V number of 3.6 at a light wavelength of 1.95 μm, which means this fibre can support 4 modes. To ensure fundamental-mode operation in LMA fibres, the LMA fibre can be bent to introduce higher attenuation to the high-order modes.

Light propagation in a step-index fibre can be described by wave equations and waveguide-boundary conditions. The propagation constant of the guided modes can be obtained by solving these equations and defined as [58]:

$$\beta = n_{eff} k \qquad (2.6)$$

where k is the wavenumber in vacuum and the effective refractive index n_{eff} of a guided mode must satisfy the following condition ($n_2 < n_{eff} < n_1$). Silica fibre has a frequency dependent refractive index $n(\omega)$. Therefore, the mode propagation constant can be expanded in a Taylor series about the central frequency of light (ω_0) [59]:

$$\beta(\omega) = n(\omega)\frac{\omega}{c} = \beta_0 + \beta_0(\omega - \omega_0) + \frac{1}{2}\beta_0(\omega - \omega_0)^2 + \cdots \qquad (2.7)$$

where

$$\beta_m = \left(\frac{d^m \beta}{d\omega^m}\right)_{\omega = \omega_0} \quad (m = 0, 1, 2 \cdots) \qquad (2.8)$$

Parameters β_1 and β_2 can be derived from Eq. 2.7 and Eq. 2.8 [59]:

$$\beta_1 = \frac{1}{v_g} = \frac{n_g}{c} = \frac{1}{c}\left(n + \omega\frac{dn}{d\omega}\right) \tag{2.9}$$

$$\beta_2 = \frac{1}{c}\left(2\frac{dn}{d\omega} + \omega\frac{d^2n}{d\omega^2}\right) \tag{2.10}$$

The group velocity v_g represents the velocity at which the envelope of an optical pulse moves, and β_2 is known as the group velocity dispersion (GVD) parameter. Dispersion parameter D is defined as [59]:

$$D = \frac{d\beta_1}{d\lambda} = -\frac{2\pi c}{\lambda^2}\beta_2 = -\frac{\lambda}{c}\frac{d^2n}{d\lambda^2} \tag{2.11}$$

Figure 2.3 plots the typical dispersion profile of bulk fused silica as a function of wavelength. When $D < 0$ $(\beta_2 > 0)$, the fibre dispersion is described as normal, whereas the fibre is said to exhibit anomalous dispersion if $D > 0$ $(\beta_2 < 0)$. In the normal dispersion regime, high-frequency components of an optical pulse travel slower than the low-frequency components of the same pulse. The opposite situation occurs in the anomalous dispersion regime [59].
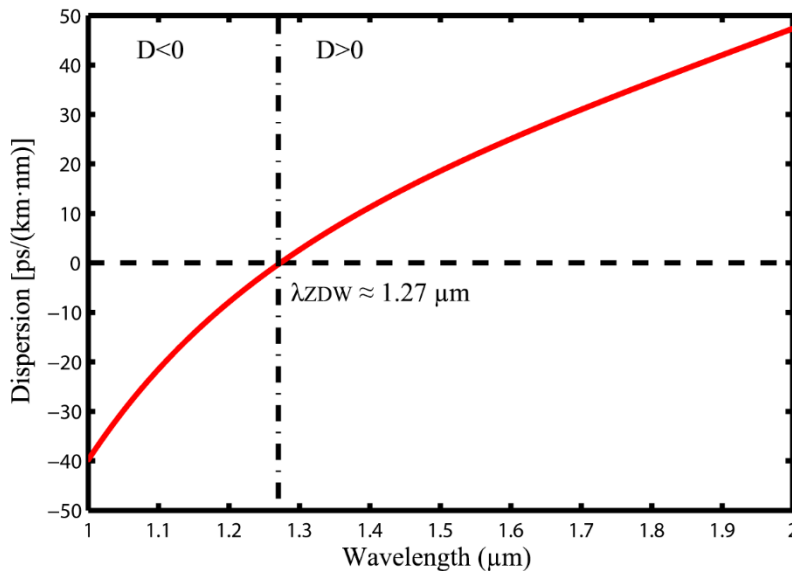
Figure 2.3. Variation of D with wavelength in bulk fused silica [59].

14

General thulium doped silica fibres have a large anomalous dispersion because operating wavelengths (1.65–2.05 µm) are far from the zero-dispersion wavelength (ZDW). Special fibre design can modify the dispersion profile of thulium doped fibres and such normal dispersion thulium doped fibres have been demonstrated in literatures [60, 61]. But note that all thulium doped fibres used in experiments in this thesis are anomalously dispersive at 2 µm.

2.1.2   Spectroscopy of thulium doped silica fibres

A simplified energy level diagram of thulium doped fibres is plotted in figure 2.4. 2-µm radiation is achieved by transition from the $^3F_4$ level to the $^3H_6$ level. Thulium ions can be excited from the ground state ($^3H_6$) to the $^3F_4$, $^3H_5$ and $^3H_4$ levels by pump light centred at ~790 nm, ~1210 nm and ~1600 nm. Due to the short lifetime of the $^3H_4$ level and the relatively small branching ratio (8–10%) of the $^3H_4 \rightarrow {}^3H_5$ transition, non-radiative decay becomes predominant in the transition between these two levels [62]. As a result of the close energy spacing between the $^3H_5$ and $^3F_4$ levels, the $^3H_5 \rightarrow {}^3F_4$ transition is also dominated by non-radiative decay [63]. Hence 2-µm laser emission can be implemented directly by exciting thulium ions to the upper level ($^3F_4$), or indirectly by non-radiative decaying of ions from the excited states to the $^3F_4$ level.

In comparison with Er^{3+}, Tm^{3+} has a much shorter lifetime of the upper energy level. While the $^4I_{13/2}$ level and the $^4I_{15/2}$ level are so well separated that non-radiative decay in erbium doped fibres is negligible, the energy gap between the $^3F_4$ level and the $^3H_6$ level is much smaller so that multiphonon assisted non-radiative decay in thulium doped fibres becomes easier, thereby reducing the measured lifetime of the upper state to hundreds of µs. This can lead to a higher pump threshold for lasers [62].
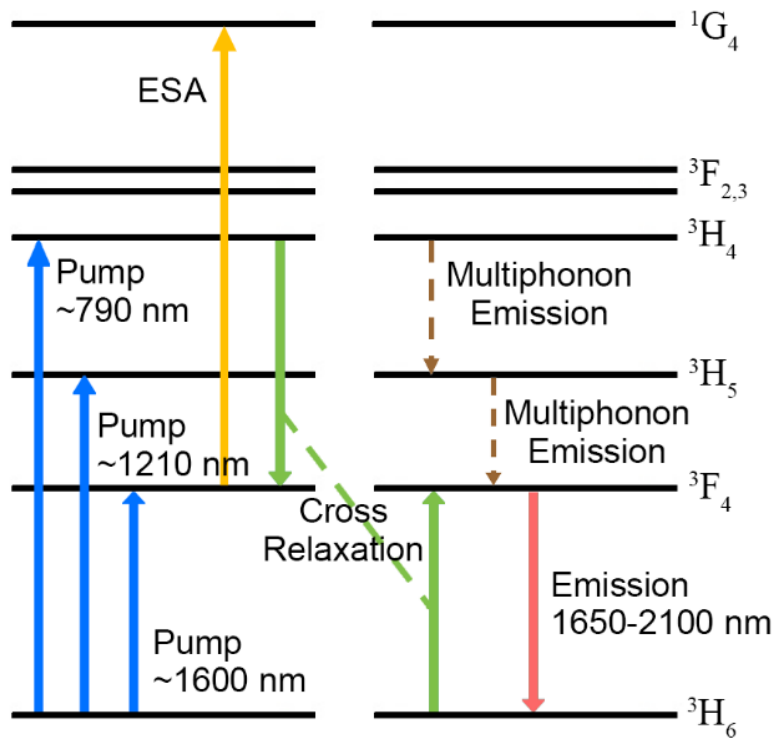
Figure 2.4. Energy level diagram of thulium doped silica fibres.

Figure 2.5 illustrates an example of the absorption and emission cross-section spectra with corresponding energy levels of a thulium doped silica fibre [64]. Note that accurate measurements of absorption and emission cross-sections of TDFs used in this thesis cannot be performed, due to limited knowledge of fibre composition (e.g. dopant concentration) and lack of proper equipment. However, the example cross-sections can still indicate the performance that we can expect from our fibres.

It can be seen from figure 2.5 that the $^3F_4 \rightarrow {}^3H_6$ transition features laser emission spanning approximately from 1.65 μm to 2.1 μm, which is much broader than the emission bandwidth of other rare earth doped silica fibres [62]. This broadband emission originates from the Stark-effect-induced splitting of energy levels. Energy levels with total orbital momentum J are split into a manifold of $g = J + 1/2$ energy sublevels [65]. Since Tm[3+] has more sublevels in each Stark manifold than Er[3+] and Yb[3+], it has potentially larger absorption and emission bandwidth. In-band pumping at ~1.6 μm is beneficial to efficient laser emission at 2 μm due to an inherent low quantum defect.
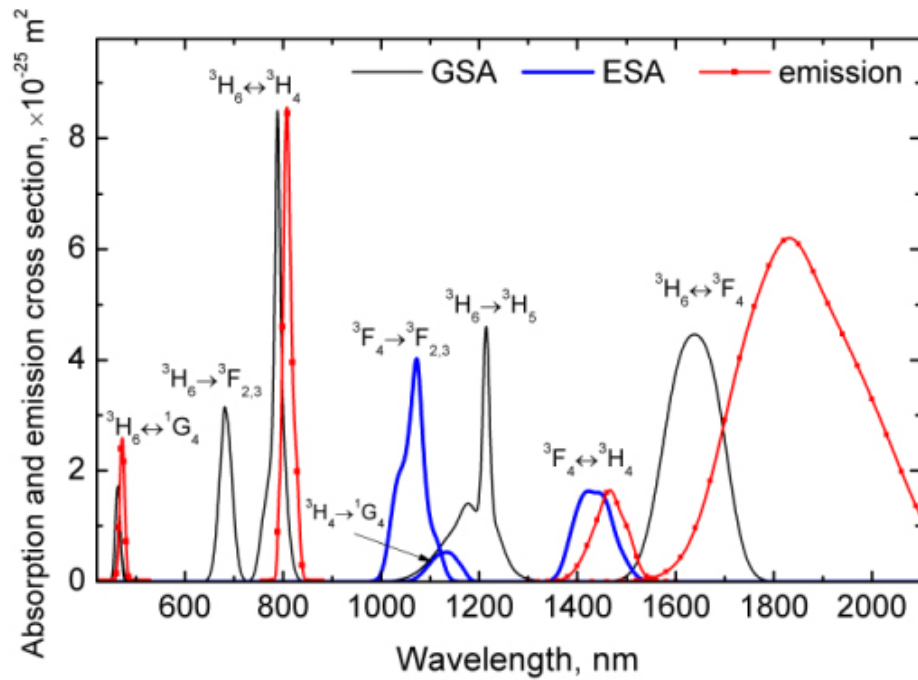
Figure 2.5. Absorption and emission cross-section spectra of thulium doped silica fibres [64].

In contrast, the pump bands at ~790 nm and ~1210 nm are much narrower than the 1550–1750 nm pump band. On the other hand, thulium doped fibres are prone to suffer from excited state absorption (ESA) when pumped around 1210 nm [63]. Despite a narrow pump bandwidth, the 790-nm pumping scheme offers the advantage of much stronger pump absorption as compared to in-band pumping, which helps in shortening the device length. Moreover, the 780–800 nm pump band is attractive to high power operation because it can be accessed by high-power multimode laser diodes.

The quantum defect of the ~790-nm pumped TDFL is large, which limits the laser quantum efficiency to a maximum of ~40%. However, the laser efficiency can be enhanced to beyond the quantum limit by means of the cross relaxation process $^3H_4, ^3H_6 \rightarrow ^3F_4, ^3F_4$, as indicated in figure 2.4 [62]. A thulium ion at the excited state $^3H_4$ can decay to the $^3F_4$ level, while transferring its residual energy to another thulium ion at the ground state $^3H_6$, which is then excited to the $^3F_4$ level. This process is also known as "two-for-one" cross relaxation because two excited states of Tm^{3+} are created for a single absorbed pump photon. Hence the laser efficiency can be enhanced to the maximum of ~80% in theory. To date, a typical slope efficiency of 50-60% can be obtained from a high-power TDFL pumped at ~790 nm [66]. However, it was found that the CR process exhibits a strong dependence on

the fibre dopant concentration [67, 68]. To achieve efficient cross relaxation, it requires a fibre with high Tm^{3+} concentration, usually >2 wt. %. Al^{3+} is added in fibre fabrication to provide rare earth solubility to silica and minimise clustering of Tm^{3+}, with an Al^{3+}/ Tm^{3+} concentration ratio of >10 recommended [62, 67, 68].

2.2   Amplification in thulium doped fibres

2.2.1   Rate equations of thulium doped fibre amplifiers

Amplification in thulium doped fibres can be described by rate equations, just like other rare earth doped fibre amplifiers. General rate equations for three-level systems are detailed in literatures [65, 69]. But in this subsection, rate equations are specified for in-band pumped and indirectly pumped TDFAs.

Before discussing the rate equations, the energy level diagram in figure 2.4 is simplified into figure 2.6 which includes only four energy levels ($^3H_6$, $^3F_4$,$^3H_5$ and $^3H_4$). The population of energy levels are denoted by N_0, N_1, N_2 and N_3, respectively. N_2 is negligible due to the fast non-radiative decay from $^3H_5$ to $^3F_4$. W_{p03}, W_{p01} and W_{p10} are the pump transitions, and W_{s01} and W_{s10} are the signal transition between energy levels. The subscript numbers indicate the energy levels involved. For example, W_{p03} represents the pump transition from level 0 ($^3H_6$) to level 3 ($^3H_4$). Spontaneous lifetimes of levels $^3F_4$,$^3H_5$ and $^3H_4$ are represented by τ_1, τ_2 and τ_3. Cross relaxation process, denoted by C_p, is also considered in the following rate equations. Note that more details about the theoretical model of TDFAs can be found in ref. [70].
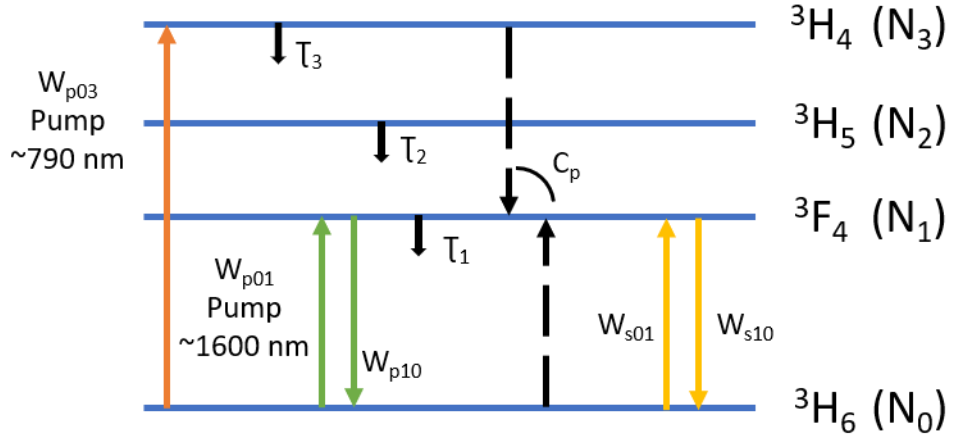
Figure 2.6. Simplified energy level diagram of TDFAs.

2.2.1.1 $^3H_6 \rightarrow {}^3F_4$ pump scheme

In the case of in-band pumping at ~1600 nm, thulium ions at the ground state are directly pumped to the upper state $^3F_4$ and cross relaxation process can be ignored due to very few ions are excited to the energy levels above $^3F_4$. Thus, rate equations of a TDFA at any position along the active fibre can be expressed as [70]:

$$\frac{dN_0(z,t)}{dt} = -W_{p01} + W_{p10} + \frac{N_1(z,t)}{\tau_1} + W_{s10} - W_{s01} \tag{2.12}$$

$$\frac{dN_1(z,t)}{dt} = W_{p01} - W_{p10} - \frac{N_1(z,t)}{\tau_1} - W_{s10} + W_{s01} \tag{2.13}$$

The concentration of thulium ions inside the fibre, N_T, can be approximately viewed as the total number of ions in level 0 ($^3H_6$) and level 1 ($^3F_4$) [70]:

$$N_T = N_0(z,t) + N_1(z,t) \tag{2.14}$$

The pump absorption rate W_{p01} is given by [70]:

$$W_{p01} = \frac{\lambda_p \Gamma_p}{hcA_{core}} \sigma_a(\lambda_p) N_0(z,t)[P_p^-(z) + P_p^+(z)] \tag{2.15}$$

De-excitation of thulium ions at level 1 ($^3F_4$) is expressed as [70]:

$$W_{p10} = \frac{\lambda_p \Gamma_p}{hcA_{core}} \sigma_e(\lambda_p) N_1(z,t)[P_p^-(z) + P_p^+(z)] \tag{2.16}$$

Signal transitions between level 0 (^{3}H$_6$) and level 1 (^{3}F$_4$), W_{s01} and W_{s10}, are written as [70]:

$$W_{s01} = \frac{\lambda_s \Gamma_s}{hcA_{core}} \sigma_a(\lambda_s) N_0(z,t) \times [P_s(z) + ASE_f(z) + ASE_b(z)] \quad (2.17)$$

$$W_{s10} = \frac{\lambda_s \Gamma_s}{hcA_{core}} \sigma_e(\lambda_s) N_1(z,t) \times [P_s(z) + ASE_f(z) + ASE_b(z)] \quad (2.18)$$

In the above equations, h is the Planck constant and c is the speed of light in vacuum. λ_p and λ_s stand for the wavelengths of pump and signal, respectively. A_{core} is the cross-section area of the doped core [70]. Γ_p and Γ_s denote the confinement factors of the pump and signal inside the doped fibre. $\sigma_a(\lambda_p)$ and $\sigma_a(\lambda_s)$ are the absorption cross sections of the pump and signal, while the corresponding emission cross sections are represented by $\sigma_e(\lambda_p)$ and $\sigma_e(\lambda_s)$ [70].

Signal power at position z is termed as $P_s(z)$. Accordingly, the forward and backward pump powers at position z are denoted by $P_p{}^+(z)$ and $P_p{}^-(z)$. $ASE_f(z)$ and $ASE_b(z)$ refer to the amplified spontaneous emission (ASE) in the forward and backward directions, respectively [70].

Thus, power distributions of the pump, signal and ASE can be expressed as follow [70]:

$$\frac{dP_p^{\pm}}{dz} = \pm P_p^{\pm}(z) \left[\Gamma_p \left(\sigma_e(\lambda_p) N_1(z) - \sigma_a(\lambda_p) N_0(z) \right) - \alpha_p \right] \quad (2.19)$$

$$\frac{dP_s}{dz} = P_s(z) \left[\Gamma_s \left(\sigma_e(\lambda_s) N_1(z) - \sigma_a(\lambda_s) N_0(z) \right) - \alpha_s \right] \quad (2.20)$$

$$\frac{dASE_f}{dz} = ASE_f(z) \left[\Gamma_s \left(\sigma_e(\lambda_s) N_1(z) - \sigma_a(\lambda_s) N_0(z) \right) - \alpha_s \right] +$$

$$2\sigma_e(\lambda_s) N_1(z) \frac{hc^2}{\lambda_s{}^3} \Delta\lambda \quad (2.21)$$

$$\frac{dASE_b}{dz} = -ASE_b(z) \left[\Gamma_s \left(\sigma_e(\lambda_s) N_1(z) - \sigma_a(\lambda_s) N_0(z) \right) - \alpha_s \right] +$$

$$2\sigma_e(\lambda_s) N_1(z) \frac{hc^2}{\lambda_s{}^3} \Delta\lambda \quad (2.22)$$

where α_p and α_s are the intrinsic absorptions of the active fibre at pump and signal wavelengths; $\Delta\lambda$ is the ASE bandwidth [70].

When the amplifier operates in the steady state, the following condition is met [70]:

$$\frac{dN_0(z,t)}{dt} = \frac{dN_1(z,t)}{dt} = 0 \tag{2.23}$$

With initial conditions of the TDFA (e.g. $P_p{}^+(z=0)$, $P_s(z=0)$, etc.) and parameters of the doped fibre (e.g. absorption and emission cross-sections, fibre dimension, etc.), the rate equations and the power distribution along the fibre can be solved numerically.

2.2.1.2   ³H₆ → ³H₄ pump scheme

When thulium ions are pumped to the ³H₄ level by ~790-nm light, cross relaxation can take place and rate equations are revised to [70]:

$$\frac{dN_3(z,t)}{dt} = W_{p03} - \frac{N_3(z,t)}{\tau_3} - C_p \tag{2.24}$$

$$\frac{dN_1(z,t)}{dt} = -\frac{N_1(z,t)}{\tau_1} + \frac{\beta_{31}N_3(z,t)}{\tau_3} - W_{s10} + W_{s01} + 2C_p \tag{2.25}$$

$$N_T = N_0(z,t) + N_1(z,t) + N_3(z,t) \tag{2.26}$$

$$C_p = k_{3101}N_0(z,t)N_3(z,t) - k_{1310}N_1{}^2(z,t) \tag{2.27}$$

where β_{31} is the branching ratio of spontaneous transition from level 3 (³H₄) to level 1 (³F₄); k_{3101} and k_{1310} represent the cross-relaxation constants [70].

Pump absorption rate W_{p03} is written as:

$$W_{p03} = \frac{\lambda_p\Gamma_p}{hcA_{core}}\sigma_a(\lambda_p)N_0(z,t)[P_p{}^-(z) + P_p{}^+(z)] \tag{2.28}$$

Expressions (Eq. 2.20–2.22) remain valid for the power distributions of signal and ASE along the fibre. But the propagation equation of pump light in the TDF should be replaced by [70]:

$$\frac{dP_p{}^\pm}{dz} = \mp P_p{}^\pm(z)\left[\Gamma_p\left(\sigma_a(\lambda_p)N_0(z)\right) + \alpha_p\right] \tag{2.29}$$

In doped fibres with low Tm³⁺ concentration (e.g. <1 wt.%), the cross relaxation effect can be neglected. But it has been shown in ref. [70] that the incorporation of CR process in the rate equations can further improve the accuracy of the numerical modelling, even for a fibre with a doping concentration of 1.25 wt.% of Tm³⁺.

2.2.2 Pump configurations

Generally speaking, fibre lasers and fibre amplifiers are either core-pumped or cladding-pumped in practice. Figure 2.7 illustrates the principles of these two pumping schemes [71].
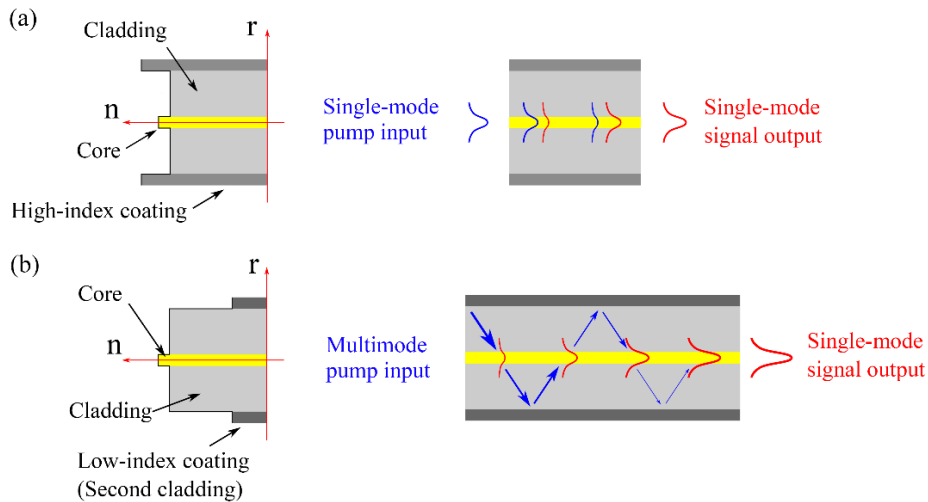
Figure 2.7. (a) Core-pumping and (b) cladding-pumping schemes for rare earth doped fibre lasers [71].

In the core-pumping scheme, both pump light and signal light propagate inside the fibre core. Pump absorption is high in the core-pumped structure due to the tight confinement of the pump light in the doped core, which helps in reducing the active fibre length. High-gain amplification is achievable with this approach because of the high population inversion and the large overlap between the pump and signal. However, the core-pumped configuration has a notable drawback that applicable pump power is largely limited by the small fibre core, as single-mode pump diodes normally have a sub-watt output power. Thus, the core-pumping approach is more suitable for building preamplifiers.

Double-clad fibres were invented in 1988 to address the unavailability of powerful single-mode pump diodes [72]. As shown in figure 2.7, a double-clad fibre has a doped core which guides the signal light and an inner cladding surrounded by a layer of low-index coating, which enables pump light propagation in the inner cladding. Therefore, high power multimode pump diodes can be used owing to the large dimension of the inner cladding, whereas the signal light can maintain single-mode operation and thus good beam quality. However, pump absorption in double-clad fibre is less efficient than that in a core-pumped fibre because some of the

pump light does not overlap with the core in a symmetric circular fibre geometry, which can be seen from figure 2.8 [71]. Pump absorption in double-clad fibres can be improved by breaking the circular symmetry in the fibre structure, for example a D-shaped cladding and an octagonal cladding. Overall, the cladding-pumping scheme is very promising for power-scaling the rare earth doped fibre lasers, regardless of the lower absorption efficiency in double-clad fibres.
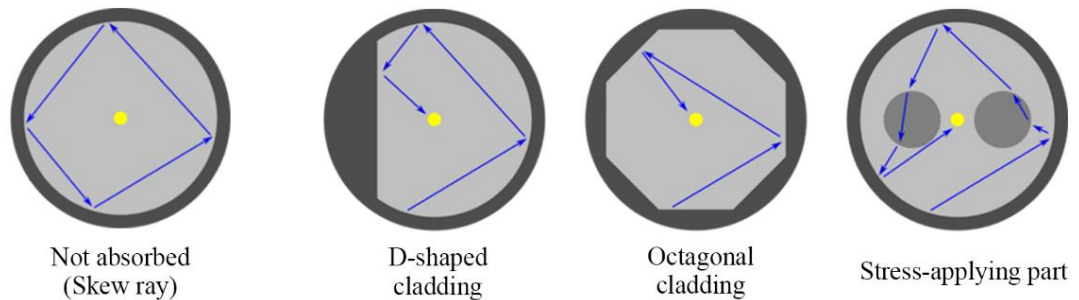
Figure 2.8. Pump propagation in double-clad fibres with different structures (circular, D-shaped, octagonal and PANDA) [71].

2.2.3   Master oscillator power amplifiers

Fiberised MOPA is a common approach to scale the laser output power with multiple advantages. The fundamental configuration of a MOPA can be summarised in figure 2.9 as a single-frequency seed followed by several high-gain amplifiers [5]. A low-power signal is gradually amplified to the desired high power level, usually after going through two pre-amplifiers and a final power amplifier. Isolators are inserted in between the amplifiers to avoid signal reflection which could be amplified in the backward direction and lead to optical damage of the system [5].
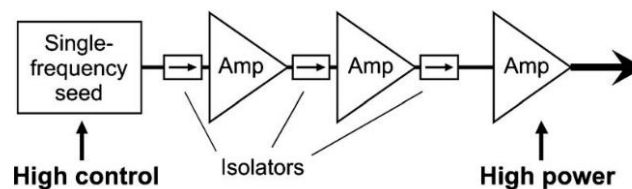
Figure 2.9. Schematic of a MOPA system [5].

To achieve the same required performance with a MOPA instead of a single high power laser, the MOPA approach has one apparent advantage that many output parameters like laser wavelength, pulse width and so on are decoupled from the

high power amplification with independent control of the seed [5]. Take gain-switched seed diode as an example. Gain-switching refers to the laser gain modulation by pump power. Laser emission occurs with a short time delay after applying high pump power to the laser. Radio-frequency (RF) signal generated from pulse generators is often used to modulate the gain in the case of gain-switching a laser diode. One can easily change the pulse duration, repetition rate and pulse peak power of the seed diode by changing the parameters of the applied electrical signal. These laser parameters are not affected in the subsequent amplification process of the MOPA.

Apart from the extra flexibility of a MOPA system, the optical components in the MOPA system do not have a harsh requirement for high power-handling capacity as compared to those components in a high-power laser resonator. However, the MOPA scheme inevitably complicates the setup with more adding parts and also increases the total cost. The noise level of a MOPA system tends to be higher [73], for each amplifier of the MOPA has unavoidable noise (e.g. noise from spontaneous emission) in addition to the shot noise. Despite these drawbacks, MOPA is still an appealing approach for many high-power laser applications.

2.3   Nonlinearities in fibres

As light propagates inside a silica fibre, the response of the fibre becomes nonlinear if the electromagnetic field is intense. Nonlinear effects can lead to spectral broadening and temporal distortion of light pulses. Hence it would be useful to briefly discuss the nonlinearities that might happen in a high power fibre laser.

Silica fibres do not exhibit any second-order nonlinear effects as a result of inversion symmetry. Therefore, the lowest-order nonlinear effects in fibres stem from the third order susceptibility $\chi^{(3)}$. Nonlinearities governed by $\chi^{(3)}$ can be divided into two categories, elastic processes and inelastic processes. Elastic processes refer to no exchanged energy between the optical field and the dielectric medium, whereas the optical field transfers some energy to the medium in inelastic processes [59].

2.3.1   Nonlinear Schrödinger Equation

It is preferential to illustrate the nonlinear Schrödinger equation before discussing any specific nonlinear effects, which helps better understandings of the nonlinear behaviours. Wave equation describing how optical pulses propagate inside fibres is derived from Maxwell's equations and given by Eq. 2.30 [59] in the time domain:

$$\nabla^2 \mathbf{E} - \frac{1}{c^2}\frac{\partial^2 \mathbf{E}}{\partial t^2} = \mu_0 \frac{\partial^2 \mathbf{P}_L}{\partial t^2} + \mu_0 \frac{\partial^2 \mathbf{P}_{NL}}{\partial t^2} \tag{2.30}$$

where $\mathbf{E}$ is the electric field, $\mathbf{P}$ is the induced electric polarisation, c is the speed of light in vacuum and μ_0 is the vacuum permeability. The induced polarisation can be viewed as a sum of the linear part $\mathbf{P}_L$ and the nonlinear part $\mathbf{P}_{NL}$ [59], when only the third-order nonlinear effects are considered in silica fibres in the wavelength range of 0.5–2 µm.

$$\mathbf{P} = \boldsymbol{P}_L + \boldsymbol{P}_{NL} \tag{2.31}$$

Several simplifying assumptions are set up to solve the wave equation. First, take the scalar approach by assuming that light maintains its polarisation along the fibre. Second, $\boldsymbol{P}_{NL}$ is treated as a small perturbation to $\boldsymbol{P}_L$ because nonlinear changes are minor in the refractive index. Third, it is justified to assume light to be quasi-monochromatic when pulses are no shorter than 0.1 ps [59]. Therefore, the Fourier transform of the electric field can be defined as [59]:

$$\tilde{E}(\boldsymbol{r}, \omega - \omega_0) = \int_{-\infty}^{\infty} E(\boldsymbol{r}, t) exp[i(\omega - \omega_0)t] dt \tag{2.32}$$

where ω_0 is the carrier frequency.

Equation 2.32 can be solved by separating variables [59]:

$$\tilde{E}(\boldsymbol{r}, \omega - \omega_0) = F(x, y)\tilde{A}(z, \omega - \omega_0) exp(i\beta_0 z) \tag{2.33}$$

where β_0 represents the wave number, $F(x, y)$ is the modal distribution and $\tilde{A}(z, \omega)$ is a slowly varying function of z. The wave number and the modal distribution can be obtained by solving the eigenvalue equation. Explanations for the modal distribution and eigenvalue equation can be found on page 30 of ref. [59].

The inverse Fourier transform of $\tilde{A}(z, \omega)$ is expressed as [59]:

$$A(z, t) = \frac{1}{2\pi} \int_{-\infty}^{\infty} \tilde{A}(z, \omega - \omega_0) exp[-i(\omega - \omega_0)t] d\omega \qquad (2.34)$$

The slowly varying function $A(z, t)$ satisfies the following equation (Eq. 2.35), which is referred to as the nonlinear Schrödinger equation (NLS) [59].

$$\frac{\partial A}{\partial z} + \beta_1 \frac{\partial A}{\partial t} + \frac{i\beta_2}{2} \frac{\partial^2 A}{\partial t^2} + \frac{\alpha}{2} A = i\gamma |A|^2 A \qquad (2.35)$$

where β_1 is the reciprocal of the group velocity and β_2 is the GVD parameter, as defined in Eq. 2.9 and Eq. 2.10. α represents the fibre loss and γ is the nonlinear parameter.

$$\gamma = \frac{n_2 \omega_0}{c A_{eff}} \qquad (2.36)$$

n is the linear refractive index dependent on the frequency whereas n_2 is the nonlinear refractive index.

$$\tilde{n}(\omega, |E|^2) = n(\omega) + n_2 |E|^2 \qquad (2.37)$$

The effective area A_{eff} is defined as [59]:

$$A_{eff} \frac{(\iint_{-\infty}^{\infty} |F(x,y)|^2 dx dy)^2}{\iint_{-\infty}^{\infty} |F(x,y)|^4 dx dy} \qquad (2.38)$$

The nonlinear Schrödinger equation describes how optical pulses propagate in fibres where loss, dispersion and nonlinear effects are all considered. Fibre loss is usually neglected in discussion. Either dispersion or nonlinearities may dominate the pulse propagation, depending on the initial pulse width T_0 and the incident peak power P_0 [59]. It is useful to introduce the dispersion length L_D and the nonlinear length L_{NL} to help illustrate the pulse evolution under the influence of dispersion and nonlinearities.

Rewrite Eq. 2.35 into [59]:

$$i\frac{\partial A}{\partial z} = -\frac{i\alpha}{2}A + \frac{\beta_2}{2}\frac{\partial^2 A}{\partial T^2} - \gamma|A|^2 A \qquad (2.39)$$

where $T = t - z/v_g$.

The slowly varying amplitude of the pulse envelope A can be expressed with a normalised time scale and a normalised amplitude U [59].

$$A(z,\tau) = \sqrt{P_0}exp(-\alpha z/2)U(z,\tau) \qquad (2.40)$$

$$\tau = \frac{T}{T_0} = \frac{t-z/v_g}{T_0} \qquad (2.41)$$

$$L_D = \frac{T_0^2}{|\beta_2|} \qquad (2.42)$$

$$L_{NL} = \frac{1}{\gamma P_0} \qquad (2.43)$$

The relative magnitudes of fibre length L, dispersion length L_D and nonlinear length L_{NL} indicate how dispersion and nonlinear effects affect the pulse propagation. Pulses are propagating in a dispersion-free and nonlinearities-free regime when $L \ll L_D$ and $L \ll L_{NL}$. When $L \sim L_D$ and $L \ll L_{NL}$, pulse evolution is governed by the dispersion rather than nonlinearities. On the contrary, nonlinear effects will dominate over dispersion in pulse propagation along the fibre when $L \ll L_D$ and $L \sim L_{NL}$. When the fibre length is comparable to both L_D and L_{NL} ($L \sim L_D, L \sim L_{NL}$), dispersive and nonlinear effects make influences on the pulse propagation at the same time. The interaction between the dispersion and the nonlinearities can give rise to interesting phenomena such as fibre solitons and supercontinuum generation [59].

GVD parameter and nonlinear refractive index of thulium doped fibres can vary with the fibre design and fibre composition. Kharitonov *et al.* have characterised the dispersion and Kerr nonlinearity of the commercial TmDF200 fibre [74]. A GVD parameter of -18.74 $ps^2 \cdot km^{-1}$ was measured at 1980 nm and a nonlinear refractive index was estimated to be 3.25–3.55×10^{-20} $m^2 \cdot W^{-1}$ at 2 µm. These numbers can be used for a rough estimation of the fibre behaviour despite the variability of GVD parameter and nonlinear refractive index in different fibres. The dispersion length L_D is estimated to be >100 km for 50-ps pulses, so the impact of dispersion on

TDFAs with "metre-scale" device lengths is small. Nonlinear parameters for different thulium doped fibres used in this thesis are calculated and summarised in table 2.1, using Eq. 2.36 and $n_2 = 3.55 \times 10^{-20} \, m^2 \cdot W^{-1}$.

Fibre	MFD (μm)	A_{eff} (μm²)	γ (W$^{-1} \cdot$ km^{-1})	L_{NL} @ P_0 (m)
TmDF200	6	30	3.8	26.3 @10 W
B0155_L10146	8.6	59	1.94	5.2 @100 W
ORC_DCF	12.4	121	0.95	1.1 @1 kW
LMA-TDF-25/250	22	387	0.29	3.5 @1 kW

Table 2.1. Estimated nonlinear parameters for different thulium doped fibres used in this thesis (ʌ=1.95 μm).

2.3.2 Self-phase modulation

Self-phase modulation (SPM) is a widely studied elastic nonlinear effect caused by nonlinear refraction, namely the intensity dependence of the refractive index. It generally leads to the spectral broadening.

When the fibre length is much shorter than the dispersion length ($L \ll L_D$) and SPM plays a dominant role in the pulse propagation, normalised amplitude $U(z, \mathrm{T})$ satisfies Eq. 2.44 and Eq. 2.45 [59].

$$\frac{\partial U}{\partial z} = \frac{ie^{-\alpha z}}{L_{NL}} |U|^2 U \tag{2.44}$$

$$U(L, \mathrm{T}) = U(0, T)\exp[i\phi_{NL}(L, T)] \tag{2.45}$$

SPM causes a nonlinear phase shift that can be defined as [59]:

$$\phi_{NL}(L, T) = |U(0, T)|^2 (L_{eff}/L_{NL}) \tag{2.46}$$

with the effective length defined as [59]:

$$L_{eff} = [1 - exp(-\alpha L)]/\alpha \tag{2.47}$$

The nonlinear phase shift can be equally expressed as the second term on the right in Eq. 2.48.

$$\phi = (n + n_2|E|^2)k_0 L \tag{2.48}$$

As shown by the above equations (Eq. 2.46 and Eq. 2.48), the SPM-induced phase shift is intensity dependent and increases with the fibre length. The spectral broadening by SPM derives from the temporally varying nonlinear phase shift, which implies instantaneous frequency differences across the pulse [59].

$$\delta\omega(T) = -\frac{\partial\phi_{NL}}{\partial T} = -\left(\frac{L_{eff}}{L_{NL}}\right)\frac{\partial}{\partial T}|U(0,T)|^2 \qquad (2.49)$$

The time dependence of $\delta\omega$, also known as frequency chirping, manifests as the generation of new frequency components, thereby broadening the initial spectrum. The SPM-broadened spectrum strongly depends on the input pulse shape and the initial chirp. However, it becomes necessary to take the GVD into consideration for ultrashort pulses. The interplay between SPM and GVD can either assist the formation of optical solitons in the anomalous-dispersion regime or compress the pulse width in the normal-dispersion regime [59].

In a fibre amplifier, the input field can suffer from severe SPM-induced spectral broadening, since pulses are amplified rather than attenuated along the fibre. Thus, the gain coefficient g will substitute for the loss parameter α in Eq. 2.47, resulting in an effective length defined as $L_{eff} = [exp(gL) - 1]/g$, which can become much larger than the amplifier length L [59].

Consider that an unchirped Gaussian pulse with a peak power of P_0 is injected into an LMA-fibre-based TDFA for amplification. Assuming that 20-dB gain is achieved at the output of 1-m-long TDF, the effective length would be ~21.5 m. An input peak power of ~1 kW is required to achieve 2π nonlinear phase shift in this fibre ($\gamma = 0.29 \ W^{-1} \cdot km^{-1}$).

2.3.3   Four-wave mixing

Four-wave mixing (FWM) is a parametric process which involves nonlinear interaction among four optical waves. This phase-sensitive, polarisation-dependent process can be described as [59]:

$$\omega_3 + \omega_4 = \omega_1 + \omega_2 \qquad (2.50)$$

$$\Delta k = \varphi_3 + \varphi_4 - \varphi_1 - \varphi_2 \qquad (2.51)$$

where $\varphi_i(i = 1, 2, 3, 4)$ is the propagation constant of an optical wave and Δk represents the phase mismatch among the interacting waves.

When FWM occurs, two photons at frequencies ω_1 and ω_2 are annihilated with simultaneous creation of two new photons at frequencies ω_3 and ω_4. Phase-matching ($\Delta k = 0$) is required to achieve efficient FWM in fibres.

In a general case, the frequencies of the two pump photons are different ($\omega_1 \neq \omega_2$). However, FWM can also be initiated in fibres with two pump photons at the same frequency ($\omega_1 = \omega_2$), which is referred to as degenerate FWM [59].

Hence the Stokes and anti-Stokes waves at frequencies ω_3 and ω_4 can be generated from noise, when a pump beam is injected into the fibre and the phase-matching condition is satisfied. Furthermore, if a weak signal at frequency ω_3 is launched into the fibre along with the pump beam, the signal (ω_3) is amplified while an idler (ω_4) is created to conserve the photon energy [59].

The gain responsible for this amplification is called the parametric gain and defined as [59]:

$$g = \sqrt{(\gamma P_0 r)^2 - (\kappa/2)^2} \tag{2.52}$$

$$\kappa = \Delta k + \gamma(P_1 + P_2) \tag{2.53}$$

where κ is the effective phase mismatch incorporating the nonlinear phase shifts induced by SPM, P_1 and P_2 are the incident peak powers of pump waves ω_1 and ω_2.

The parameter r and P_0 are introduced as [59]:

$$r = 2(P_1 P_2)^{1/2}/P_0 \tag{2.54}$$

$$P_0 = P_1 + P_2 \tag{2.55}$$

2.3.4   Modulation instability

Many nonlinear systems exhibit an instability that can be interpreted as modulation of the steady state which results from the interaction between the nonlinearities and the dispersion. The following deduction considers the propagation of CW light instead of pulses in fibres, but the conclusions are also applicable to the quasi-CW situation that the pulse duration is much longer than the modulation period (~1 ps) [75].

The amplitude $A(z,T)$ is time independent if fibre loss is overlooked and it is given by [59]:

$$A = \sqrt{P_0}\exp(i\phi_{NL}) \qquad (2.56)$$

A small perturbation term a is exerted on the propagation of CW light in fibres to examine with linear stability analysis whether the steady state remains stable [59].

$$A = (\sqrt{P_0} + a)\exp(i\phi_{NL}) \qquad (2.57)$$

With the nonlinear Schrödinger equation, we can obtain

$$i\frac{\partial a}{\partial z} = \frac{\beta_2}{2}\frac{\partial^2 a}{\partial T^2} - \gamma P_0(a + a^*) \qquad (2.58)$$

The solution of Eq. 2.58 is [59]:

$$a(z,T) = a_1 \exp[i(Kz - \Omega T)] + a_2\exp[-i(Kz - \Omega T)] \qquad (2.59)$$

where K and Ω are the wave number and the perturbation frequency respectively.

$$K = \pm\frac{1}{2}|\beta_2\Omega|[\Omega^2 + sgn(\beta_2)\Omega_c^2]^{1/2} \qquad (2.60)$$

$$\Omega_c^2 = \frac{4\gamma P_0}{|\beta_2|} = \frac{4}{|\beta_2|L_{NL}} \qquad (2.61)$$

In the normal dispersion regime where $\beta_2 > 0$, the wave number K is real in all conditions and therefore the steady state maintains the stability against small perturbations. In contrast, the perturbation term a could grow exponentially with z when K becomes imaginary for $|\Omega| < \Omega_c$ in the anomalous dispersion regime ($\beta_2 < 0$), so the steady-state situation is no longer stable and modulation instability (MI) appears [59].

Note that the actual wave number and the frequency of perturbation are $\beta_0 \pm K$ and $\omega_0 \pm \Omega$. The manifestations of MI are creating two spectral sidebands ($\omega_0 + \Omega$ and $\omega_0 - \Omega$) in the frequency domain and breaking up the CW or quasi-CW radiation into a train of ultrashort pulses in the time domain [59].

When MI occurs, frequency components within the gain spectrum of MI can be amplified. The gain is expressed as [59]:

$$g(\Omega) = |\beta_2\Omega|\sqrt{\Omega_c^2 - \Omega^2} \qquad (2.62)$$

The gain exists only when the frequency of perturbation meets the condition $|\Omega| \leq |\Omega_c|$. It reaches maximum when $\Omega = \pm\frac{\Omega_c}{\sqrt{2}}$ [59].

$$g_{max} = \frac{1}{2}|\beta_2|\Omega_c^2 = 2\gamma P_0 \qquad (2.63)$$

It can be concluded from Eq. 2.61 and Eq. 2.62 that the locations of MI peaks change with the incident peak power.

Thulium doped fibre sources are prone to the modulation instability as a result of the inherent anomalous fibre dispersion at 2 μm. Figure 2.10 plots the MI gain spectrum of LMA thulium doped fibres with a 25-μm core diameter and a nonlinear parameter of 0.29 $W^{-1} \cdot km^{-1}$, assuming a laser wavelength at 1950 nm.
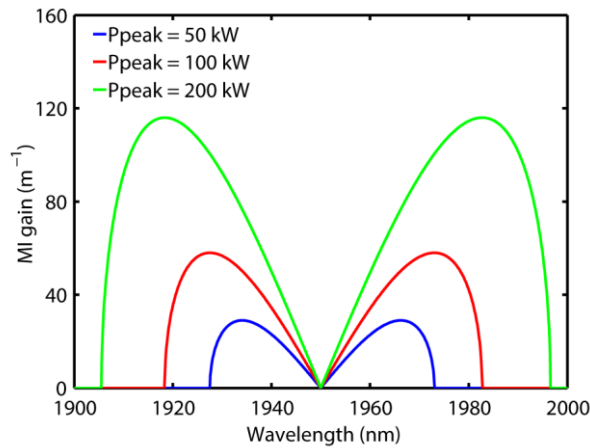
Figure 2.10. Calculated MI gain spectrum for an LMA thulium doped fibre.

MI can be interpreted as an FWM process that is phase-matched by SPM. When the spectral broadening induced by SPM is large enough, the SPM-generated frequency components within the MI gain bandwidth can act as a probe that is amplified by MI [59], as indicated in figure 2.10.

2.3.5   Stimulated Raman scattering

Stimulated Raman scattering (SRS) is an inelastic nonlinear process associated with optical phonons. Two optical fields, termed pump and Stokes, are involved in this process. A pump photon is annihilated to create a photon at a lower frequency (Stoke wave) and a phonon, the combined energy and momentum of which have to abide by the conservation law. Likewise, a higher-frequency photon (anti-Stoke

32

wave) can be created if a phonon and a pump photon are annihilated. Thus, new spectral components are generated in these two processes [59].

The SRS process can be described by the following equations [59]:

$$\frac{dI_s}{dz} = g_R I_p I_s - \alpha_s I_s \tag{2.64}$$

$$\frac{dI_p}{dz} = -\frac{\omega_p}{\omega_s} g_R I_p I_s - \alpha_p I_p \tag{2.65}$$

where the intensities of pump and the Stokes are represented by I_p and I_s, g_R is the Raman gain coefficient, and α_p and α_s account for fibre losses at the pump and the Stokes frequencies.

The Raman gain coefficient g_R depends on the fibre composition and can vary significantly with different dopants. For fused silica fibres, $g_R \approx 6 \times 10^{-14}$ m/W at 2 μm. Typical Raman gain spectrum measured in silica fibres is shown in figure 2.11, with an example pump wavelength at 1950 nm. Raman scattering in fused silica has a distinct feature that the whole gain bandwidth extends over a large frequency range, reaching up to 40 THz. The Raman gain peaks at a Stoke frequency downshifted from the pump frequency by about 13 THz [59].
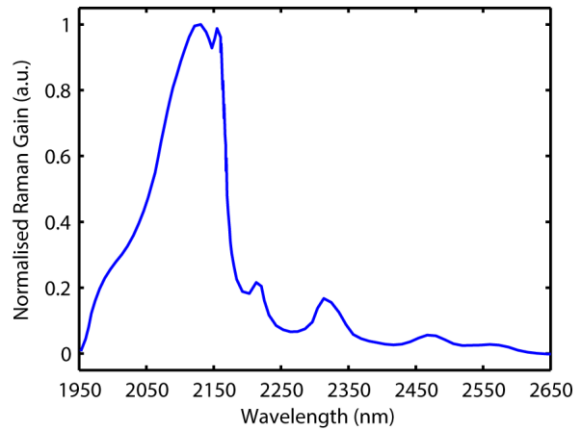
Figure 2.11. Normalised Raman gain in fused silica for a pump wavelength of 1950 nm.

A solution to Eq. 2.64 can be expressed as [59]:

$$I_s(L) = I_s(0) \exp(g_R I_0 L_{eff} - \alpha_s L) \tag{2.66}$$

There exists a pump intensity threshold for the Raman effect. It is defined as the input pump power at which the Stokes power becomes equal to the pump power at the output [59]:

$$P_s\,(L) = P_p\,(L) = \ P_0\,exp\big(-\alpha_p L\big) \qquad (2.67)$$

where P_0 is the incident peak power.

An empirical rule to estimate the pump threshold is given by [76]:

$$P_{th} = \ \frac{16 \cdot A_{eff}}{g_R L_{eff}} \qquad (2.68)$$

According to Eq. 2.68, the critical pump threshold for a TDFA can be estimated. Table 2.2 summarises the estimated critical pump thresholds for the TDFAs demonstrated in this thesis. For example, SRS is expected in the LMA TDFA with a device length of 1.3 m, when the peak power P_0 of incident pulses exceeds a critical value of ~2.3 kW.

Fibre	A_{eff} (μm^2)	Gain (dB)	g (m^{-1})	L (m)	L_{eff} (m)	P_{th} (W)
TmDF200	30	~40	0.76	12	~12020	0.66
B0155_L10146	59	~16	3.0	1.2	11.8	1300
ORC_DCF	121	10.6	0.97	2.5	10.6	~3000
LMA-TDF-25/250	387	22.6	4.0	1.3	45.0	~2300

Table 2.2. Estimated critical SRS thresholds for the TDFAs presented in this thesis.

2.3.6   Supercontinuum generation

Supercontinuum generation is a nonlinear process which yields light with a broad spectral bandwidth. This phenomenon was first observed in bulk materials around 1970 [77] and then widely studied in optical fibres since the first demonstration of SCG in fibres in 1976 [78]. A brief introduction to supercontinuum generation in fibres is provided here, including the underlying physical mechanism and the general design concern for making a supercontinuum source. Comprehensive discussions about SC generation can be found in ref. [59] and ref. [79].

Multiple nonlinear effects can be involved in supercontinuum generation and the dominant processes include SPM, MI, FWM and SRS. Pump condition divides SC generation into two different regimes, femtosecond-pumped and long-pulse-pumped (picosecond, nanosecond and even CW). On the other hand, fibre dispersion and its wavelength dependence should also be considered due to the broad spectral coverage of SC generation.

When a fibre is pumped by femtosecond pulses in the anomalous dispersion regime, pulse propagation is perturbed by high-order dispersive and nonlinear effects, which leads to high-order solitons breaking up into fundamental solitons. This phenomenon is referred to as soliton fission [59]. A characteristic length called 'fission length' is introduced to describe the fission point after which the breakup of the input pulse starts. Fission length can be expressed approximately as $L_{fiss} \sim L_D/N$, where $N^2 = L_D/L_{NL}$ is the soliton order of the input pulse [79]. Hence in this case, supercontinuum generation is initiated by soliton fission, followed by Raman soliton self-frequency shift (SSFS) to longer wavelengths [79]. The soliton has such a wide spectrum that its low-frequency components can amplify its high-frequency components through Raman effect. Meanwhile, soliton inside the fibre can shed a part of its energy to a dispersive wave (DW) if the dispersive wave has the same phase velocity as that of the soliton [59].

Femtosecond-pumped SC generation in the normal dispersion regime is different from that in the anomalous dispersion regime. Since no soliton is formed in the normal dispersion regime, supercontinuum generation is dominated by the high-peak-power-induced SPM effect in the fibre [79]. However, if the initial broadening from SPM generates new spectral contents in the anomalous dispersion regime, these new frequency components can undergo similar soliton dynamics [79].

Soliton fission will not happen in SC generation pumped by high-peak-power pulses with longer duration in the anomalous dispersion regime, due to a very large soliton order ($N \gg 10$) as well as an increased fission length [79]. Take picosecond-pumping a fluoroindate fibre as an example. The fluoroindate fibre has a core diameter of 9 μm and core NA of 0.26. The pump pulse has a duration of 35 ps with 100-kW peak power. Relevant parameters are calculated and summarised in table 2.3. It can be seen from the calculation that the soliton order is extremely large with a fission length of more than 20 m. Consequently, the initial phase of pulse propagation inside the fibre will be dominated by MI or FWM rather than soliton fission. But the initial MI dynamics will also lead to the breakup of pump pulses and formation of a lot of sub-pulses. These sub-pulses subsequently evolve

into solitons in the fibre, after which the previously mentioned soliton dynamics (SSFS, DW) can engage in the supercontinuum generation [79].

λ_p (nm)	$n_2(m^2 \cdot W^{-1})$	A_{eff} (μm^2)	γ ($W^{-1} \cdot m^{-1}$)	L_{NL} @ P_0 (m)
1950	3.2×10^{-20} [80]	48	2.13×10^{-3}	4.7×10^{-3}
$D(ps/(nm \cdot km))$	$\beta_2(ps^2/km))$	$L_D(m)$	N	L_{fiss} (m)
5	-10.1	1.2×10^5	5053	23.7

Table 2.3. An example of picosecond-pumped SC generation in fluoride fibres and its relevant parameters.

With long pump pulses in the normal dispersion regime, spectral broadening arises primarily from either FWM or Raman scattering. When the pump resides in the deep normal dispersion regime, Raman effect dominates over FWM because of the great difficulty in satisfying the phase-matching condition. When the pump wavelength is tuned closer to the ZDW, FWM plays an increasingly important role in SC generation owing to a higher parametric gain than the Raman gain [79].

Below discusses the general design concern for supercontinuum generation in terms of pump wavelength, fibre length, output bandwidth and spectral flatness. It is favourable to pump in the vicinity of the fibre ZDW for the maximum spectral broadening due to the combined nonlinear effects such as SSFS and DW. On the other hand, a pump wavelength which is close to the desirable output wavelengths is preferred for a better power conversion efficiency. Powerful pump source at a particular wavelength might also be useful for producing supercontinuum with high output power.

Femtosecond pumping allows the usage of a short piece of nonlinear fibre while long-pulse pumping usually demands a longer fibre length. The fundamental limitation on the output spectral bandwidth of a supercontinuum is the intrinsic loss of the fibre material, but the pump wavelength and fibre dispersion also have a significant impact on the spectral broadening. As for spectral flatness, it is largely dependent on the fibre dispersion profile. By modifying the waveguide dispersion, it is possible to shift the fibre ZDW and engineer the dispersion profile (e.g. tapered fibres) so as to achieve the wanted supercontinuum generation.

2.4   Nonlinear frequency conversion in crystals

2.4.1 $\chi^{(2)}$ nonlinearity basics

As mentioned in section 2.3.1, P is the induced polarisation when light is applied to a medium. The total induced polarisation has a linear part P_L and a nonlinear part P_{NL}. When the applied electric field is weak, the nonlinear part can be ignored and the polarisation P can be described as [81]:

$$P(t) = \epsilon_0 \chi^{(1)} E(t) \tag{2.69}$$

Where ϵ_0 is the vacuum permittivity and $\chi^{(1)}$ is the linear susceptibility.

However, the nonlinear part becomes progressively important in the contribution to the total induced polarisation when the applied electric field is getting intense. Thus, P is written in a more general form as [81]:

$$P = \epsilon_0 [\chi^{(1)} E(t) + \chi^{(2)} E^2(t) + \chi^{(3)} E^3(t) + \cdots] \tag{2.70}$$

where $\chi^{(j)}$ is the jth order susceptibility.

In non-centrosymmetric crystal materials, the second order susceptibility $\chi^{(2)}$ is responsible for nonlinear effects such as second-harmonic generation, sum-frequency generation (SFG) and difference-frequency generation (DFG) [81, 82]. These frequency-mixing processes are diagrammatically illustrated by figure 2.12 [83].
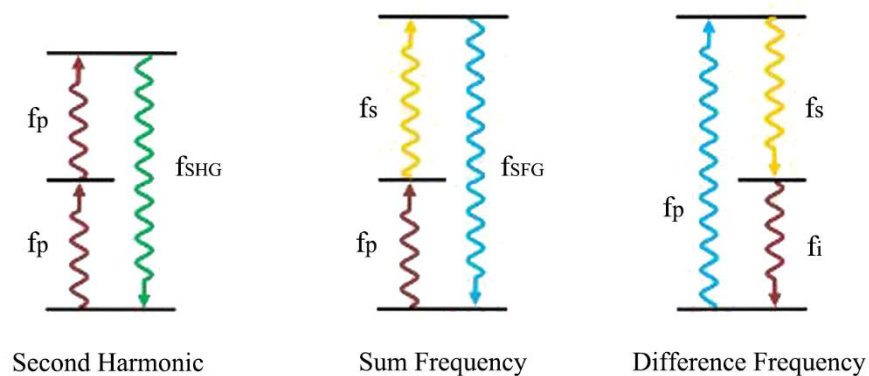
Figure 2.12. Diagrammatic representations of second-harmonic generation, sum-frequency generation and difference-frequency generation [83].

As a result of photon energy conservation, the frequency-mixing processes can be represented by a simple relationship [82]:

$$f_1 + f_2 = f_3 \tag{2.71}$$

At the photon level, SHG can be regarded as the annihilation of two photons having the same frequency ($f_1 = f_2 = f_p$), accompanied with instantaneous creation of a frequency-doubled photon ($f_{SHG} = f_3 = 2f_p$). In SFG, two photons with different frequencies ($f_1 = f_s$, $f_2 = f_p$) are annihilated to generate a new photon with frequency at $f_{SFG} = f_3$. The opposite situation occurs in DFG, where the energy of a single pump photon ($f_3 = f_p$) is divide into two portions, one for a signal photon with frequency at $f_1 = f_s$, the other for an idler photon with frequency at $f_2 = f_i$. Therefore, frequency-mixing process is particularly attractive to laser generation at exotic wavelengths due to its ability to generate new frequency components [82]. The efficiency of such nonlinear frequency conversion largely depends on the phase relationship among the interacting waves. Phase-matching ($\Delta k = k_3 - k_2 - k_1 = 0$) is required to realise efficient frequency-mixing.

2.4.2 Second harmonic generation

In the following discussion about SHG, the fundamental and the second-harmonic waves are labelled by $n = 1$ and $n = 2$, respectively.

$$\omega_1 = \omega \tag{2.72}$$

$$\omega_2 = 2\omega \tag{2.73}$$

$$\Delta k = k_2 - 2k_1 = 2\omega(n_2 - n_1)/c \tag{2.74}$$

In the low-depletion regime where the fundamental beam remains essentially un-depleted, the second-harmonic intensity can be obtained by solving the wave equations [82]:

$$I_2(z) = \frac{(\omega_2 \chi^{(2)} I_1)^2}{8\varepsilon_0 c^3 n_2 n_1^{\,2}} \, sinc^2 \left\{ \frac{\Delta kz}{2} \right\} \tag{2.75}$$

It can be seen from Eq. 2.75 that I_2 grows as the square of both the second order susceptibility and the fundamental intensity I_1. When phase-matching, the sinc function goes to unity and I_2 increases as the square of the distance. When $\Delta k \neq 0$, Eq. 2.75 is rewritten as [82]:

$$I_2(z) = \frac{(\omega_2 \chi^{(2)} I_1)^2}{2\varepsilon_0 c^3 n_2 n_1{}^2} \frac{sin^2\{\Delta k z/2\}}{\Delta k^2} \tag{2.76}$$

In this case, the second-harmonic intensity oscillates with the propagation distance, as shown in figure 2.13. The intensity reaches the maximum for the first time at a distance where

$$z = L_{coh} = \frac{\pi}{|\Delta k|} \tag{2.77}$$

which is known as the coherence length [82].
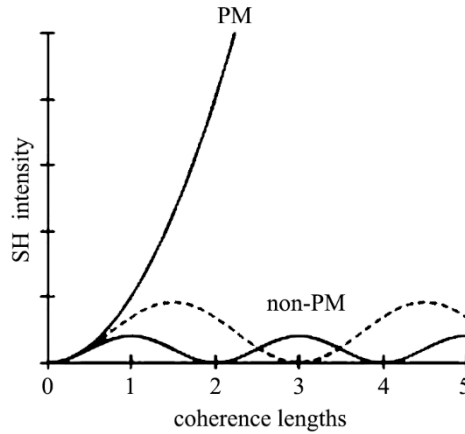
Figure 2.13. Second-harmonic intensity as a function of distance under phase-matching (PM) and two non-phase-matching (non-PM) conditions. The dotted line has a coherence length 1.5 times larger than the solid line. [82].

However, Eq. 2.75 and Eq. 2.76 do not apply to the case where significant energy is transferred from the fundamental wave to the second-harmonic wave. In the high-depletion regime, Manley-Rowe relations must be included in solving the wave equations. Manley-Rowe relation is a statement of photon energy conservation and expressed as [82]:

$$\frac{d\phi_1}{dz} = -2\frac{d\phi_2}{dz} \tag{2.78}$$

The inclusion of Manley-Rowe relation complicates the coupled-wave equations and their solutions, discussion of which is beyond the scope of this thesis. But a detailed deduction can be found in the literatures [81, 82].

The conversion efficiency of SHG is defined as the ratio of the second-harmonic output power to the fundamental input power.

$$\eta_{eff} = \frac{P_2(z=L)}{P_1(z=0)} \qquad (2.79)$$

where L is the length of a nonlinear crystal [81].

It can be inferred from the equations (Eq. 2.75 and Eq. 2.76) that the conversion efficiency depends on the intensity of the fundamental beam. Therefore, an optimally focused beam should yield a maximum conversion efficiency. To achieve this, there are two basic rules to follow. First of all, the focused beam should always have a maximum intensity below the damage threshold of the crystal, which means a minimum limitation on the focal spot size r_0. Second, the focal spot size is chosen so that the confocal parameter b of the beam equals to the crystal length L [81].

$$b = \frac{2\pi r_0^2}{\lambda_1/n_1} = L \qquad (2.80)$$

where λ_1 and n_1 are the wavelength of the fundamental beam in vacuum and the refractive index of the nonlinear crystal, respectively.

2.4.3   Optical parametric generation and amplification

Optical parametric generation and amplification can be considered as the special cases of DFG, which involve the interaction among the pump, signal and idler waves. The frequency relationship is written as [82]:

$$f_p = f_s + f_i \qquad (2.81)$$

Schematics of an OPG and an OPA are depicted in figure 2.14. As shown in the figure, the structure of an OPG is simple that just requires an input pump wave. A large combination of signal and idler wavelengths can satisfy the frequency relationship in Eq. 2.81. However, the emission wavelengths of signal and idler are never random in an OPG and they are always determined by the phase-matching condition. There are broadband background noises when the pump is launched

into the OPG and these noises could initiate the frequency conversion as long as phase-matching condition is satisfied [82]. As a result, the spectral bandwidths of the signal and idler from an OPG are broad, with the most efficient conversion at the central wavelengths.

As compared to the OPG, an OPA requires a pump beam and a signal beam as the seed. Because of the seed injection, the output bandwidths of the OPA signal and idler are often much narrower in comparison with the OPG case [82]. Due to their dependence on phase-matching, OPG and OPA exhibit wavelength tunability, which is usually enabled by birefringent phase-matching or quasi phase-matching (QPM) in crystals [82].
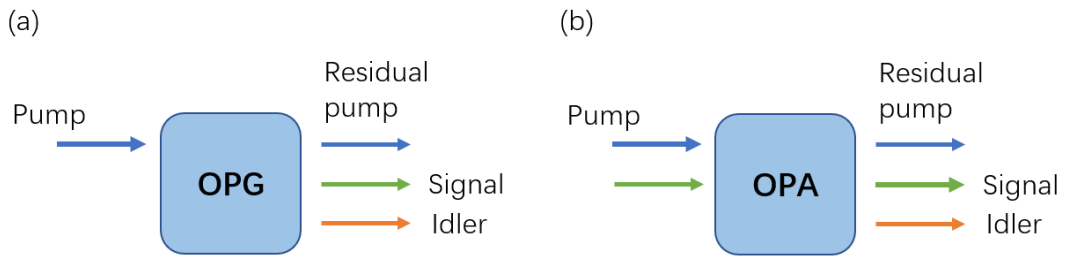
Figure 2.14. Schematics of an (a) optical parametric generator and (b) optical parametric amplifier.

In optical parametric process, the pump, signal and idler waves can be described by the following equations [81]:

$$\frac{dE_p}{dz} = j \frac{\omega_p d}{n_p c} E_s E_i e^{-j\Delta kz} \tag{2.82}$$

$$\frac{dE_s}{dz} = j \frac{\omega_s d}{n_s c} E_p E_i^* e^{j\Delta kz} \tag{2.83}$$

$$\frac{dE_i}{dz} = j \frac{\omega_i d}{n_i c} E_p E_s^* e^{j\Delta kz} \tag{2.84}$$

where d is the effective nonlinear coefficient of a crystal.

When the pump is assumed un-depleted, the above coupled equations can be solved for the signal and idler [81]:

$$E_s(z) \propto \cosh(gz) \tag{2.85}$$

$$E_i(z) \propto \sinh(gz) \tag{2.86}$$

$$g = \sqrt{\Gamma^2 - (\frac{\Delta k}{2})^2} \tag{2.87}$$

$$\Gamma = \frac{8\pi^2 d^2}{n_p n_s n_i \varepsilon_0 c \lambda_s \lambda_i} I_p \qquad (2.88)$$

where g is the parametric gain coefficient. When $\Delta k \neq 0$, the gain is reduced according to Eq. 2.87.

Consider an OP-GaAs OPA pumped by 1952-nm light, producing signal at 2650 nm and corresponding idler at 7440 nm. The refractive indexes of GaAs are 3.3408, 3.3187 and 3.2864 at the pump, signal and idler wavelengths, respectively [84]. The effective nonlinear coefficient d is ~59 pm/V for small-signal amplification [85]. Assuming a pump intensity of ~230 MW/cm², the small-signal gain is expected to be ~55 dB.

2.5   Conclusion

This chapter discusses the theoretical background knowledge which underpins the experimental work presented in this thesis. I have first reviewed the fundamentals of thulium doped fibres and the amplification theory, which provide guidance for developing high-power thulium doped fibre MOPA in chapter 3. I have also briefly discussed the nonlinear effects in fibres, which help illustrate the experimental results in the following chapters. Nonlinearities based on $\chi^{(2)}$ susceptibility such as SHG and DFG are also included, which form the basis for the work in chapter 5 and chapter 6.

Chapter 3 High power gain-switched diode-seeded picosecond thulium doped fibre MOPA system

3.1 Introduction

A wide range of applications such as gas sensing, material processing and nonlinear frequency conversion have growing demands for powerful and versatile 2-μm lasers. Thulium doped fibre lasers prove to be outstanding candidates for a wide wavelength-tuning range covering 1.65-2.05 μm, with flexible configurations and exceptional stability.

Thulium doped fibre lasers delivering nanosecond pulses with high average output powers are desirable for laser processing of polymers and could be easily implemented by cascaded amplifications. A nanosecond-pulsed thulium-doped LMA-fibre MOPA system with peak power of 12.1 kW is recently reported producing an average output power scalable from 150 W to 238 W [19]. However, scaling the peak power of nanosecond-pulsed TDFLs has proved to be challenging because of energy saturation as well as limitation imposed by fibre nonlinearities. Peak power up to MW level at a very low repetition rate is demonstrated using a large-core PCF rod as the gain medium. For instance, 6.5-ns pulses with a peak power of ~1 MW at 1-kHz repetition rate was demonstrated from a thulium-doped photonic-crystal-fibre amplifier with an 80-μm core diameter [22].

In contrast, TDFLs which generate femtosecond pulses with low average power but exceptionally high peak power are usually achieved from more complicated structures incorporating dispersion management and pulse compression. Femtosecond pulses with a peak power in excess of 200 MW were generated from a CPA system based on a thulium-doped large-pitch rod fibre with a mode field diameter (MFD) of 65 μm [86]. Picosecond-pulsed TDFLs with simpler system architectures appear as a good alternative if one wants a trade-off between average power and peak power. A thulium-doped PCF-rod-type amplifier with an 80-μm core diameter produced 520-ps pulses with an average power of 6 W and a record peak power of 230 kW without external pulse compression [31]. However, this record peak power is substantially lower than the power level achieved in thulium-doped PCF-based amplifiers operating in the nanosecond or femtosecond regime.

Flexible, high-peak-power thulium doped fibre lasers are of great interests to nonlinear frequency conversion applications. In this chapter, we present the work of the generation of high power picosecond pulses from a gain-switched diode-seeded thulium doped fibre MOPA system. Although similar technique has been investigated in literatures ([30, 87]) before, there existed limitations in these works. In ref. [87], 100 kW of peak power was demonstrated from a thulium doped fibre MOPA with a gain-switched seed at 2008 nm. However, the signal OSNR was just 28 dB at the output of the final-stage amplifier, with ASE peak at ~1970 nm. The build-up of ASE was pronounced in this case because the seed wavelength was close to the edge of the fibre gain bandwidth.

Ref. [30] reported peak power scaling to 130 kW of another thulium doped fibre MOPA which had similar architecture as that in ref. [87] but a different signal wavelength at 1952 nm. Despite a better output OSNR of 40 dB in this work, the MOPA exhibited strong nonlinearities at the maximum output power. Its measured autocorrelation trace showed temporal beating atop the trace envelope, which the author attributed to the presence of MI at the highest output power of the MOPA.

However, it is known that sometimes intensity autocorrelation can be ambiguous. Two different pulse shape can yield a same autocorrelation and moreover, complicated and noisy pulses can generate an autocorrelation which has a coherence-spike-on-a-pedestal shape. Therefore, the results presented in ref. [30] were unreliable. The coherence spike on top of the autocorrelation trace can be an indication that the 1952-nm pulses were already broken into small pulses at a pulse energy of 4.8 µJ and a corresponding estimated peak power of ~126 kW. Hence, the performance of gain-switched diode-seeded thulium doped fibre MOPAs are still far from satisfactory and more efforts should be given to improve such systems.

Note that the setups I present in this chapter are similar to those in literatures([30, 87]) but the seed and each stage of the MOPA were completely rebuilt and characterised by myself. Section 3.2 illustrates picosecond pulse generation by gain-switching a 2-µm laser diode. A three-stage thulium doped fibre MOPA producing 76-kW peak power picosecond pulses is presented in section 3.3 with detailed characterisation of the in-band pumped preamplifiers. To satisfy the peak power requirement of mid-infrared SC generation, the three-stage thulium doped fibre MOPA was further optimised into a four-stage structure for higher peak power (up to 295 kW) along with excellent OSNR (~40 dB), which is discussed in section 3.4. To the best of our knowledge, this is the current highest peak power reported

from a picosecond-pulsed LMA-fibre-based TDFL. A brief summary of this chapter is given in section 3.5.

3.2 Gain-switched seed laser

3.2.1 Theory of gain-switching

Mode-lock techniques are commonly used to generate stable picosecond pulses. However, the major disadvantages of mode-locked lasers are the requirement of more components which adds to the system complexity, and a fixed pulse repetition rate determined by the cavity length. On the other hand, gain-switching a laser diode provides an easier route to picosecond pulse generation because of a much simplified structure and allowing adjustable repetition rate. Typical gain-switch operation of a laser diode is essentially to apply a bias direct current (DC) below the laser threshold, which is then superimposed with a train of short electrical pulses from a pulse generator. Figure 3.1 describes how optical pulses are produced from a gain-switched laser diode [88].

The electron density inside the diode maintains a very low level at the beginning and starts increasing only when the electrical pulse is injected into the active region of the diode. Lasing does not occur until the electron density has reached the lasing threshold. Accordingly, the photon density rises rapidly, forming the leading edge of the optical pulse in the time domain and leading to a depletion of electron density [88, 89]. Laser emission stops with a declining photon density when the electron density falls below the lasing threshold. However, the electron density could continue building up and reach the laser threshold again if the driving electrical pulse continues to pump the active region. A single optical pulse can be obtained if the electrical pump pulse terminates in time before reaching the lasing threshold for a second time. Otherwise, more spikes with decreasing amplitude could be generated [88, 89]. Hence the optical pulse is much shorter in duration than the driving pump pulse.
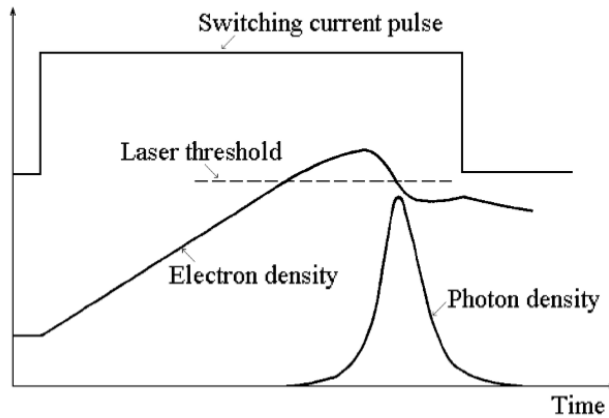
Figure 3.1. Physical process of gain-switching a laser diode [88].

The gain-switching method induces an inherent negative frequency chirp to the optical pulses, which can be inferred from the change in electron density in figure 3.1 [88]. When the injection current is switched on abruptly, the sudden increase in charge density leads to a temporary reduction of the refractive index of the laser active region. Consequently, the optical path length of the laser cavity is shortened, thereby shifting the lasing mode to shorter wavelength. Likewise, laser wavelength redshifts when switching off the injection current and reducing the charge density in the active region. Therefore, optical pulses generated by gain-switching a laser diode have an intrinsic frequency down-chirp [88].

3.2.2   Results and discussion

An InGaAs/InP discrete-mode laser diode at 1952 nm (Eblana Photonics, P/N: EP1948-DM-PM) was gain-switched to produce sub-hundred picosecond pulses and used as a seed of the thulium doped fibre MOPA. This laser diode had a ridge waveguide Fabry-Perot (FP) structure with etched slot features, which enabled discrete mode operation by strengthening one FP mode and suppressing the others [83]. The lasing threshold of the diode is 20 mA. The diode generates an average output power of ~1 mW at the maximum driving current of 100 mA.

46

Figure 3.2 shows an image of the gain-switched seed laser. A biased current of 16 mA was directly applied to the laser diode, using a Newport laser diode driver. A pulse generator (HP 8131A) delivered rectangular electrical pulses with a 420-ps duration and 5-V amplitude at variable repetition rates from 1 MHz to 500 MHz into the diode through the RF cable. The temperature of the laser diode was monitored and stabilised at 21 °C with a Thorlabs temperature controller (TC200).
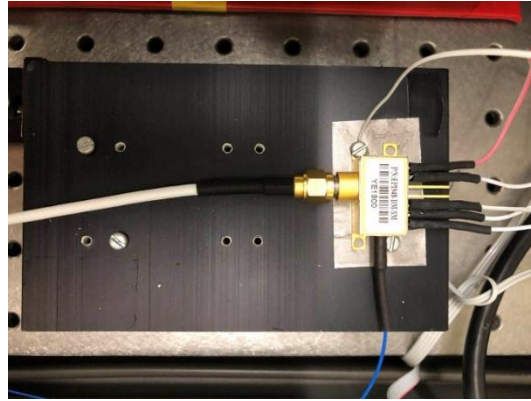
Figure 3.2. Photo of the gain-switched seed laser.

Figure 3.3(a) compares the output spectra of the seed diode operating in the CW mode and the gain-switching mode. In the CW regime, the seed diode emitted a single longitudinal mode at 1952.8 nm with a narrow 3-dB spectral bandwidth of less than 0.1 nm (blue line), an excellent side mode suppression ratio (SMSR) of up to 45 dB, and a mode spacing of ~1.5 nm.

The exact cavity length of this diode is unknown, but we try to estimate it from the free spectral range (FSR), compared with another Eblana laser diode, which is well illustrated in ref. [90]. In this literature, the 2008-nm discrete-mode laser diode was also fabricated in the InGaAs/InP multiple quantum-well system and had a similar FP cavity as compared to our 1952-nm diode. The 2008-nm diode is said to have a cavity length of 600 µm and a refractive index of 3.48 [90], so its FSR is calculated to be 71.8 GHz, corresponding to a longitudinal mode spacing of 0.97 nm. In our case, the measured mode spacing (~1.5 nm) corresponds to a free spectral range of 118.3 GHz. Thus, we obtain an estimated cavity length of ~365 µm for our 1952-nm diode. Given the discrepancy in fabrication between the two diodes, we think that the estimated cavity length (~365 µm) is reasonable in respect to that reported in ref. [90].
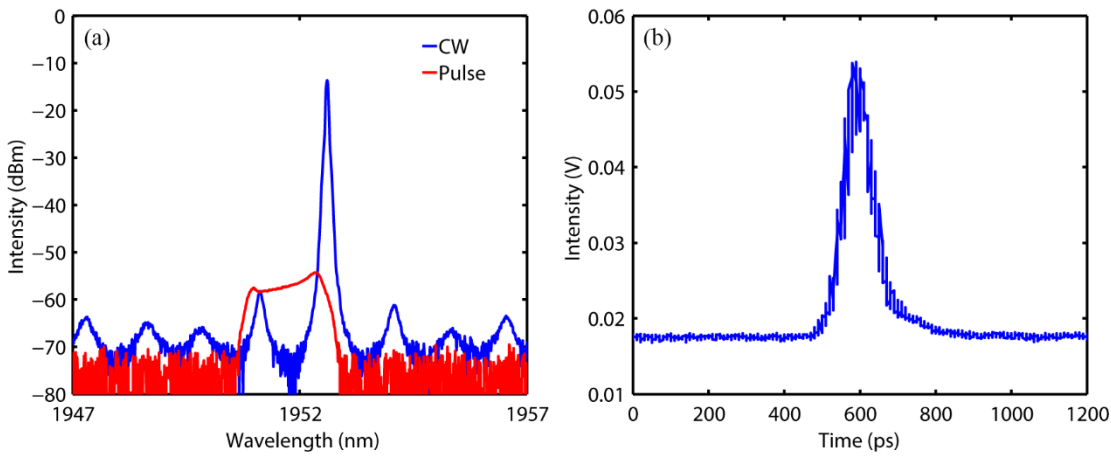
Figure 3.3. (a) Spectra of the seed diode at CW/gain-switching mode (0.05 nm resolution); (b) Temporal profile of the seed pulses at 1MHz repetition rate.

However, the output spectrum changed noticeably in gain-switching operation (e.g. at 1 MHz repetition rate). As depicted by the red line in figure 3.3(a), the two local peaks were at 1950.9 nm and 1952.3 nm respectively. The spacing of these two peaks (1.4 nm) was very close to the measured FSR (~1.5 nm), so it is believed that two longitudinal modes were emitted during the gain-switch operation of the diode. As a result, the 3-dB spectral bandwidth was broadened to 0.9 nm and the relative intensity ratio of these two adjacent modes degraded to ~3 dB, in comparison with the CW operation.

The temporal output of the gain-switched seed diode was characterised by a >9 GHz extended InGaAs photodetector (EOT, ET-5000F) and a 50-GHz Tektronix communication signal analyser (CSA), and shown in figure 3.3(b). Note that the intensity offset was caused by the dark current of the photodetector. The measured temporal trace had a Gaussian-shape profile with a full width half maximum (FWHM) of ~100 ps. It is to be noted here that the pulses might be shorter than 100 ps in time but cannot be resolved because of the bandwidth limit of the detector. Autocorrelation measurement was not feasible due to the low output power from the seed diode (µW level).

Sub-hundred picosecond pulses at repetition rate up to 500 MHz (limited by the pulse generator) could be generated in this case. The gain-switched laser diode driven at a higher repetition rate would have resulted in a higher average output power from the seed but the scope for peak-power scaling in the subsequent amplifier chain would be limited. Therefore, a moderate repetition rate of 1 MHz

was determined that offered the best compromise between average output power from the seed diode and power scaling in the thulium doped fibre MOPA system. The average output power of the 1-MHz gain-switched pulse train was ~1 μW.

3.3   Three-stage thulium doped fibre MOPA

3.3.1   In-band pumped preamplifiers

The low average power of the gain-switched seed pulses necessitated core-pumped preamplifiers to boost the signal power for the final amplification, prior to the development of a high power picosecond thulium doped fibre MOPA system.

3.3.1.1   Pump laser characterisation

An erbium/ytterbium co-doped fibre laser (EYFL) was built to in-band core-pump the preamplifiers at 1564 nm, where thulium doped fibres have decent absorption (e.g. ~30dB/m). Figure 3.4 shows the schematic of an FBG-stabilised EYFL. This pump laser had a 5-m-long double-clad Er/Yb co-doped fibre (Nufern) with a core/cladding diameter of 12/130 μm and core/first cladding NA of 0.2/0.46. The gain fibre was forward pumped by two 915-nm multimode laser diodes using a (2+1) × 1 pump and signal combiner. The HR grating had a very high reflectivity of over 99% at 1564 nm with a FWHM of 2 nm whereas the OC grating had a reflectivity as low as 6% at 1564 nm with a FWHM of 1.2 nm. The laser output power was coupled out through the SMF-28 fibre pigtail of the OC grating.
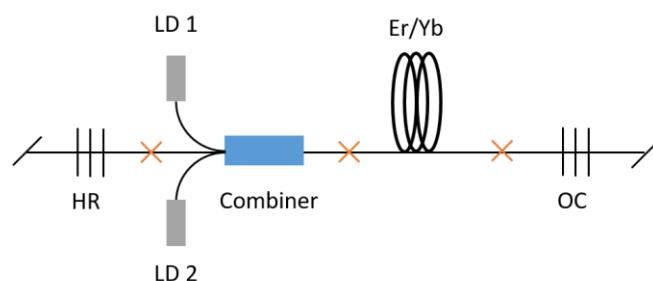
Figure 3.4. Schematic of the Er/Yb co-doped fibre laser.

Figure 3.5 plots the output power as a function of launched pump power and the spectrum of the laser output. A maximum output power of 2.9 W with a slope efficiency of 26% was achieved. This pump laser can provide adequate pump power for small-signal TDFAs. The spectrum shows a centre wavelength of 1564 nm with an OSNR of ~40 dB. An image of the pump laser is shown in figure 3.6.
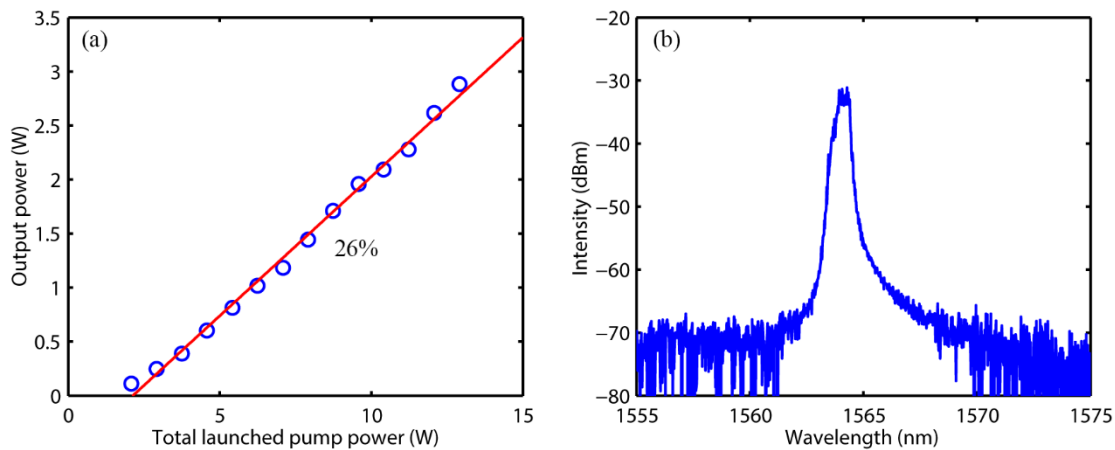
Figure 3.5. (a) Output power of the EYFL; (b) output spectrum of the EYFL (0.1 nm resolution).
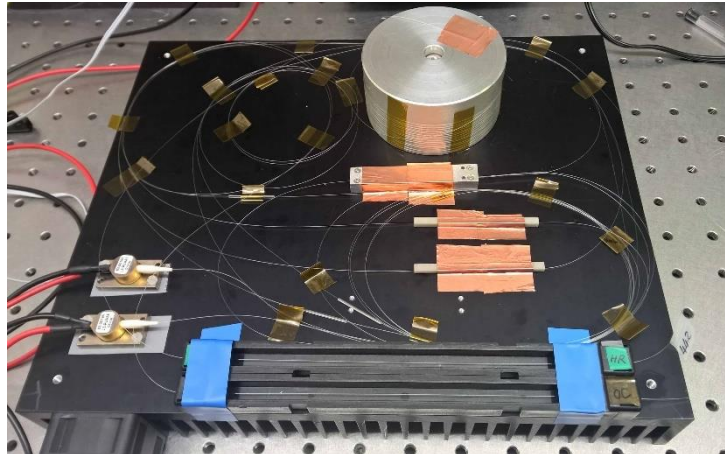
Figure 3.6. Image of the EYFL.

3.3.1.2   First-stage amplification

The average power of the seed laser was so low (~1 µW) that small-core thulium doped fibre was requested as the gain medium for the first-stage amplifier. A commercially available single-mode fibre from OFS (TmDF200) was used, with a 5-µm MFD at 1700 nm, a 125-µm cladding and NA of 0.26. This fibre had a peak absorption of 200 dB/m at 790 nm and a measured absorption of ~30 dB/m at

1564 nm. The quantum efficiency of pumping a thulium doped fibre at 1564 nm for signal amplification at 2 µm is about 80%. A free running laser efficiency test of this fibre was conducted in ref. [91]. The results of the test showed 75% and 71% slope efficiency for an 8-m and a 10-m length of TDF respectively, indicating a high efficiency of this OFS fibre. The results also suggested that 8 to 15 m long TDF "naturally" lases at ~1970–1990 nm as the lasing wavelength redshifts with an increasing fibre length due to signal reabsorption [91].

Since the target wavelength is 1952 nm, a fibre length of 8 m or less is a good starting point for the test. Figure 3.7 depicts two different structures that have been tested for the first small signal amplifier. In scheme 1, an 8-m-long TDF was forward pumped by the EYFL through a filter-based WDM (AFR). The pigtail of this WDM is SMF-28 fibre, which has a calculated MFD of 11.2 µm at a signal wavelength of 1.95 µm. The MFD of TmDF200 fibre at the same operation wavelength is estimated to be 6.1 µm. Irrespective of the mismatched MFDs, the splice loss between these two fibres can be reduced to less than 0.2 dB with an optimised splice recipe. Dual-stage isolators (AFR) were employed at both the input and output of the amplifier to prevent reflections and backward ASE from coupling back into the seed laser.
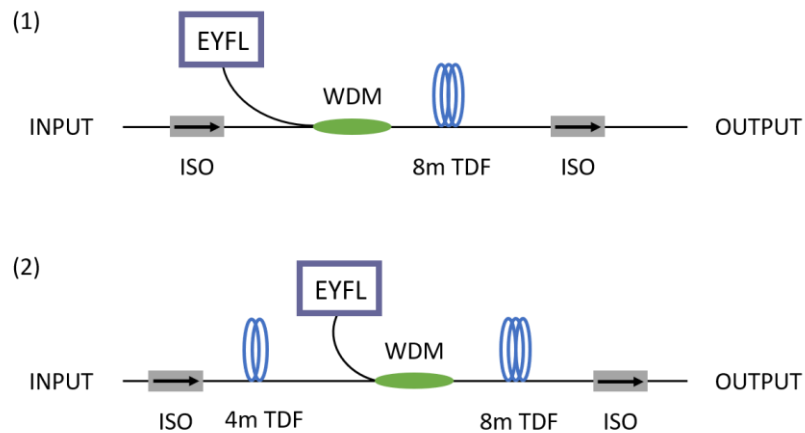
Figure 3.7. Schematics of the first preamplifier: (1) 8 m TDF scheme; (2) 4 m + 8 m TDF scheme.

This configuration obtained a total output power of 6.8 mW at a launched pump power of 0.6 W. However, a huge amount of ASE was created in between the pulses due to the short pulse duration (~100 ps) and comparatively long period (1 µs), leading to a poor in-band optical signal-to-noise ratio (OSNR) of ~11 dB, as shown in figure 3.8. The in-band signal power was calculated to be ~1.4 mW by integrating

the spectrum and excluding the noise. A further increase in pump power would not enhance the in-band signal power by much but would generate more ASE instead.
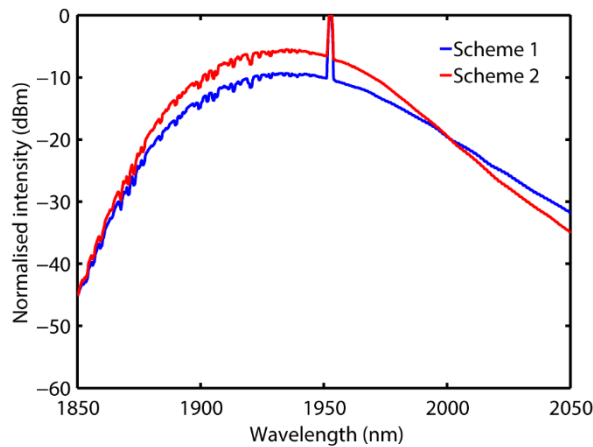
Figure 3.8. Spectra of the outputs of the first preamplifier in two configurations (1 nm resolution).

An electro-optic modulator (EOM) could be used after the first-stage amplifier to remove the excess ASE in between the pulses. However, the EOM was polarisation sensitive while all the components in the amplifier were polarisation insensitive except the PM-pigtailed seed diode, which had a linearly polarised output. As a result, the polarisation extinction ratio (PER) of the signal experienced degradation along the non-PM fibre inside the first preamplifier. Hence an in-line polarisation controller (PC) and a fast-axis-blocked polariser would have been needed before the EOM. The EOM itself had a loss of 6 dB and with the additional loss of the PC (~0.7 dB) and the polariser (~1 dB), the total loss would add up to ~9.7 dB for the signal. With the use of PC, the signal polarisation could be optimised so that the signal power had a minimum loss after the polariser. Nevertheless, the 9.7-dB total loss was still so large that a signal power of only 1.4 mW from the first preamplifier would not have been adequate for seeding the second-stage amplifier.

Consequently, the second structure in figure 3.7 was investigated whereby another 4-m-long TDF was inserted between the input isolator and the WDM, which helps improve the power conversion efficiency [92]. This additional fibre was indirectly pumped by the backward ASE generated from the forward-pumped 8-m-long TDF. In this case, the thulium doped fibre was more efficiently utilised by virtue of recycling the backward ASE, which produced a total output power of 36 mW at a pump power of 0.6 W. Increasing the pump power to ~0.95 W, which was just below the 1-W damage threshold of the WDM, a maximum total output power of 86 mW was achieved. Despite a worse in-band OSNR of ~6 dB in comparison with scheme 1 in figure 3.9, the second configuration generated an in-band signal power of ~11 mW out of a total output power of 86 mW. Therefore, scheme 2 was more favourable as the first preamplifier, because it provided a signal power of almost ten times higher than that of scheme 1, which could overcome the ~10-dB excess loss of the following EOM and the polarising components. The pulse profile of the first preamplifier (scheme 2) output is plotted in figure 3.9, which shows an unchanged pulse width of ~100 ps.
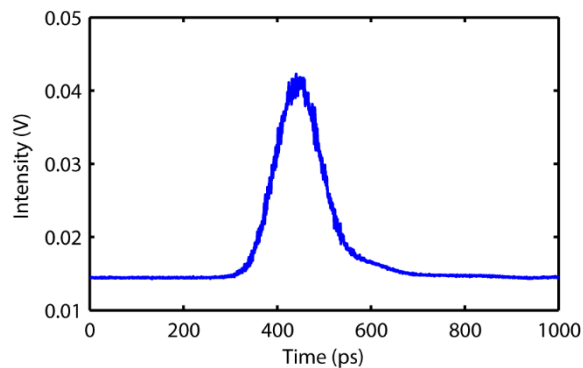
Figure 3.9. Output of the first preamplifier (scheme 2) in time domain.

Before developing the second-stage amplifier, the EOM (Photline, MPX2000-LN-01) was set up as a time gate to remove the excess ASE from the first preamplifier. The EOM was driven by a DC power supply providing a biased voltage of 8.7 V while a pulse generator synchronised to the seed diode delivered electrical pulses (7 V amplitude) to open and close the time gate. The minimum width of the time gate was 2.4 ns, limited by the settings of the pulse generator (HP 8110A). Hence the signal pulses passed the time gate with only a small fraction of ASE while the rest of the ASE was blocked by the time gate, thereby greatly improving the in-band OSNR from ~6 dB to ~25 dB as shown in figure 3.10. The signal power at the output of the EOM was 1.2 mW.
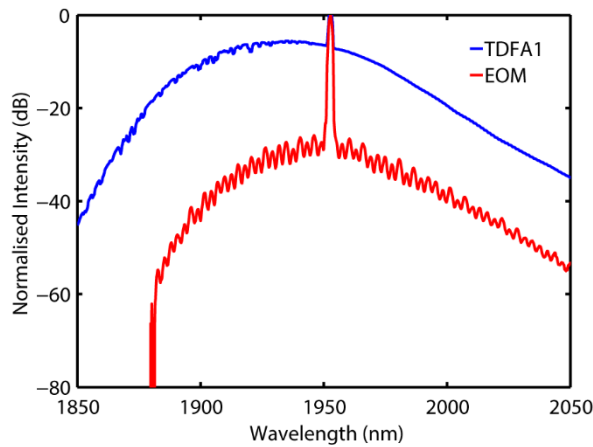
Figure 3.10. Spectra of signal output before and after the EOM (1 nm resolution).

Note that the EOM could also be operated as a pulse picker which could reduce the repetition rate of the signal pulses. Signal pulses running at a higher repetition rate (e.g. 10 MHz) had more average power from the seed, which helped extracting more output power from the first preamplifier with a better OSNR at the same time. However, when the EOM worked as a pulse picker to reduce the repetition rate to 1 MHz, the resulting output power turned out to be lower primarily due to the pump power limit sets by the WDM.

3.3.1.3   Second-stage amplification

The choice of thulium doped fibre becomes critical when it comes to the second preamplifier, as nonlinearities are expected to appear at higher signal power levels. In order to minimise the nonlinearities, it is preferable that the second preamplifier uses a short length of TDF with stronger pump absorption and a larger core.

Figure 3.11 illustrates the basic structure of the second-stage amplifier, which was also a core-pumped TDFA incorporating a short gain fibre and two isolators to prohibit back-reflections. Note that this preamplifier was pumped by another in-house built EYFL, which had a similar configuration as the pump laser described in section 3.3.1.1 but provided more output power of up to 5 W. Two different homemade fibres have been tested for the second preamplifier. Fibre TYPE-1 (part number: A0269_L10164) had a core/clad diameter of 8.5/100 μm and NA of 0.21. This fibre showed an extremely strong absorption of ~240 dB/m at 1560 nm but also a considerable absorption of ~10 dB/m at the signal wavelength. The fibre

54

length had to be very short due to the noticeable signal reabsorption of this particular fibre. The doped fibre was wrapped in small coils (5-cm diameter) to attenuate the high order mode so as to ensure single mode operation. The gain fibre was shortened to an optimum length of 0.4 m and produced an output power of 8.3 mW at 1-W pump power. It was observed that ESA was strong near the splice point where the pump was coupled into the doped fibre, turning the fibre "purplish". Excess heat was also generated during the amplification process because of the poor efficiency of this fibre. Thus, it can be concluded that fibre TYPE-1 was not ideal for the second-stage amplifier.
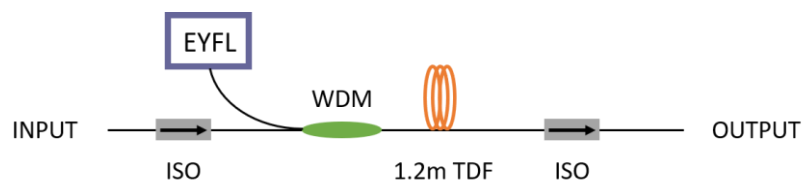
Figure 3.11. Schematic of the second preamplifier.

To improve the power performance of the second preamplifier, fibre TYPE-1 was replaced by fibre TYPE-2 (part number: B0155_L10146), which had less pump absorption (~95 dB/m at 1560 nm) and less signal reabsorption (~3 dB/m). This fibre also had an 8.5-μm core, a 100-μm cladding and 0.2 NA. Forward pumping a 1.2-m length of fibre TYPE-2, the second-stage amplifier amplified the 1-MHz signal pulses from 1.2 mW to 48 mW at 1-W pump power before the onset of MI. As indicated by figure 3.12(a), this amplifier had low noise and the signal maintained a good in-band OSNR of ~21 dB.
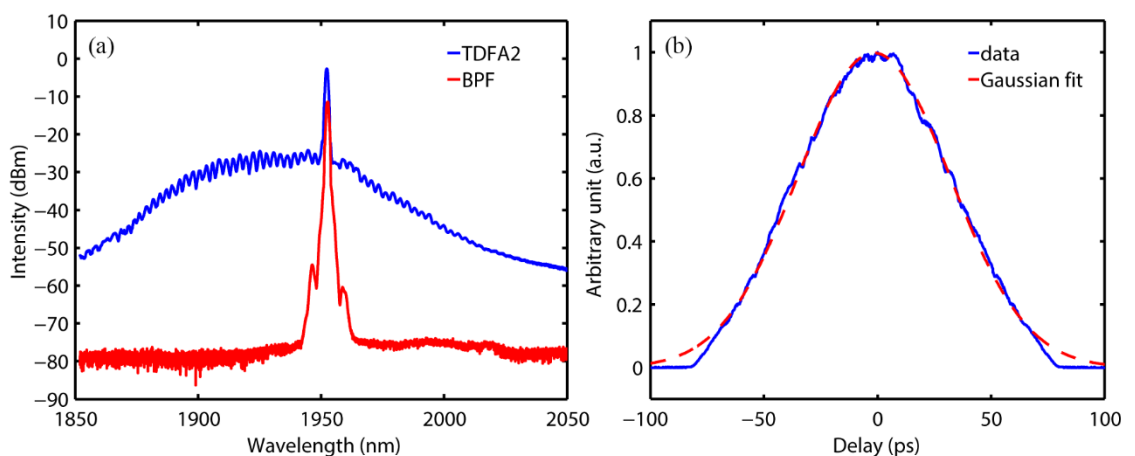
Figure 3.12. (a) Spectra at the outputs of the second preamplifier and after the band pass filter (1 nm resolution); (b) Temporal profile of the output of the second preamplifier.

An autocorrelator (APE pulsecheck) instead of a photodetector was used to measure the pulse width at the output of the second preamplifier, for now the amplified signal should have enough peak power for SHG in the crystal of the autocorrelator. The FWHM of the measured Gaussian-shape autocorrelation (AC) trace was 74 ps as shown in figure 3.12 (b). This corresponded to a Gaussian pulse width of 52 ps. The peak power of the pulses was calculated to be ~0.92 kW.

A pigtailed etalon-based tuneable filter (Agiltron, FOTF-020121131) was placed after the second-stage amplifier to improve the out-of-band signal OSNR ready for coupling into the final power amplifier. This band pass filter had a -3 dB bandwidth of 3.6 nm, a -20 dB bandwidth of 10 nm and a tuneable wavelength range from 1860 nm to 2030 nm. It can be seen from figure 3.12(a) that this filter cleaned up most ASE and enabled an out-of-band OSNR of at least 60 dB with two sidelobes peaking at 1946 nm and 1959 nm. These two sidelobes originated from the filter spectral response, which can be confirmed by figure 3.13. An ASE source generated from a TDFA was used to measure the transmission response of the filter. The two sidelobes situating at 1946 nm and 1959 nm were ~20 dB below the main peak at 1953 nm. The insertion loss of this filter was ~3.3 dB at the signal wavelength, resulting in a reduced signal power of 22 mW at the output of the filter. A photo of the first and second preamplifiers as well as the EOM is shown in figure 3.14.
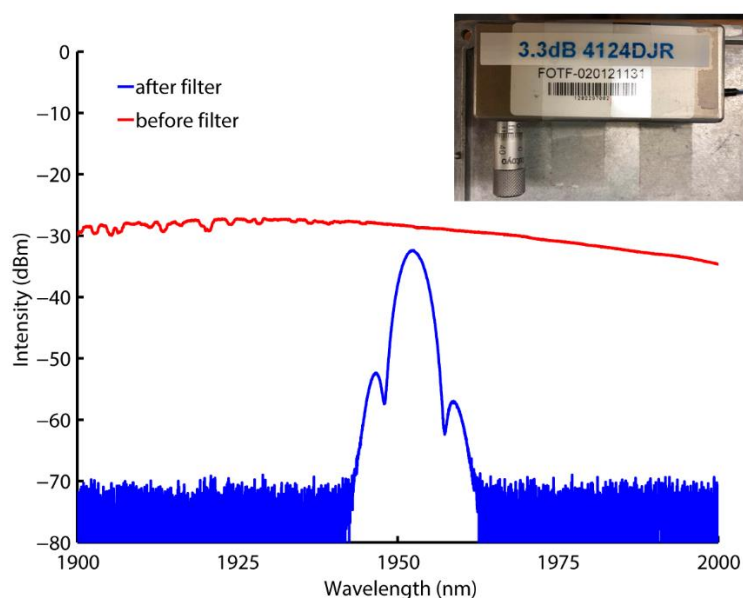
Figure 3.13. Spectral response of the band pass filter with 1 nm resolution. The inset shows the photo of the filter in use.
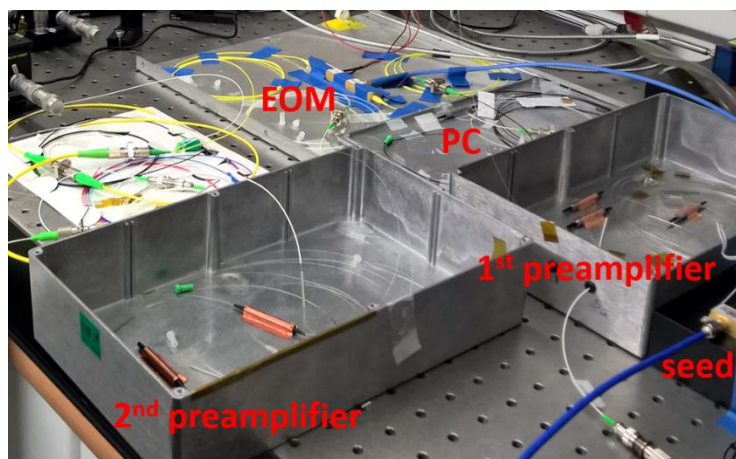
Figure 3.14. Setup photo of the in-band pumped preamplifiers.

3.3.2   Third-stage power amplifier

Figure 3.15 provides the schematic of the complete three-stage MOPA system and the structure of the third-stage amplifier. Detailed characterisation of the gain-switched seed laser and two preamplifiers have been provided in previous sections, but a brief summary is given here for reference only. 1-MHz picosecond pulses with 1-µW output power and ~100-ps pulse duration was generated by gain-switching a seed diode at 1952 nm. The signal power was enhanced to 11 mW by the first preamplifier but was impaired by the excess ASE in between the pulses which was removed by using a lossy EOM. The output of the EOM had a power of 1.2 mW with an OSNR of ~25 dB. The second preamplifier increased the signal power to 48 mW and the following band pass filter eliminated the out-of-band ASE, leading to an output power of 22 mW with a 60-dB out-of-band OSNR.

To scale up the energy and peak power of the picosecond pulses, a third-stage amplifier based on an LMA thulium doped fibre was proposed in figure 3.15(b). The input signal and the pump were arranged in a counter-propagating configuration in this final-stage amplification. The input of this power amplifier had a standard APC pigtailed SMF-28 fibre taper-spliced to an LMA double-clad thulium doped fibre, which facilitated the detachable connection between the second and the third amplifiers. This 2-m-long LMA fibre had a 25-µm core diameter with 0.09 NA, a 250-µm cladding diameter with 0.46 NA and a cladding absorption of ~9.5 dB/m at 793 nm. The output end of the active fibre was terminated with an angle-polished end cap. This helped in avoiding any back-reflections and optical damage to the fibre end facet due to high signal intensity.
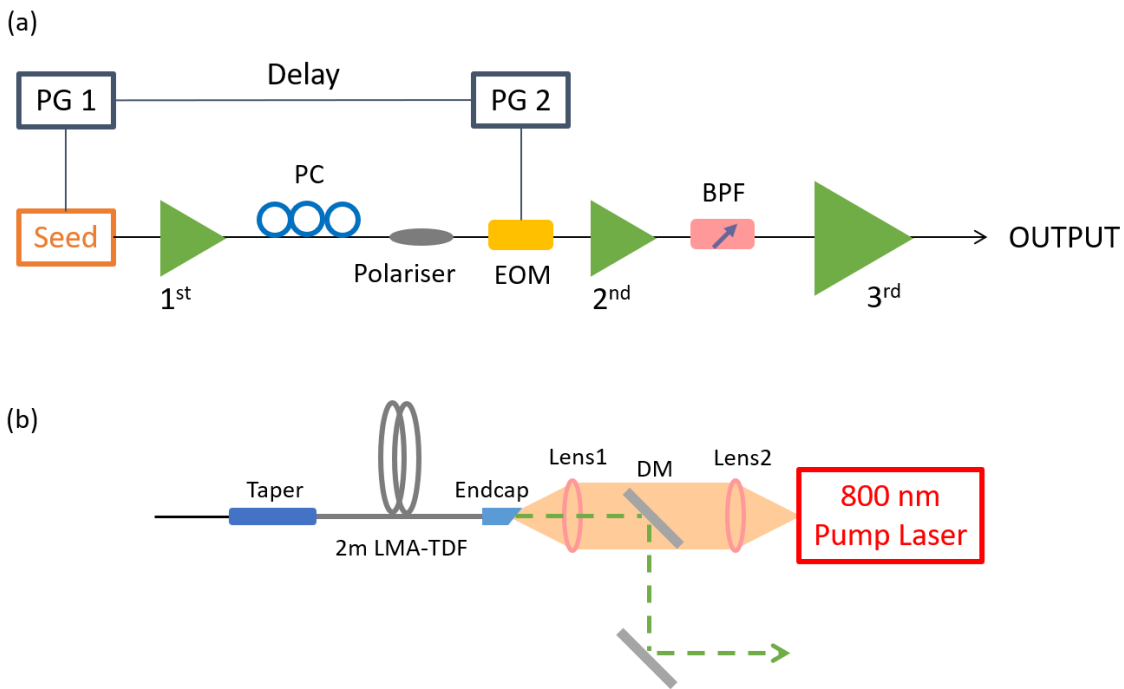
Figure 3.15. Schematics of (a) the three-stage thulium-doped fibre MOPA system and (b) the final-stage amplifier (PC: polarisation controller; PG: pulse generator; BPF: band pass filter; DM: dichroic mirror).

The fibre-coupled pump diode (P/N: JOLD-75-CPXF-2P iTEC), mounted on a water-cooled aluminium base and monitored by a thermoelectric cooler (TEC), can provide a pump power of up to 50 W. The output fibre has a core diameter of 400 μm and core NA of 0.22. Spectral and power characteristics of the pump diode are plotted in figure 3.16. The pump laser emitted at 797 nm with a FWHM of 1.8 nm. A pair of lenses were used to collimate and focus the pump laser beam into the doped fibre. Focal lengths of Lens1 and Lens2 were 12 mm and 25 mm respectively. An 800 nm/2000 nm dichroic mirror (DM) was placed in between the lenses to separate the output signal beam and the residual pump laser beam.
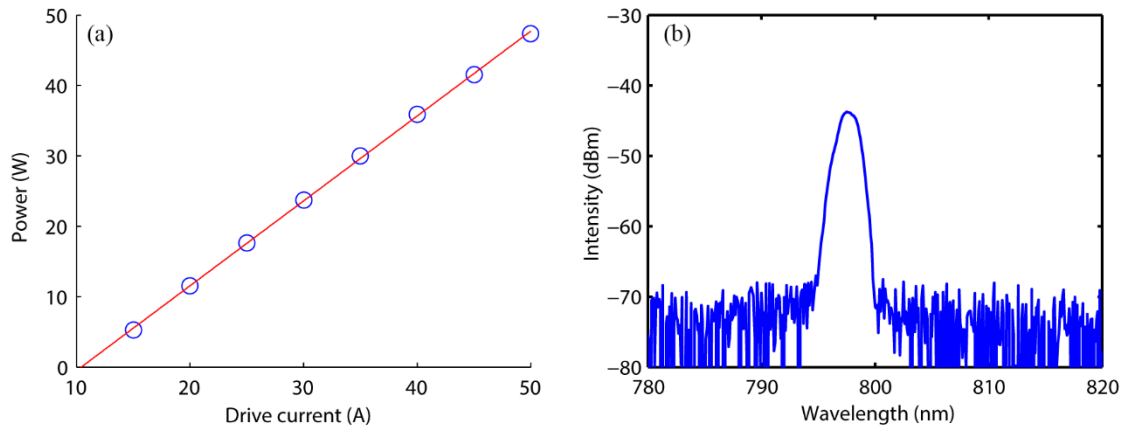
Figure 3.16. (a) Power and (b) spectral characteristics of the pump diode (1 nm resolution).

Figure 3.17 shows the photo of the final-stage amplifier. The coil of the thulium doped fibre was mounted on another powerful TEC which could bring the temperature down to 5 °C. The output fibre end was firmly mounted on a water-cooled translation stage. A chiller which had a lower temperature limit of 10 °C was used to take away heat from the translation stage. However, a small section of the doped fibre had to be suspended in air due to the difference in height between the stage and the TEC. A thin slice of copper tape was closely clung to the suspended fibre to help in dissipating the generated heat. In this experiment, the TEC and the chiller were operating at 15 °C, since dew was noticed on all the metallic surfaces when operating at lower temperatures (e.g. 10 °C).
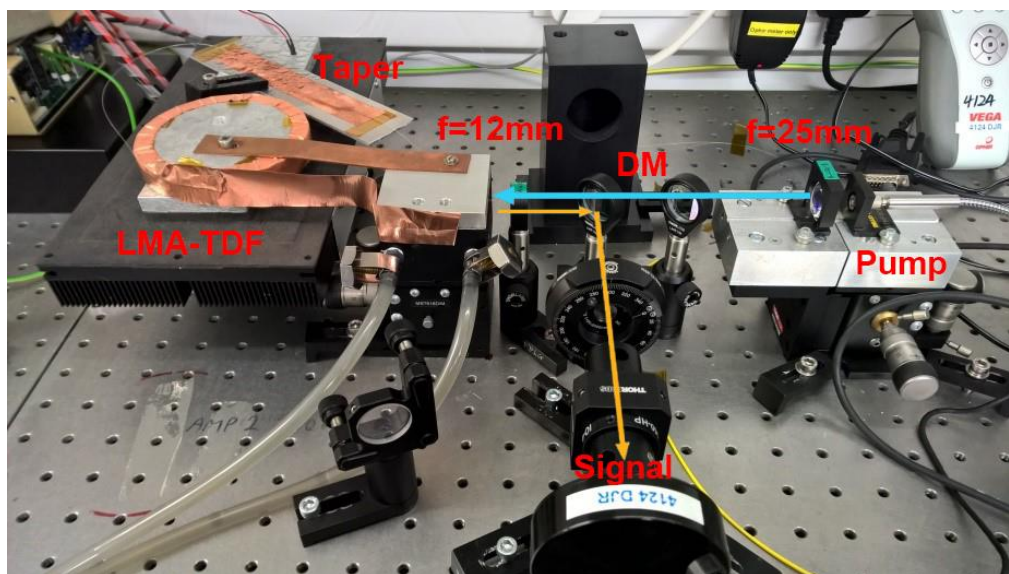
Figure 3.17. Photo of the final-stage amplifier.

Figure 3.18 plots the power and temporal characteristics of the MOPA output. In the third-stage amplifier, the output power was scaled up to 3.94 W at a slope efficiency of 17.4%. Note that the output power reported here was the in-band (1950.5-1952.8 nm) signal power calculated from the measured spectrum and the measured total output power. Figure 3.18(b) shows the autocorrelation trace having a FWHM of 74 ps, which indicates a Gaussian pulse width of 52 ps. We observed no change in pulse duration with output powers of the third-stage amplifier.
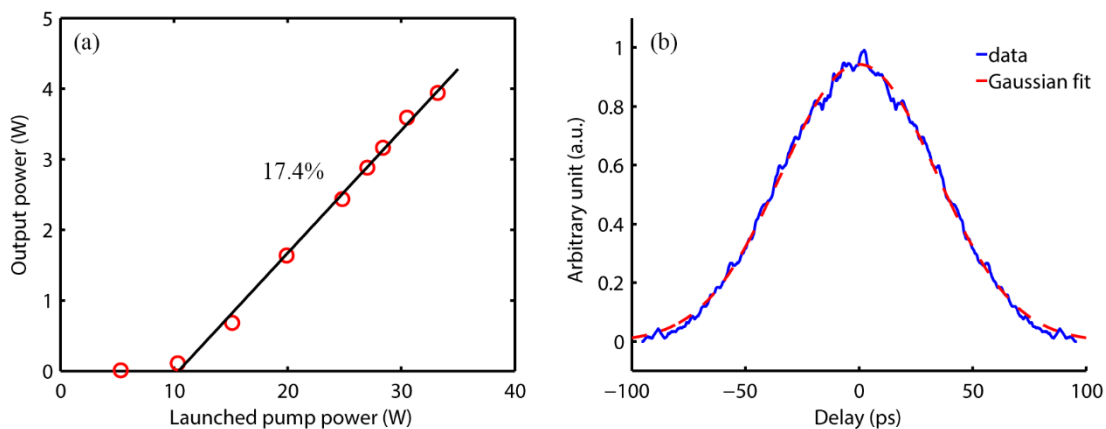
Figure 3.18. (a) Power and efficiency of the third-stage amplifier; (b) Autocorrelation trace of the MOPA output.

As illustrated by the broadband spectra in figure 3.19(a), the input signal was amplified with increased pump power while the ASE also built up very quickly. Because of the SPM and FWM, the -20 dB bandwidth of the output spectrum broadened from 2.7 nm at the input of the third-stage amplifier to 3.4 nm at the maximum output power of 3.94 W. MI started to appear when the signal power reached 3.94 W, which can be seen from the small hump near 1980 nm of the green line plot. The symmetric MI sidebands peaked around 1920/1980 nm but the one at ~1920 nm was masked by the ASE. Figure 3.19(b) plots a high-resolution spectrum at 3-W output power, which better illustrates the nonlinearities-induced spectral change experienced by the amplified pulses. It can be clearly seen that more frequency components were generated as small peaks around the input signal, highlighted by the red circles in the figure. This was due to the fact that FWM led to an energy transfer from the signal pulses to the out-of-band noises at high peak powers. The additional frequency components resulted from SPM and FWM can be further amplified if they fall within the gain bandwidth of MI. Consequently, nonlinearities including SPM, FWM and MI inhibited scaling the

output power of the MOPA to beyond 4 W. Besides, the in-band OSNR of the MOPA output was degraded to ~15 dB by the combined effects of nonlinearities and the ASE. The beam quality of the MOPA output was measured by an Ophir Nanoscan at the maximum output power. As shown in figure 3.20, the output of the MOPA had a beam quality of M^2~1.5 and M^2~1.6 at the x and y axis respectively.
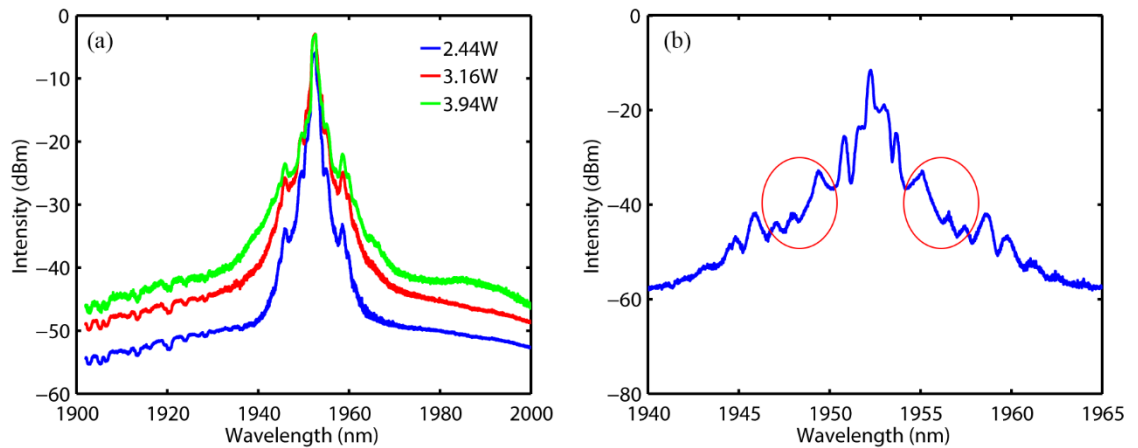
Figure 3.19. (a) Broadband spectra of the MOPA output (1 nm resolution); (b) high resolution spectrum of the MOPA output at 3 W (0.1 nm resolution).
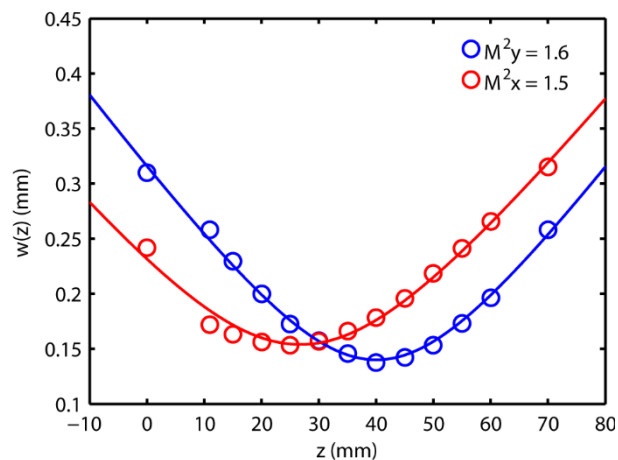
Figure 3.20. Beam quality of the MOPA output.

To conclude section 3.3, a three-stage thulium doped fibre MOPA system seeded by a gain-switched laser diode was demonstrated producing 52-ps pulses with an average output power of 3.94 W, a peak power of 76 kW and a good beam quality of 1.6. This MOPA system was used to pump a ZBLAN fibre for supercontinuum generation up to ~4 μm, which will be discussed in detail in section 4.2.

3.4 Four-stage thulium doped fibre MOPA

Picosecond pulses with a peak power of up to 76 kW have been achieved from a simple fiberised structure comprising only a gain-switched seed diode and three amplification stages. This three-stage thulium doped fibre MOPA system is very useful for applications where moderate peak powers are required, such as sensing and tissue ablation [33, 35]. It is also advantageous in terms of compactness and cost. However, strong nonlinear effects that occurred at a relatively low power level and accumulated rapidly in the third-stage amplifier, hindered the signal amplification with much degraded OSNR. It merits special attention that the gain-switched seed laser with only two longitudinal modes can act as a seed for nonlinearities such as FWM and MI, significantly lowering the nonlinear threshold. Careful management of fibre nonlinearity and the signal purity have to be taken into considerations to overcome the limitations exerting on the MOPA performance. Hence a new configuration of the high-power picosecond thulium doped fibre MOPA is proposed for nonlinear mitigation in the MOPA chain and addressing applications that demand higher peak power.

Figure 3.21 depicts the schematic of the four-stage thulium doped fibre MOPA system. The seed, the first and the second preamplifier were maintained in the four-stage MOPA. After the second preamplifier, an FBG-based filter was used to substitute the band pass filter, which removed the ASE and the sidebands from the seed at the same time. A new third-stage preamplifier was added to the amplifier chain to compensate the high insertion loss of the FBG-based filter. The final-stage amplifier employed the same type of LMA thulium doped fibre but was adapted to make it more efficient as well as to manage the nonlinear effects. New mechanics were also designed to optimise the fibre cooling in the four-stage thulium doped fibre MOPA system. All the optimisations mentioned above enabled us to accomplish peak power scaling to ~300 kW. The following subsections discuss how these optimisations improved the performance of the gain-switched diode-seeded thulium doped fibre MOPA system.
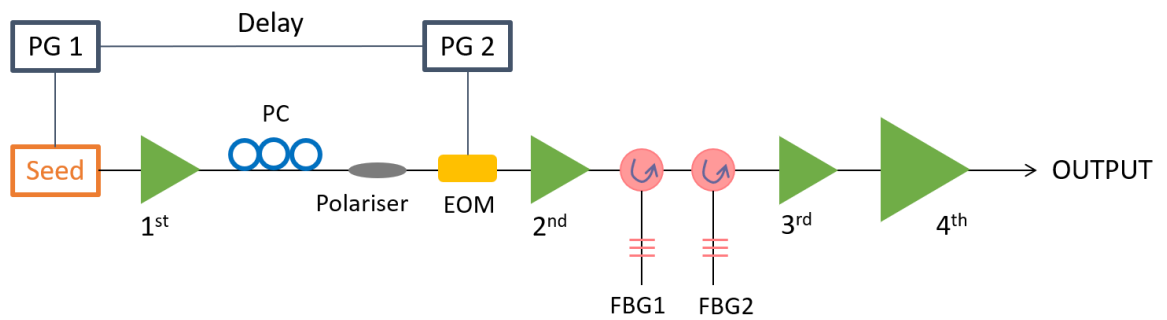
Figure 3.21. Schematic of the four-stage thulium-doped fibre MOPA system (PC: polarisation controller; PG: pulse generator).

3.4.1 FBG-based filter

As shown in figure 3.21, the FBG-based filter was composed of a pair of circulators and customised FBGs. Before utilising the grating filter, the FBGs were tested with a 2-μm ASE source and a circulator to measure their transmission and reflection characteristics. Figure 3.22 sketches the setup and figure 3.23 illustrates the features of the FBGs. Both gratings had a centre wavelength of 1952.2 nm and a high reflectivity of more than 99%. The bandwidths of the first and the second gratings were 0.8 nm and 0.5 nm respectively. Small reflection peaks in the short wavelength region were due to the cladding modes. The two gratings, each of which was spliced to a circulator, were connected in series to form a narrow passband filter.
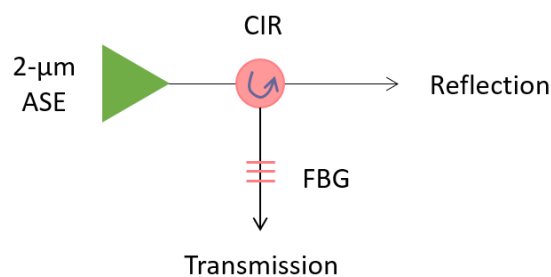
Figure 3.22. Setup sketch of the FBG test (CIR: circulator).
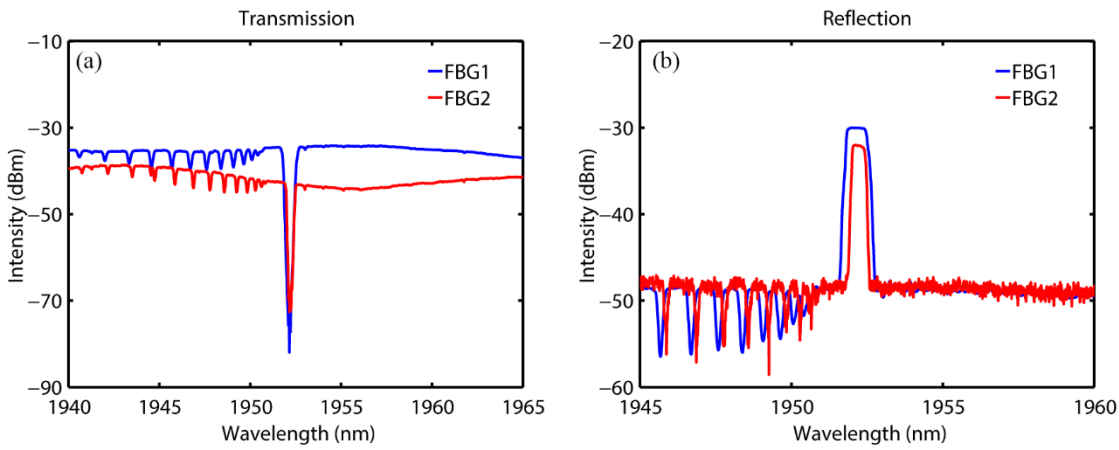
Figure 3.23. Transmission and reflection characteristics of FBGs (0.05 nm resolution).

Spectra at the outputs of the seed and preamplifiers are replotted in figure 3.24(a) to compare the spectral outputs before and after the FBG-based filter. The spectra were measured with 0.05 nm resolution bandwidth of the OSA so as to distinguish the fine structures. In contrast to the single longitudinal mode operation in the CW regime (blue line), gain-switching the seed diode (red line) resulted in the emission of two longitudinal modes which had comparable spectral intensities. The two longitudinal modes centred at 1950.9 nm and 1952.3 nm respectively. Note that the spectrum at the output of the EOM exhibited multi-peak structure owing to the spectral response of the EOM rather than strong nonlinear effects. It can be seen by comparing the cyan line in figure 3.24(a) and the blue line in figure 3.24(b) that the signal was amplified to 48 mW in the second-stage amplifier without significant nonlinear distortion but the intensities of the sidebands (e.g. at 1950.1 nm and 1953 nm) grew very quickly.

The band pass filter used in the three-stage thulium doped fibre MOPA system could not eliminate these sidebands effectively because of its bandwidth limitations. However, these undesirable sidebands and the dual longitudinal modes from the gain-switched diode were potential seeds for FWM and MI, which would deteriorate the signal spectrum in the following amplification stages as evidenced in figure 3.19(b). In order to minimise the signal impairment due to nonlinearities in the cascaded amplification stages, only the strongest longitudinal mode (at 1952.3 nm) was picked out by means of the narrow-band gratings to seed the follow-on amplifiers. As illustrated in figure 3.24(b), the first grating effectively removed the majority of the unwanted spectral components and obtained a greatly improved SMSR of ~40 dB, which was later enhanced to 55 dB by the second grating.

Meanwhile, output power was largely reduced as a result of the insertion losses of the circulators and the slicing of the signal spectrum with the grating filter. The power at the output of the first and second grating were 13 mW and 5 mW respectively. Note that the typical loss of the 2-µm circulators from AFR is about 2 dB and that the total loss of this FBG-based filter reached ~9.8 dB.
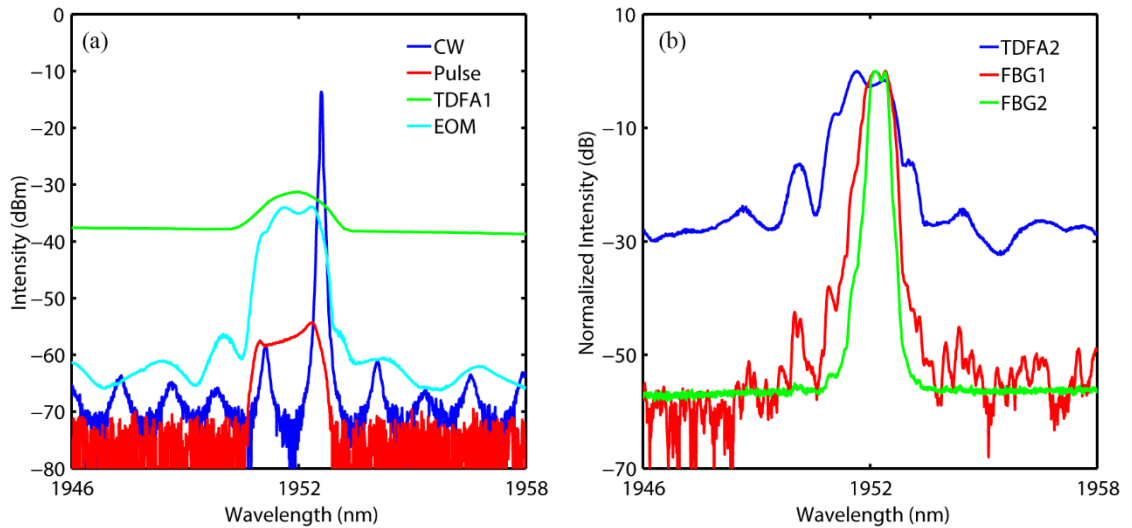
Figure 3.24. (a) Spectra of the seed diode in CW and pulsed operations as well as the outputs of the TDFA1 and EOM (0.05 nm resolution); (b) Spectra at the outputs of TDFA2, FBG1 and FBG2 (0.05 nm resolution).

Figure 3.25 depicts the autocorrelation traces measured at the outputs of the first and second grating filters. After the first grating, the autocorrelation trace had a FWHM of 37 ps, which corresponded to a Gaussian pulse width of 26 ps. However, the second grating stretched the pulse width to ~35 ps, which could be inferred from a broader autocorrelation trace with a FWHM of ~49 ps. Note that the autocorrelation trace measured after the second grating was much noisier due to a lower signal power of 5 mW.
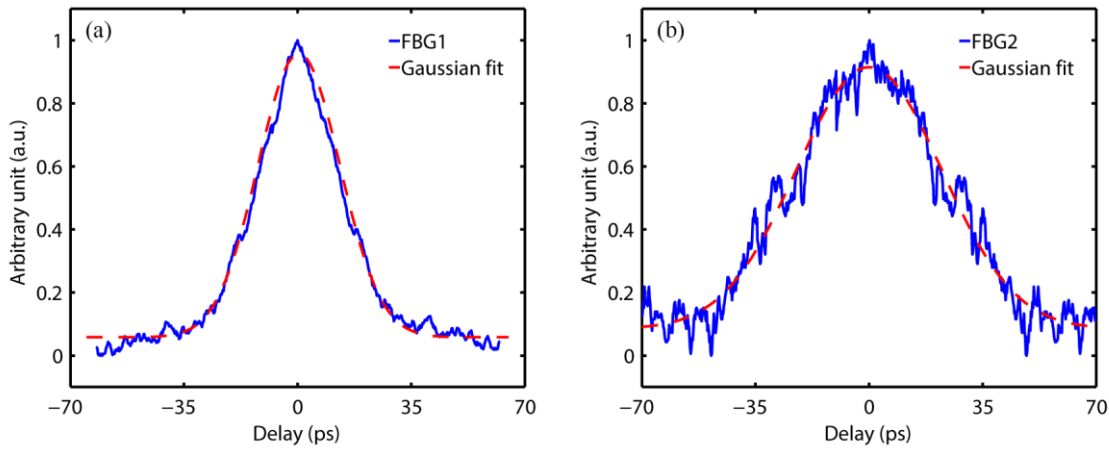
Figure 3.25. Autocorrelation traces measured at the outputs of (a) FBG1 and (b) FBG2.

3.4.2　Third-stage preamplifier

Remarkable signal purity with SMSR of 55 dB was achieved by the grating-based filter but at the price of high transmission loss of the signal. Therefore, a third preamplifier stage was incorporated to compensate the loss introduced by the grating filter and boost the signal power into the final stage amplifier. Figure 3.26 presents the schematic of the third-stage amplifier. Both the first and second preamplifiers were core-pumped amplifiers, but the third preamplifier was designed as a cladding-pumped configuration based on an in-house fabricated fibre with a larger core to further enhance the nonlinear threshold. The gain fibre in this preamplifier was a double-clad thulium doped fibre having a core/clad diameter of 11/127 μm and a cladding absorption of ~6 dB/m at 790 nm. This fibre was cladding pumped by a multimode laser diode at 790 nm which could provide a maximum pump power of 9 W. The active fibre length was chosen as 2.5 m long to ensure adequate pump absorption of ~15 dB. A small amount of residual pump power was stripped off by the high-index-coated splice to the output isolator. Isolators were put at both the input and output of the amplifier to prevent parasitic lasing. Note that the fibre pigtail of the output isolator was shortened to an optimum length to avoid nonlinearities. A photo of the third-stage amplifier is shown in figure 3.27. The pump diode and the fibre were cooled by a TEC constantly running at 15 °C.

66
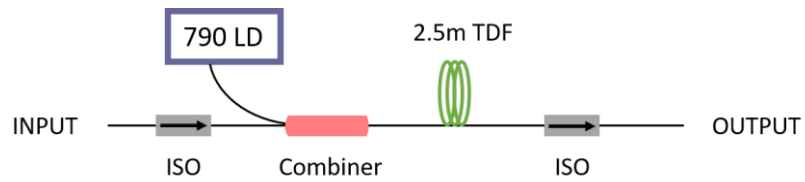
Figure 3.26. Schematic of the third-stage preamplifier.

Figure 3.27. Photo of the third-stage amplifier.

As illustrated in figure 3.28, the third-stage amplifier could scale the output power to ~0.3 W at a slope efficiency of 22.3% before the onset of MI with the two noticeable sidebands at ~1935 nm and ~1970 nm. As expected, the peak of the MI sidebands shifted outward from the central signal peak with growing output power. Frequency components caused by FWM manifested as a bunch of small peaks superimposed on the MI sidebands along with a broadband ASE as indicated by the green line in figure 3.28(b). Although a higher input power to the final (fourth) stage amplifier was preferred, taking nonlinearity management into consideration, it was concluded to operate the third preamplifier at an output power of less than 0.274 W to seed the final-stage amplifier. The temporal profile of the third-stage amplifier was measured by an autocorrelator, as shown in figure 3.29 with a FWHM of 49 ps. The corresponding Gaussian pulse width was 35 ps, which remains same at all output powers.

Briefly, a cladding-pumped third-stage amplifier was demonstrated to generate a nonlinearity-free maximum output power of 0.274 W with an in-band OSNR of 50 dB. This power level and signal purity were crucial to energy scaling of picosecond pulses in the final-stage amplifier.
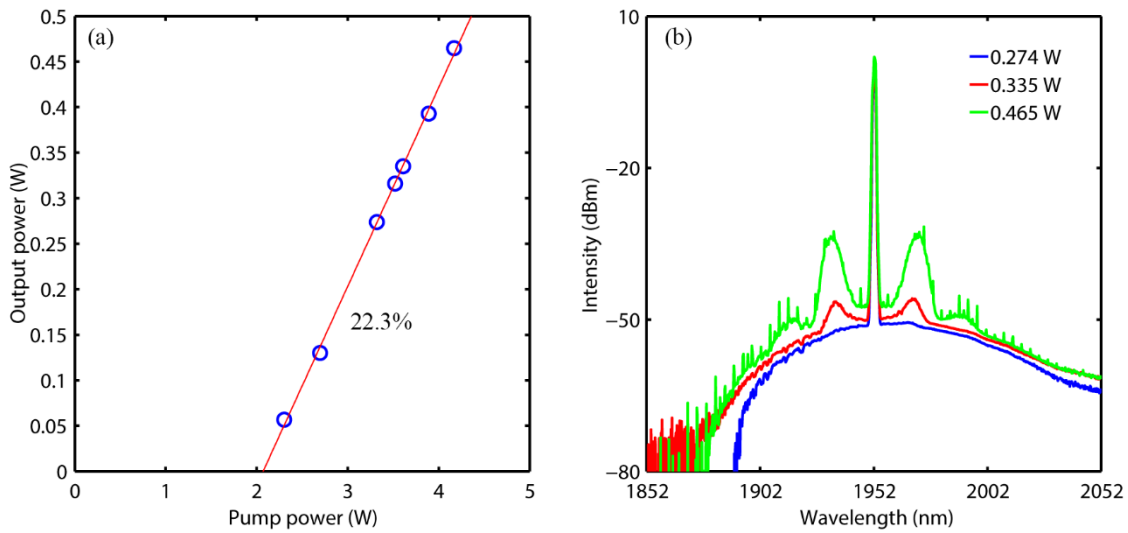
Figure 3.28. (a) Power and (b)spectral characteristics of the third preamplifier.
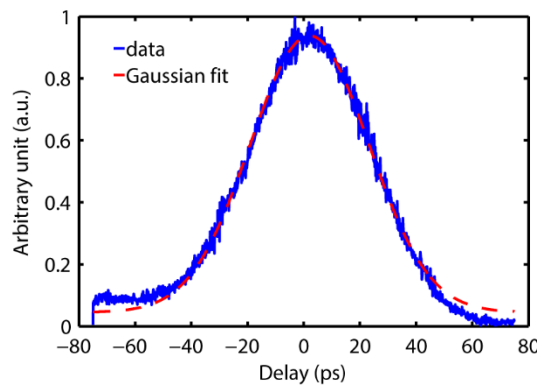
Figure 3.29. Autocorrelation trace of the output of the third preamplifier (57 mW).

68

3.4.3   Fourth-stage power amplifier

In addition to the new FBG-based filter and third-stage preamplifier, the final-stage amplifier of the MOPA system was also modified for better optical performances, including a shortened gain fibre length, a new pump laser and a homemade mode adaptor (MA) at the amplifier input. Figure 3.30 illustrates the new schematic of the final-stage amplifier of the four-stage thulium doped fibre MOPA system.
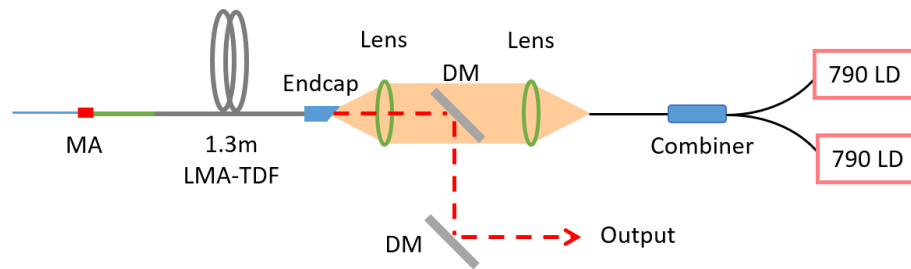
Figure 3.30. Schematic of the final-stage amplifier of the four-stage thulium doped fibre MOPA system (MA: mode adaptor; DM: dichroic mirror).

Signal from the third-stage amplifier was launched into the final-stage amplifier through the mode adaptor, which was made of a 0.3-mm-long graded-index fibre with a core/cladding diameter of 50/125 µm. The mode adaptor was designed and made by Dr. Yongmin Jung. The input pigtail of the mode adaptor was a 20-cm-long SMF-28 fibre whereas a 15-cm-long passive double-clad fibre was spliced to the graded-index fibre as the output of the mode adaptor. The passive double-clad fibre had the same parameters as the gain fibre (25/250 µm core/clad diameter, 0.09 NA). Acting like an imaging lens, this mode adaptor helped in matching the fundamental mode of the two dissimilar fibres and reducing the coupling loss to just 1dB.

In the four-stage thulium doped fibre MOPA system, the gain fibre of the final stage amplifier was reduced from 2 m to 1.3 m so as to decrease the nonlinear interaction length and increase the nonlinear threshold. The final-stage amplifier was free-space counter-pumped by two 790-nm multimode pump laser diodes, which were combined by a (2+1) ×1 pump and signal combiner. The pump beam was collimated by a B-coated aspheric lens (f = 8 mm) and then coupled into the doped fibre with an uncoated plano-convex lens (f = 12 mm). Two 800/2000 nm dichroic mirrors were used to extract the output signal beam from the fibre and remove the background pump light.

The combined pump diodes could deliver a maximum pump power of up to 50 W as shown in figure 3.31. The pump diodes were water-cooled to stabilise the emission wavelength at ~790 nm, where the absorption peak of thulium doped fibres lies. The pump diodes had a 3-dB spectral bandwidth of 2 nm. Irrespective of a short gain fibre length of 1.3 m, more than 92% of the launched pump power could be absorbed. Residual pump power was stripped off by high-index gel at the splice point between the doped fibre and the passive fibre pigtail of the mode adaptor. The doped fibre output had an angle-polished core-less end cap, which reduced the optical intensity at the glass-air interface and prevented optical damage to the fibre end facet.
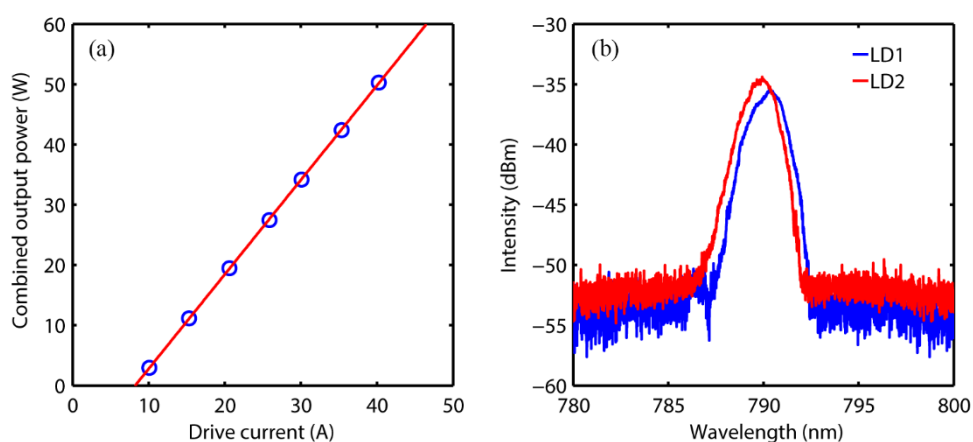
Figure 3.31. (a) Power and (b) spectral characteristics of the pump diodes at 790 nm.

Figure 3.32 and figure 3.33 provide an image of the fourth-stage amplifier and a close shot of the mechanics designed to improve the fibre-cooling efficiency. In the three-stage thulium doped fibre MOPA system, a small section of the LMA thulium doped fibre, inside which pump absorption was very strong, could not be mounted on any heat sink, resulting in heavy thermal load. The coating of this fibre section would gradually degenerate after continuous operation for many hours, which could lead to a worse pump confinement in the fibre cladding and hence a lower efficiency of the amplifier.

In order to protect this section of gain fibre and enhance the efficiency, new fibre mounts were designed and fabricated in house. The output fibre section was sandwiched in the V-groove between the two aluminium plates, which were constantly cooled by the circulating cold water at 15 °C. The bottom aluminium plate had a specially-designed cut with a radius of 7.5 cm so that the rest of the

doped fibre could be mounted on the adjoining water-cooled metallic mandrel without any gaps. The fibre surface was covered by thin graphite with excellent thermal conductance.
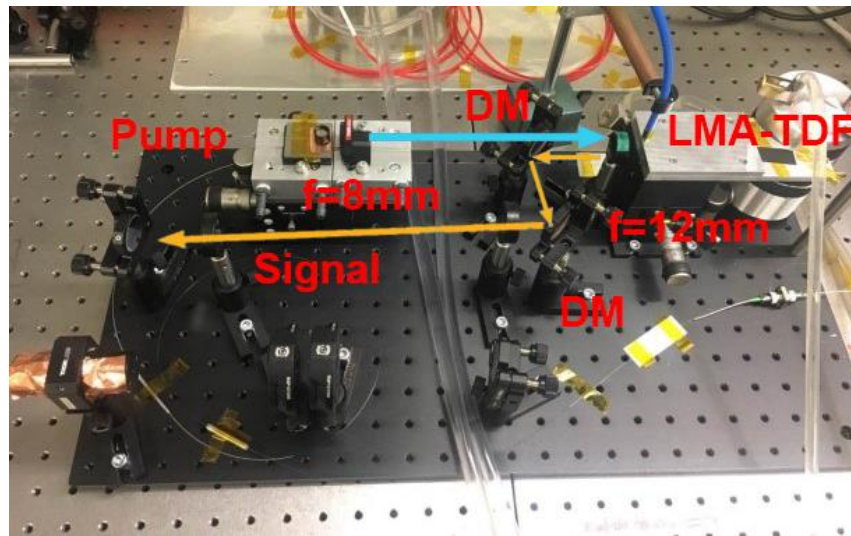
Figure 3.32. Image of the final-stage amplifier in the four-stage thulium doped fibre MOPA.
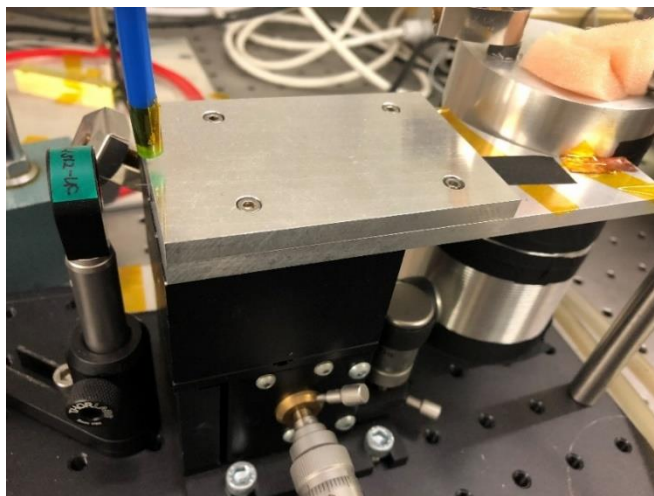
Figure 3.33. Close shot of the designed fibre-cooling system.

A moderate output power of 130 mW from the third-stage amplifier was chosen to seed the final-stage amplifier to enhance signal gain and to mitigate nonlinear effects even further. Results are plotted in figure 3.34. The average output power of the final-stage amplifier was successfully scaled up to 9.08 W at a pump power of 40.8 W, with a slope efficiency of 27.8%. However, it can be seen from the spectra that strong nonlinear effects arose in the amplifier with multiple sidebands at the

maximum output power of 9.08 W. The two symmetrical sidebands peaking at ~1943 nm and ~1961 nm started to appear at a lower output power of 7.09 W.

In fact, these two sidebands originated from the MI in the third-stage amplifier, as the positions of both peaks coincided with the MI sidebands shown in figure 3.28(b). It meant that these two sidebands (1943/1961 nm) were amplified together with the signal in the final-stage amplifier but could only be distinguished at a relatively high output power. It also showed that the peaks of the MI sidebands were masked by the ASE in the third preamplifier with 130 mW of output power because at this power level, the intensity of MI-induced noise was weak as compared to the intensity of ASE in the amplifier. Two more MI sidebands emerged at ~1920 nm and ~1980 nm when the output power reached 9.08 W. It can be inferred that these two sidebands (1920/1980 nm) were indeed caused by the MI in the final-stage amplifier, because the positions of the MI gain peaks were in good agreement with the calculated value determined by the nonlinear parameter γ, the group-velocity dispersion β_2 and the peak power of the signal (see figure 2.10).
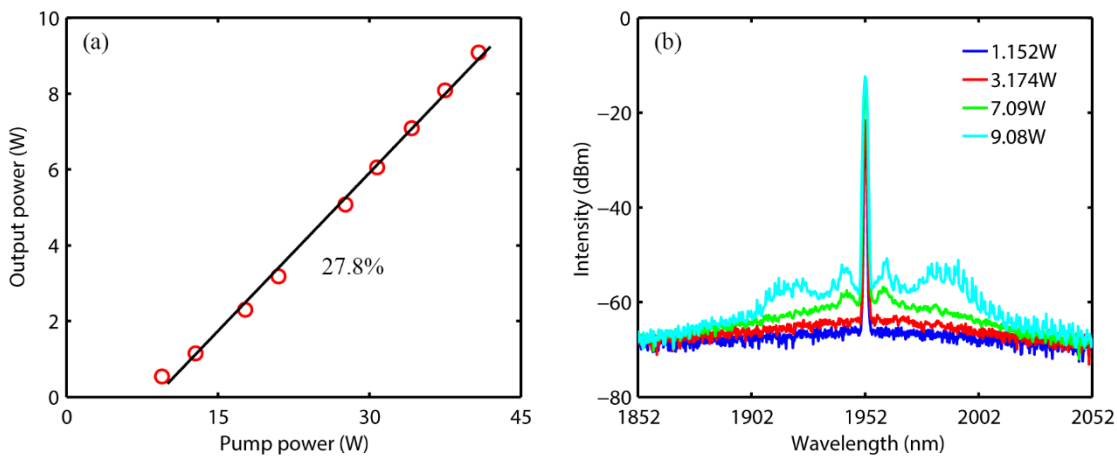
Figure 3.34. (a) Amplified output power as a function of pump power and (b) spectral plots at different output powers of the final-stage amplifier seeded with an input power of 130 mW.

So far, noteworthy improvements in nonlinearity management and power scaling were achieved in the final-stage amplifier seeded with an input power of 130 mW. However, the concealed MI sidebands from the third-stage amplifier were launched together with the signal into the fourth-stage amplifier, which resulted in nonlinear effects to become apparent at a lower power than expected. In order to avoid seeding MI sidebands into the final stage, the input power was reduced from 130 mW to only 57 mW.

Figure 3.35(a) showed that the final-stage amplifier managed to scale up the signal output power to 10.34 W at a slope efficiency of 29.5% without any power roll-off. A maximum signal gain of 22.5 dB was obtained from this amplification stage at a pump power of 45.6 W. Figure 3.35(b) depicts the autocorrelation trace measured at the output of the final-stage amplifier. The trace had a FWHM of 49 ps so that the corresponding FWHM of the Gaussian pulse width was 35 ps. The maximum peak power of the signal pulses was calculated to be 295 kW. The autocorrelation measurement showed a constant pulse width before and after the final-stage amplifier at different output powers.
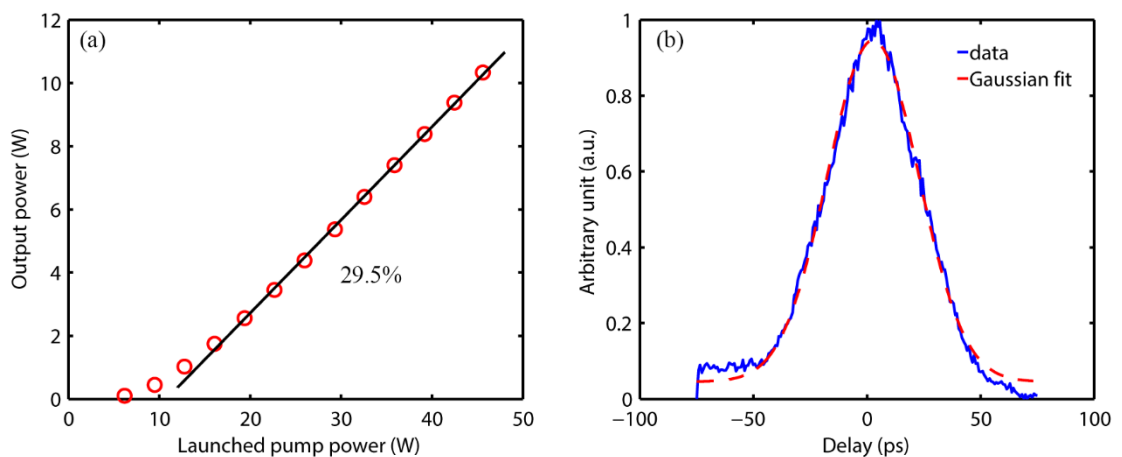
Figure 3.35. (a) Power scaling of the final stage amplifier; (b) Autocorrelation trace measured at the output of the final amplifier (4.5 W) and the corresponding Gaussian fit.

Figure 3.36 presents the spectral evolution with increasing signal output power. The signal maintained an extraordinary out-of-band OSNR of at least 40 dB. The onset of MI only became noticeable at the highest output power of 10.34 W with two symmetrical sidebands around 1920 nm and 1980 nm respectively. The seeding and amplification of the concealed MI sidebands from the third-stage amplifier was successfully inhibited in the final-stage amplifier by reducing the input power, as suggested by the green line in figure 3.36(a). Severe spectral broadening due to SPM in figure 3.36(b) was also an indication of the high peak power of signal pulses inside the fibre amplifier. The 10-dB spectral bandwidth broadened from 0.6 nm at 1.024 W to 1.7 nm at 10.34 W. In this case, SPM was inevitable because pulses with high peak power were propagating along the fibre but was significantly reduced by using a short device length.

Because of the choice of a counter-pumping scheme in conjunction with high gain operation, the effective nonlinear length was considerably reduced, thereby inhibiting the appearance of MI in the amplifier. A lower input power of 57 mW into the final-stage amplifier enabled an enhancement in output power from 9.08 W to 10.34 W with a less noisy spectrum, as compared to the output when seeding the amplifier with 130-mW input power. Figure 3.37 shows the output beam profile of the four-stage thulium doped fibre MOPA. The system had a near-diffraction-limited output with a beam quality of $M^2 \sim 1.2$ at 4.5 W of average output power, which degraded slightly to $M^2 \sim 1.3$ at the highest output power of 10.34 W.
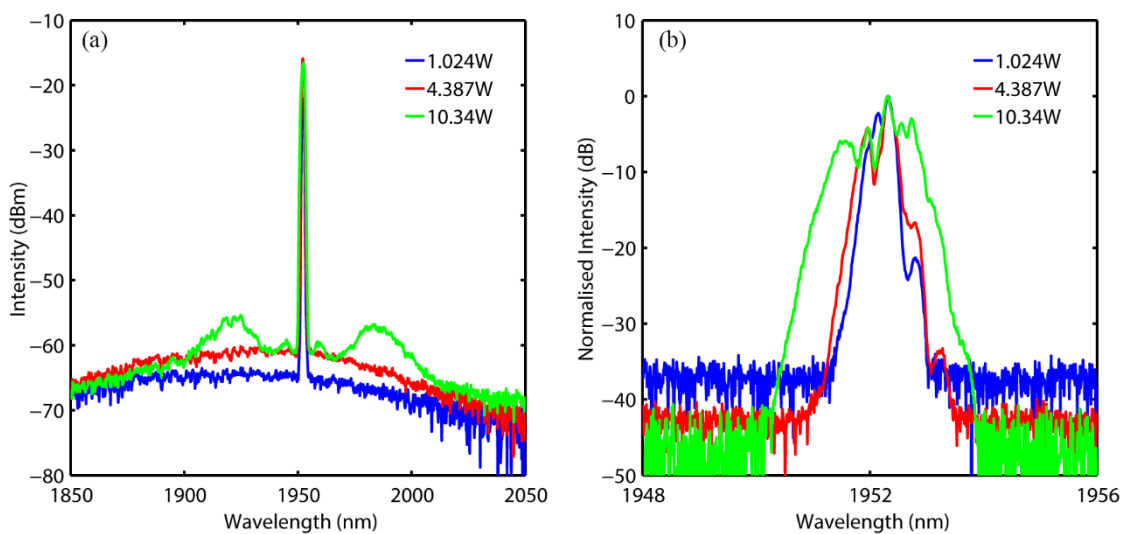
Figure 3.36. (a) Broadband spectra (1.0 nm resolution) and (b) high resolution spectra (0.05 nm resolution) of the MOPA system at 1.024 W, 4.387 W and 10.34 W average output powers.
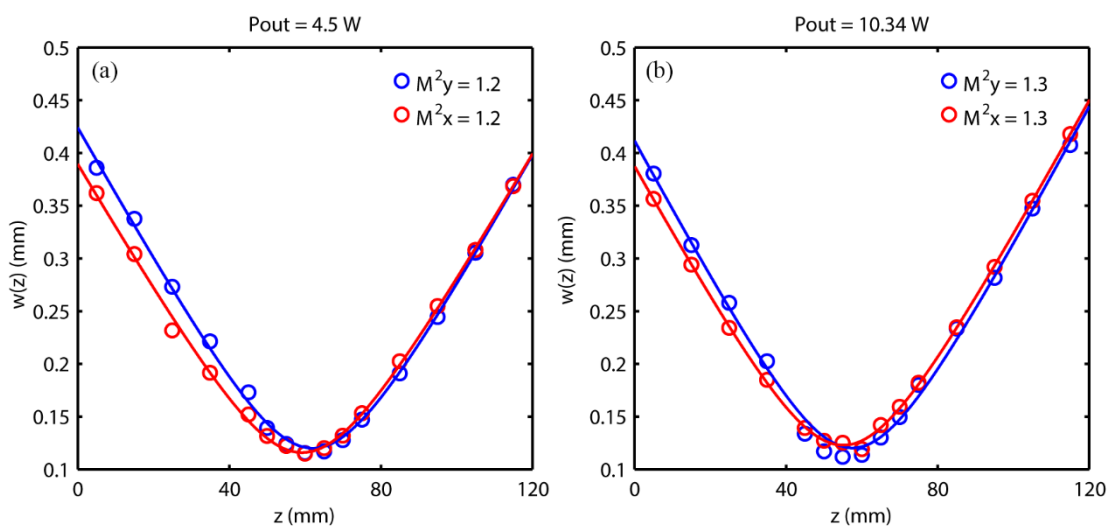
Figure 3.37. Beam quality of the MOPA output measured at the power of (a) 4.5 W and (b) 10.34 W.

3.4.4   Peak power demonstration

An excellent improvement in optical performance was achieved with the optimized four-stage thulium doped fibre MOPA system incorporating a new narrowband grating-based filter and an optimised LMA-fibre-based final-stage amplifier, enhancing the signal peak power from 76 kW to 295 kW.

An InGaAs photodetector was used to examine the peak power of the signal pulses based on two-photon absorption (TPA) process in order to verify the accuracy of the MOPA output. Note that the InGaAs photodetector had a very low and negligible responsivity at 2 µm but high responsivity in the near-infrared. The experimental setup is sketched in figure 3.38. A mirror with a reflectivity of 12% was placed at the output of the MOPA to attenuate the average power for the photodetector. An uncoated plano-convex lens with a focal length of 20 mm was used to focus the MOPA output onto the small aperture of the photodetector, electrical output of which was connected to an oscilloscope for power analysis. The residual output of the MOPA system was terminated by a beam block. It can be seen from figure 3.39 that the amplitude of the TPA-induced signal read from the oscilloscope increased quadratically with the output power of the MOPA. But the data started to roll off at output powers beyond 6.5 W, which was attributed to the power saturation of the photodetector. Note that this could be addressed by further attenuating the MOPA output. However, we did not have a suitable filter at the time to improve the test results. In spite of a slight roll-off, the results of the test confirmed the generation of picosecond pulses with high peak powers from the four-stage thulium doped fibre MOPA system.
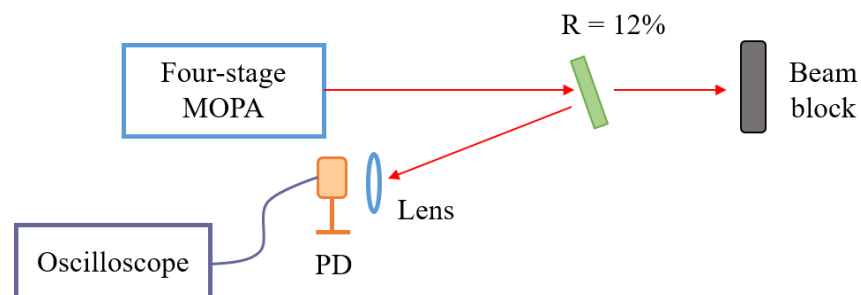
Figure 3.38. Schematic of the peak power demonstration test.
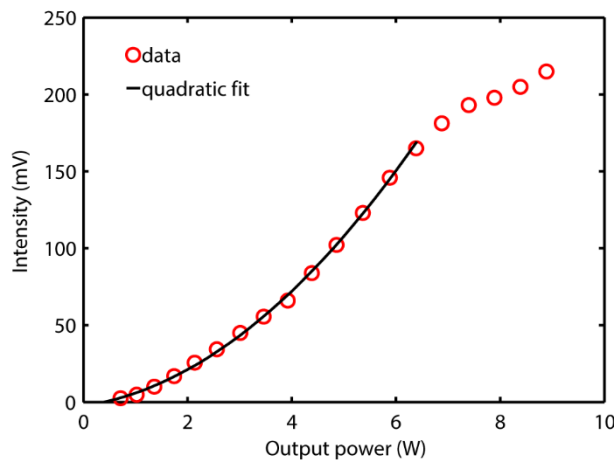
Figure 3.39. Results of the peak power demonstration test.

3.5 Conclusion

In this chapter, I discuss the high-peak-power picosecond pulse generation from a gain-switched diode-seeded thulium doped fibre MOPA system. Gain-switching a laser diode offers an easy approach to produce short picosecond pulses with a simple configuration. A 1952-nm discrete-mode laser diode was gain-switched to generate sub-hundred picosecond pulses at 1-MHz repetition rate with an average output power of ~1 µW. I have built a three-stage thulium doped fibre MOPA, comprising two core-pumped preamplifiers and a final-stage amplifier based on LMA fibre, which yielded picosecond pulses with 52-ps pulse duration, 3.94-W average output power, 76-kW peak power and a beam quality of M^2~1.6.

Further peak power scaling of the three-stage thulium doped fibre MOPA system was inhibited by nonlinearities observed in the final-stage amplifier, among which MI was the primary constraint due to the innate anomalous dispersion of silica-based fibres. From this perspective, MI cannot be thoroughly eliminated in thulium doped fibre amplifiers but increasing the nonlinear threshold of the amplifier could suppress the emergence of MI at a higher power. On the other hand, SPM and FWM can initiate and promote the growth of MI if the frequency components generated from these two processes fall within the MI gain spectrum.

Consequently, I proposed a four-stage MOPA structure to address the deleterious nonlinearities and enhance the power scalability. The four-stage thulium doped fibre MOPA featured an FBG-based filter to improve the signal purity, a new cladding-pumped preamplifier as a power compensator, and an optimised final-stage power amplifier using a very short piece of LMA thulium doped fibre. The

76

grating filter narrowed the signal spectrum down to 0.5 nm, removing the additional longitudinal mode from the seed and the extra spectral contents from the preamplifiers. A clean signal output with an OSNR of 55 dB was obtained after the filter. To make up for the high insertion loss of the grating filter, I built another cladding-pumped TDFA to boost the signal power to 57 mW. In the final-stage amplifier, I accomplished power scaling to 10.34 W with a slope efficiency of 29.5% and an excellent output OSNR of at least 40 dB. The output of this four-stage MOPA had a pulse width of 35 ps, a record-breaking peak power of 295 kW and a near-diffraction-limited beam quality of $M^2 \sim 1.3$. The attainment of high-peak-power pulses suggests effective nonlinearities management in our system. In comparison with the previous works [30, 87], considerable improvement has been achieved in terms of the MOPA output performance.

Chapter 4 High power ultra-broadband supercontinuum generation in fluoride fibres

4.1 Introduction

As compared to silica fibres which possess exponentially growing propagation loss beyond 2 μm, fluoride fibres such as ZBLAN fibres and fluoroindate fibres are particularly attractive for mid-infrared laser sources because of their low-loss transmission in the 3-5 μm region. Therefore, both fibres can be considered as potential candidates for mid-infrared SC generation and are worth further investigations. Typical transparency ranges of ZBLAN fibres and fluoroindate fibres are 0.5-4 μm and 0.5-5.5 μm, respectively (Figure 4.1).

Rapid development in the power scaling of Tm-doped 2-μm fibre lasers make them ideal pump sources for broadband SC generation over their counterpart 1.5-μm fibre lasers. Furthermore, pumping fluoride fibres with 2-μm fibre lasers can assist spectral broadening deep into the mid-infrared and enhance the power conversion efficiency, while maintaining the inherent advantages of fibre lasers such as high brightness and good compactness.

Table 4.1 compares the commercial single mode fluoride fibres from three popular companies. ZBLAN fibres exhibit a cost-effective solution to high power SC sources owing to more mature fabrication techniques. Low-loss ZBLAN fibres are available at a reasonable price. The general attenuation of commercial ZBLAN fibres is no more than 0.15 dB/m for 2-3 μm region. The-state-of-the-art fabrication technique has enabled ultra-low attenuation ZBLAN fibres with a record transmission loss of 0.00104 dB/m at 2560 nm [93]. However, only two companies (Le Verre Fluoré and Thorlabs) provide in-stock fluoroindate fibres. Research studies and fabrication techniques of indium fluoride fibres seriously lag behind that of ZBLAN fibres.

The SC generation from a ZBLAN fibre can be extended to ~4.5 μm with a complex configuration such as cascaded SC generation in combined active silica fibres and ZBLAN fibres [46]. However, it remains difficult to access beyond 5 μm for a ZBLAN fibre having strong attenuation from 5 μm and onwards. On the other hand, fluoroindate fibres have not been fully exploited as potential mid-infrared lasers

from 3 µm to 5.5 µm, because of the unavailability of high-quality fibres and powerful pump sources.

This chapter discusses SC generation in both ZBLAN fibres and fluoroindate fibres. In section 4.2, I demonstrated SC generation spanning from 800 nm to 4 µm in a small core (8.5-µm core diameter) ZBLAN fibre pumped by our three-stage thulium doped fibre MOPA. I achieved further SC generation into the mid-infrared by pumping a fluoroindate fibre with higher-peak-power picosecond pulses from the four-stage thulium doped fibre MOPA, which is detailed in section 4.3. A conclusion of this chapter is provided in section 4.4.
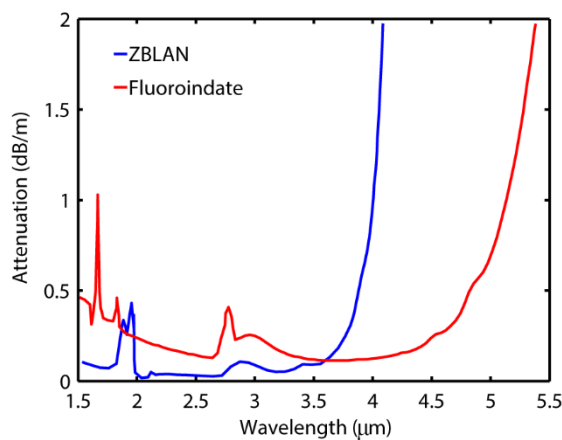
Figure 4.1. Transparency limit of ZBLAN fibres and fluoroindate fibres (data from Thorlabs).

	Le Verre Fluoré	Thorlabs	FiberLabs
Single mode ZBLAN Fibre	8.5/125 µm NA = 0.23	9/125 µm NA = 0.19	9/125 µm NA = 0.20
	<0.005 dB/m for 2000 – 2400 nm	≤0.15 dB/m for 2.3 – 3.6 µm	<0.1 dB/m for 1-2 µm
	€110/m fibre	£199.67/m cable	$160/m fibre
Single mode Fluoroindate Fibre	7.5/125 µm	9/125 µm NA = 0.26	Fibre not available
	<0.02 dB/m for 2 - 4.5 µm	≤0.45 dB/m for 3.2 – 4.6 µm	
	€200/m fibre	£226.44/m cable	

Table 4.1. Summary of fluoride fibres available from three popular companies.

4.2 Supercontinuum generation in ZBLAN fibres

4.2.1 Experimental setup

Figure 4.2 depicts the schematic of SC generation in a ZBLAN fibre. Pump pulses from the three-stage thulium doped fibre MOPA system were coupled into the ZBLAN fibre through a C-coated aspheric lens. A focal length of 4.5 mm was chosen to best match the fundamental MFD of the ZBLAN fibre. A polarisation sensitive isolator was put before the focusing lens to protect the MOPA system from any back-reflections. The half-wave plate (HWP) before the isolator was meant to provide the maximum output pump power while the other HWP was supposed to optimise the pump polarisation for the ZBLAN fibre. A 7-m-long ZBLAN fibre with flat-cleaved ends was used in this experiment. The output of the ZBLAN fibre was butt-coupled to a multimode fluoride fibre, which was connected to an OSA or a monochromator for beam diagnosis.

The tested ZBLAN fibre from Le Verre Fluoré has a core/cladding diameter of 8.5/125 µm and NA of 0.23. As shown in figure 4.3(a), this fibre had a low attenuation of less than 0.05 dB/m across the whole wavelength range from 1 µm to 3.5 µm whereas the attenuation increased rapidly beyond 3.5 µm, reaching more than 1 dB/m at 4.5 µm. The single mode cut-off wavelength of this ZBLAN fibre is 2.55 µm. Figure 4.3(b) plots the dispersion profile of the fundamental mode. The zero-dispersion wavelength located at ~1.6 µm. Therefore, the dispersion was anomalous (D ≈ 6 ps/(nm*km)) at the pump wavelength of 1952 nm.
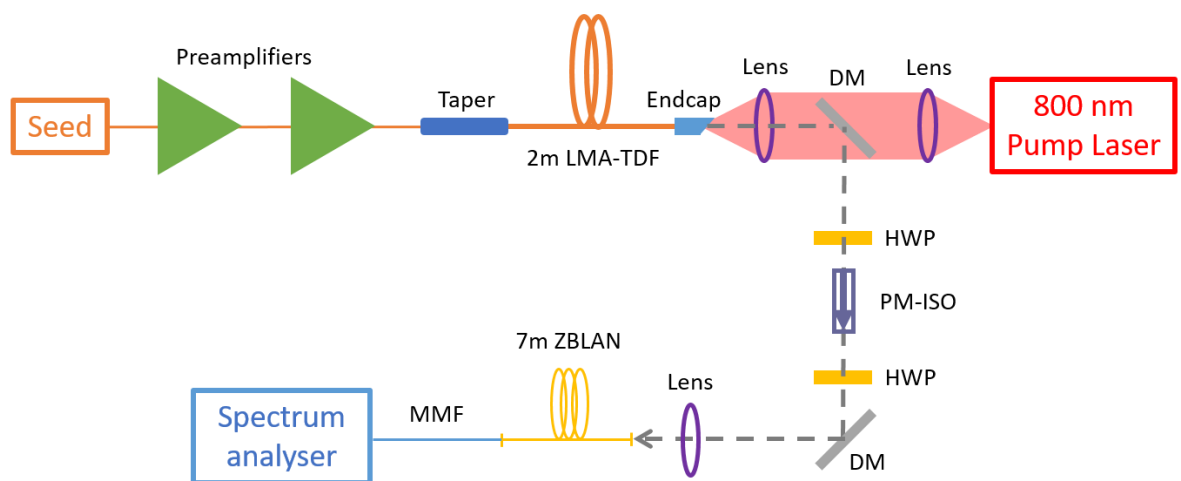
Figure 4.2. Schematic of the picosecond pumped SC generation in the ZBLAN fibre (DM: dichroic mirror; MMF: multimode fluoride fibre).
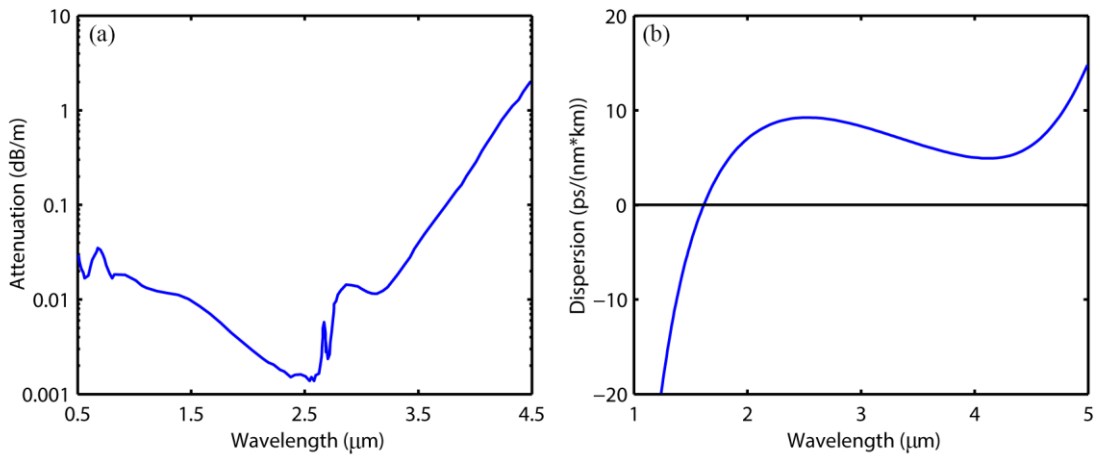
Figure 4.3. (a) Attenuation and (b) dispersion profile of the ZBLAN fibre (data provided by Le Verre Fluoré).

4.2.2   Results and discussion

Figure 4.4 describes how the spectral broadening developed in the ZBLAN fibre at different pump power levels. The full-span supercontinuum spectra were measured by a Yokogawa AQ6370 OSA (800–1600 nm), a Yokogawa AQ6375 OSA (1600–2400 nm) and a Bentham TMc300V monochromator with a liquid-nitrogen-cooled PbS detector for wavelengths above 2400 nm. The spectral resolutions of the two OSAs and the monochromator were set to 2 nm and 10 nm, respectively. Note that the OSAs and the monochromator have different noise floors.

In order to ensure an accurate synthesis of the spectra, a spectral overlap of at least 100 nm was recorded between the OSAs and the monochromator to calibrate the relative spectral intensities between the instruments. The monochromator was continuously purged with nitrogen to minimise the effects of water vapour and carbon dioxide on the measurement.

Since the MOPA did not have a linearly polarised output, the maximum available power for pumping the ZBLAN fibre became 2.52 W after the first HWP and the isolator. The pump coupling efficiency of the ZBLAN fibre was ~60%. The generated supercontinuum was typical of picosecond pumping a nonlinear fibre in the anomalous dispersion regime [94]. It can be seen from figure 4.4 that the residual pump peak was always ~20 dB above the supercontinuum at different pump powers. The supercontinuum generation broadened bidirectionally to both the near- and mid-infrared wavelengths as a result of dispersive wave and soliton self-frequency shift effects [94-97].

Initiated by modulation instability, pump pulses broke up into a large number of solitons at the beginning of the propagation inside the ZBLAN fibre. The solitons experienced a subsequent self-frequency shift and generated longer wavelengths [94, 95]. The redshift solitons transferred some energy to the blueshift radiation modes in the form of dispersive wave, when the short and long spectral contents propagated at the same group-velocity in a fibre [96, 97].
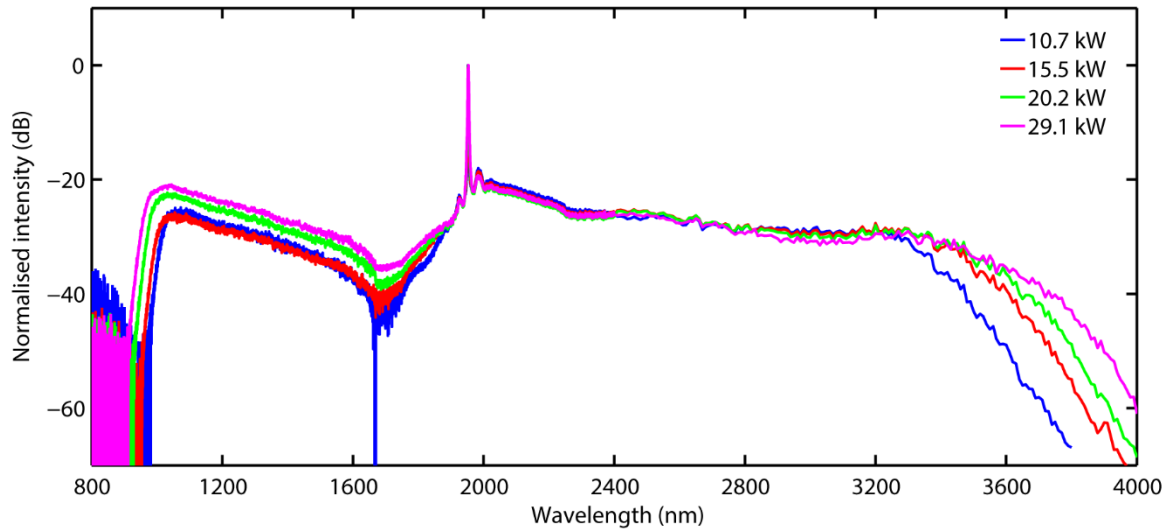
Figure 4.4. Full-span spectra of SC generation in the ZBLAN fibre at different launched pump powers.

The launched pump power was gradually increased from 0.93 W to 2.52 W, so the corresponding coupled average/peak power was increased from 0.56 W/10.7 kW to 1.51 W/29.1 kW. The supercontinuum spanned from 990 nm to 3480 nm in terms of a 20-dB bandwidth at a relatively low coupled peak power of 10.7 kW, thanks to a long interaction fibre length (7 m) and a small core diameter of 8.5 μm. The long-wavelength edge of the supercontinuum extended to 3750 nm at the highest coupled peak power of 29.1 kW while the short-wavelength edge also shifted to 925 nm accordingly with stronger spectral intensities.

It is obvious in figure 4.4 that as the coupled peak power increased, the strength of SSFS effect became weaker than that of dispersive wave due to continuous energy transfer, thereby inhibiting further frequency conversion into the mid-infrared. The fast-growing fibre attenuation beyond 3.5 μm is another reason for the slow-down in generation of longer wavelengths. Figure 4.5 presents a higher-resolution (2 nm) spectrum of the supercontinuum measured by a 3-μm OSA (Yokogawa AQ6376). The generated supercontinuum exhibited a remarkable 1.5-dB spectral flatness from 2200 nm to 3000 nm.
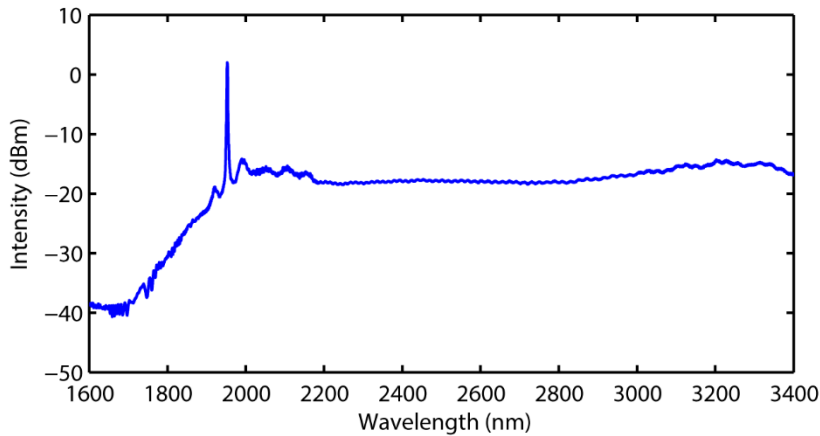
Figure 4.5. SC generation spectrum measured by a 3-µm OSA at 1.75-W of pump power.

Output power of the supercontinuum was measured by a thermal power meter (Ophir). As shown in figure 4.6, the maximum pump power yielded a total average output power of 0.746 W. Figure 4.7 characterises the distributed power and power conversion efficiency of selected mid-infrared wavelength regions (above 2500 nm and 3000 nm). Here, the power conversion efficiency is defined as the ratio of regional power to total output power. The regional power was calculated from the measured output power and measured power spectral densities. Maximum output powers of 95.8 mW and 51.1 mW were achieved for wavelengths beyond 2500 nm and 3000 nm, respectively. The power conversion efficiency for wavelengths above 2500/3000 nm reached the peak value of 19%/7.5% and then gradually decreased to 12.8%/5.3%. This was in accordance with the observed weakened SSFS effect at higher pump power.
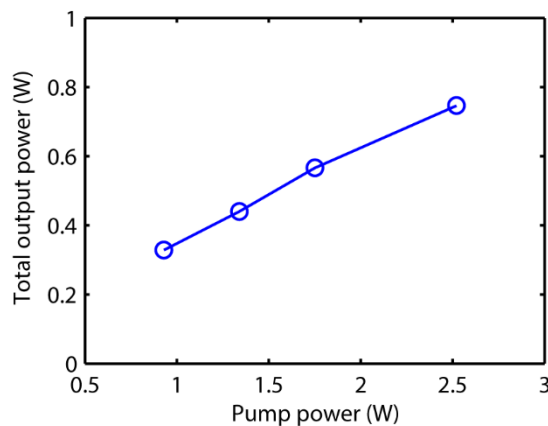
Figure 4.6. Total output power of ZBLAN-based SC generation as a function of launched pump power.
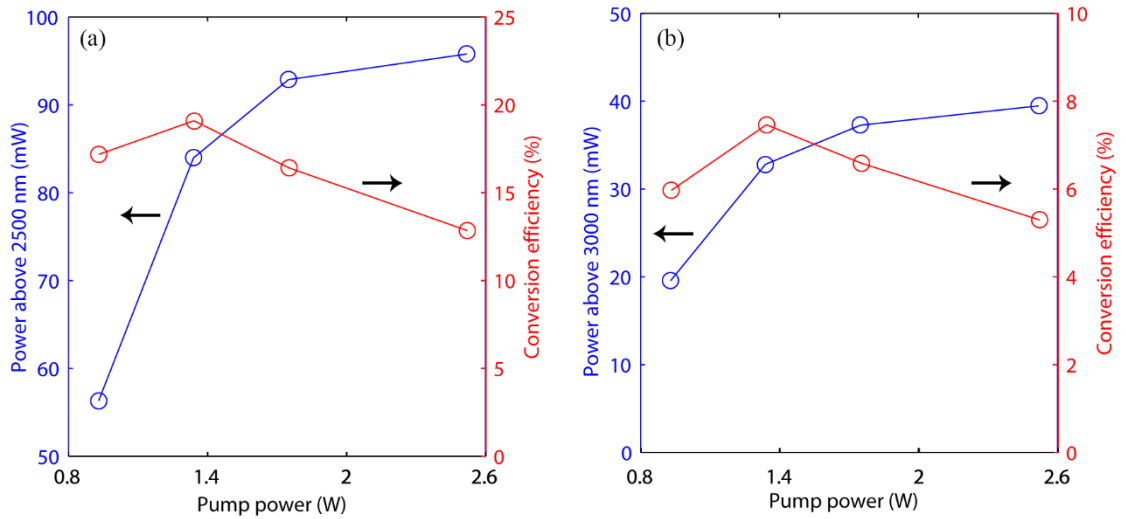
Figure 4.7. Power and conversion efficiency for wavelengths above (a) 2500nm and (b) 3000 nm.

4.3 Supercontinuum generation in fluoroindate fibres

4.3.1 Experimental setup

It can be inferred from the results of ZBLAN-fibre-based SC generation that an even powerful pump and a more transparent fluoride fibre into the mid-infrared are required to achieve high brightness SC generation extending beyond 4 μm. Hence this was accomplished by the high-power four-stage thulium doped fibre MOPA system and fluoroindate fibres.

The proposed experimental schematic is presented in figure 4.8, which is similar to that presented in figure 4.2. High-peak-power pulses from the four-stage thulium doped fibre MOPA system was launched into a fluoroindate fibre (Thorlabs) with an uncoated aspheric lens (f = 6.24 mm), which induced 0.5 dB loss. Both the input and output ends of this fibre were flat-cleaved. A polarisation-insensitive isolator (0.8 dB loss) was used in this case to maximise the attainable pump power as well as to protect the pump laser. A half-wave plate was employed to provide a variable input polarisation state. The multimode fluoride fibre, which was butt-coupled to the indium fluoride fibre, served as a delivery fibre and coupled light into optical instruments for spectral analysis.
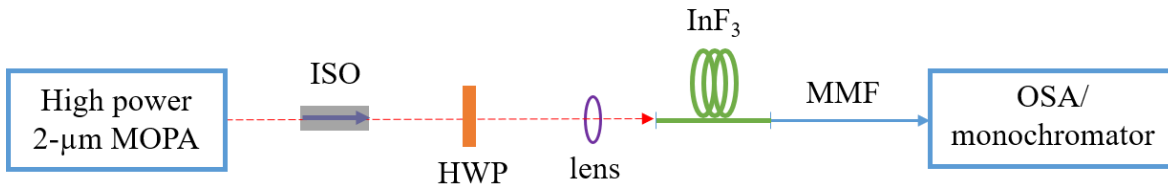
Figure 4.8. Schematic of the four-stage MOPA pumping a fluoroindate fibre (MMF: multimode fluoride fibre).

In this experiment, a shorter piece of indium fluoride fibre (4.5 m long) was first tested as a trial and another longer piece of fibre (10 m long) was used to compare the performance of SC generation in fluoroindate fibres. Both fibres under test have a core/cladding diameter of 9/125 µm, NA of 0.26 and a single-mode cut-off wavelength of 3.2 µm. As shown in figure 4.9(a), this fibre had a wide transmission window from 0.5 µm to 5.5 µm with low attenuation (<0.5 dB/m) over 1.7-4.7 µm region. Fibre attenuation increased exponentially beyond 5 µm, reaching up to ~3 dB/m at 5.5 µm. Figure 4.9 (b) depicts the dispersion profile of the fibre, indicating that it had flat dispersion over a wavelength range from 2.5 µm to 4.5 µm with a ZDW of ~1.7 µm. Therefore, the pump wavelength resided in the anomalous dispersion region with D ≈ 5 ps/(nm*km).
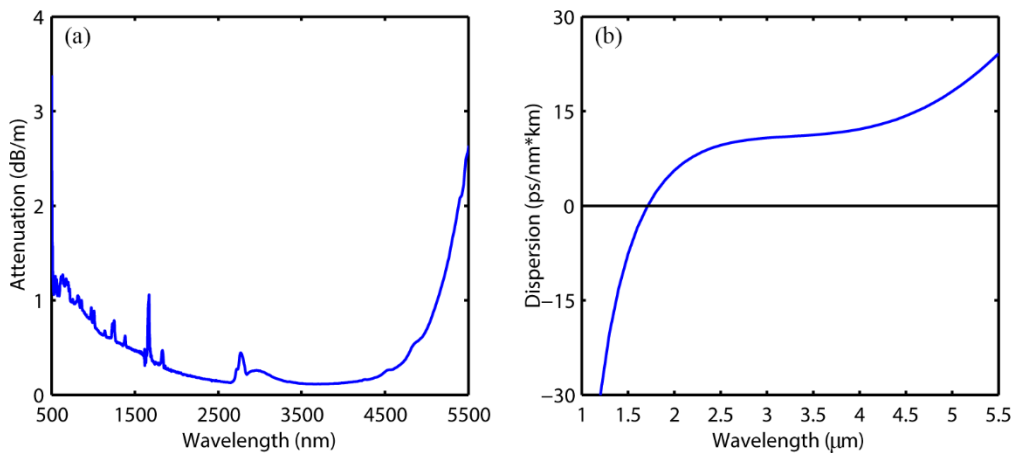
Figure 4.9. (a) Attenuation and (b) dispersion profile of the fluoroindate fibre.

4.3.2 Results and discussion

Figure 4.10 and figure 4.11 plot the spectra of the supercontinuum generated from the 4.5-m-long and the 10-m-long indium fluoride fibres, respectively. Note that the spectra were measured in the same way that mentioned in section 4.2 with an Ando AQ6317 OSA (700–1600 nm), a Yokogawa A6375 OSA (1600–2400 nm) and a Bentham TMc300V monochromator (above 2400 nm). Calibrations of relative power levels between instruments were conducted with a minimum 100-nm-wide spectral overlap during data acquisition.

The coupling efficiency was measured to be ~55% with a 1-m-long fluoroindate fibre tested under the same launching condition. It can be seen from figure 4.10 that as the coupled peak power increased from 34.6 kW to 94.3 kW, the SC generation had the bidirectional spectral broadening driven by the same physical mechanism described in the previous section. Since the employed fluoroindate fibre (0.26 dB/m) had a higher loss than the ZBLAN fibre (0.004 dB/m) at the same pump wavelength, the SC generation in fluoroindate fibres had a higher pump depletion. The residual pump peak was sitting ~15 dB above the supercontinuum.
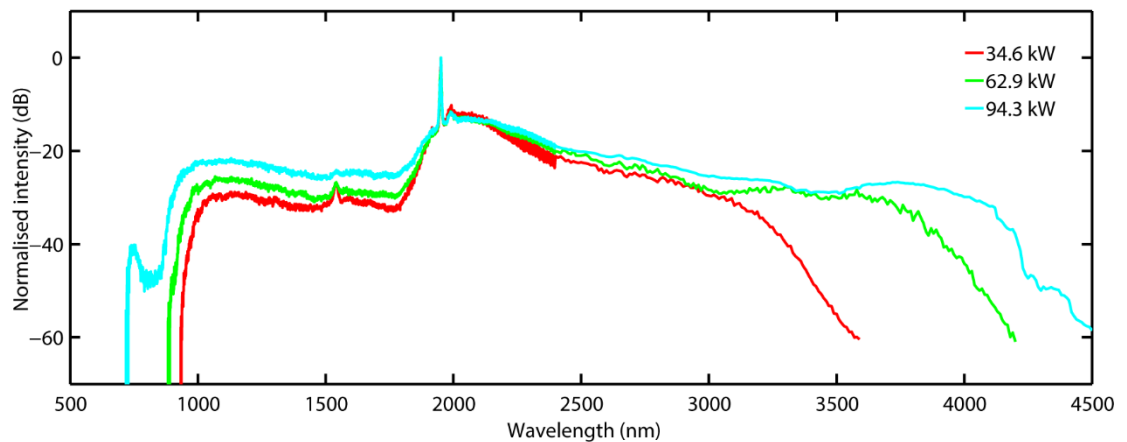
Figure 4.10. SC generation in a 4.5-m-long indium fluoride fibre.

The 20-dB supercontinuum bandwidth broadened from 3220 nm to 4150 nm at the long wavelength edge with increased pump power. However, the applicable pump power was limited to 6 W of average power due to fibre end-facet damage observed at a coupled peak power of ~100 kW. A similar damage threshold (~128 kW) was reported in the literature [55]. Compared to SC generation in the 7-m-long ZBLAN fibre (figure 4.4), this 4.5-m-long fluoroindate fibre required a higher peak power (34.6 kW) to produce supercontinuum up to 3 µm, due to a shorter interaction

length and a higher fibre attenuation at the pump wavelength. But the fluoroindate fibre outperformed the ZBLAN fibre in generating longer wavelengths at higher pump power because of its essentially lower loss at the 4-5 μm region.

Nevertheless, the long-wavelength edge of the SC spectrum generated by the 4.5-m-long fibre (4150 nm) was still far from the transparency limit of fluoroindate fibres (5.5 μm). Consequently, a longer indium fluoride fibre (10 m) was used to enhance the nonlinear effects and thus the bandwidth of SC generation. As indicated by the blue line in figure 4.11, the 10-m interaction length halved the required pump power for SC generation up to 3500 nm.
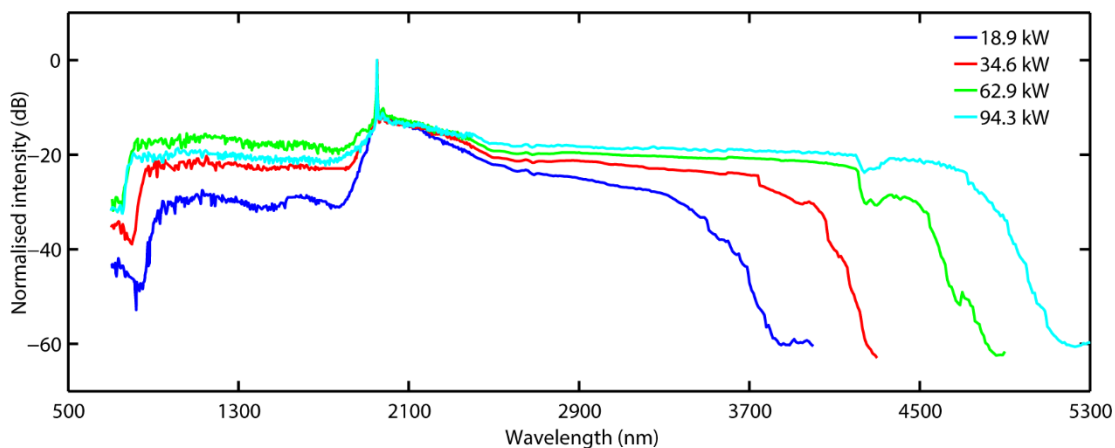
Figure 4.11. SC generation in a 10-m-long indium fluoride fibre.

When the injected peak power increased from 18.9 kW to 34.6 kW, 62.9 kW and 94.3 kW, the long-wavelength edge of the SC stretched from 3690 nm to 4160 nm, 4620 nm and 5000 nm with a benchmark of 30-dB bandwidth. Accordingly, the short-wavelength side of the SC generation extended down to 860 nm, 800 nm and 750 nm respectively. Note that at the maximum coupled peak power of 94.3 kW, the intensities of the short-wavelength spectral components did not continue to increase as expected. This was due to the fact that alignment was re-optimised at the highest pump power with the monochromator for stronger intensity at 4800 nm and preferential excitation of the fundamental mode, since the fluoroindate fibre was few-mode at the pump wavelength and single mode at wavelengths above 3.2 μm.

When the solitons redshifted from the multimode region to the single mode region, the high-order modes would be attenuated in the fibre and hence less solitons and energy would be transferred to the longer wavelengths. Therefore, better excitation of the fundamental mode in fluoroindate fibres benefited the spectral broadening into the mid-infrared at the expense of less effective energy transfer to the high-order modes in the near-infrared spectral components via dispersive wave.

Further spectral broadening to beyond 5 µm was limited by the noticeable fibre attenuation at long wavelengths and the maximum damage-free launched pump power (6W). At the highest coupled peak power, the generated supercontinuum had a 3-dB spectral flatness over an 1870-nm span from 2500 nm to 4370 nm. A slight drop in spectral intensity at ~4.2 µm could be observed in the full-span spectra (figure 4.11), which was caused by carbon dioxide absorption inside the monochromator. In this case, the monochromator was not purged due to lack of nitrogen. As shown in figure 4.12, the spectral intensity dip coincided with the absorption band of carbon dioxide.
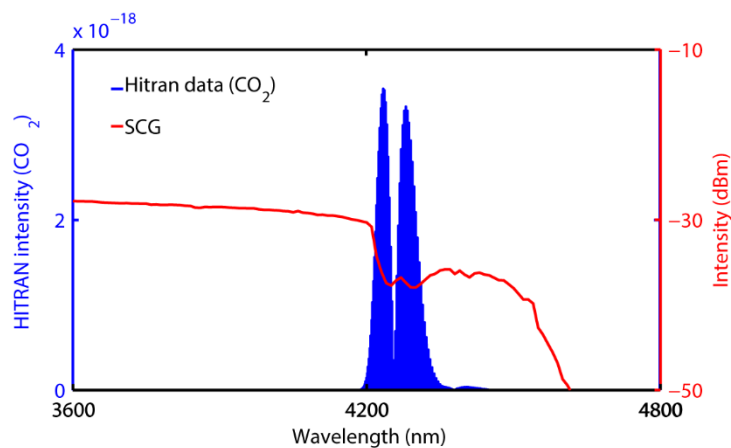
Figure 4.12. Observed CO_2 absorption in the measurement of SC generation.

A straightforward comparison of SC generation in different lengths of fluoroindate fibres at the same pump power is provided in figure 4.13. It can be seen that the nonlinear interaction length played a crucial role in mid-infrared SC generation by picosecond pumping a fluoride fibre in the anomalous dispersion regime. Under such circumstance, the soliton order is so large ($N \gg 10$) that MI dominates the initial propagation phase [79]. The nonlinear evolution of picosecond pulses inside the fluoride fibre is much slower than that of femtosecond pumping in the anomalous dispersion regime.

In the case of femtosecond pumping, fission length is much shorter so that soliton fission and subsequent soliton dynamics set in more promptly. Moreover, at the initial stage of nonlinear evolution, the high-order pump solitons compress in the time domain, resulting in the maximum spectral bandwidth before soliton fission, which contributes significantly to the ultimate supercontinuum bandwidth. Hence only a short length (usually centimetre scale) of nonlinear fibre is required to accomplish efficient femtosecond-pumped mid-infrared SC generation [79].
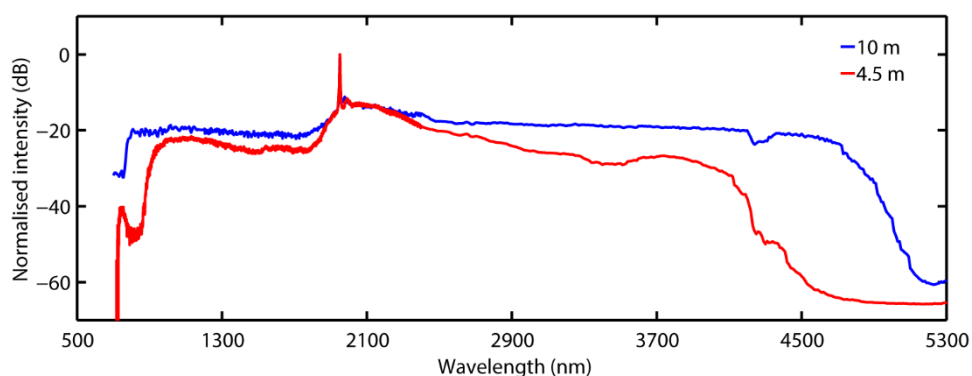
Figure 4.13. Comparison of outputs between 4.5-m-long fluoroindate fibre and 10-m-long fluoroindate fibre.

Comparatively speaking, generation of mid-infrared wavelengths by picosecond pumping a fluoride fibre principally relies on SSFS effect, as the picosecond pump normally has a narrow input bandwidth (less than several nanometre) which is not adequate for intrapulse Raman scattering. But driven by MI, the pump pulse breaks up into a large number of sub-pulses that could evolve into solitons prior to the SSFS effect. This is a slower process as compared to soliton fission, so picosecond-pumped SC generation demands a long fibre length (usually metre scale) [79].

Here for picosecond pumping the fluoroindate fibre, the additional fibre length (5.5 m) has obviously strengthened the Raman effects, indicated by the noticeable increase in both the output bandwidth and the spectral intensity. There exists an optimum fibre length for SC generation when the total fibre attenuation has just exceeded the strength of nonlinearities. However, with the available fluoroindate fibre (~10 m), further optimisation in fibre length could not be performed. But a simple conclusion could still be drawn from figure 4.13 that lengthening the fluoride fibre can help fostering the growth of long-wavelength spectral contents until the fibre attenuation becomes predominant over the nonlinearities.

Figure 4.14 shows the power scaling characteristics of the mid-infrared SC generation in the 10-m-long fluoroindate fibre. The total average output power was scaled up to 1.76 W at the maximum pump power of 6 W. Output power remained stable in the measurement for at least half an hour. A slight power roll-off was later observed in experiments. This was due to thermally induced misalignment of the setup, but same output power could be retrieved by optimising the pump coupling.
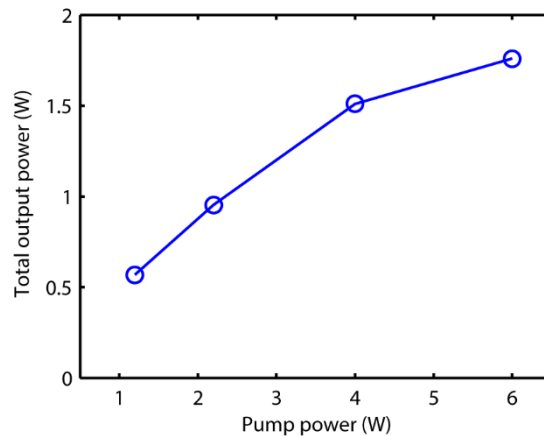
Figure 4.14. Power scaling of the SC generation in the 10-m-long indium fluoride fibre.

Figure 4.15 illustrates the power level and power conversion efficiency of wavelengths beyond 2500 nm and 3500 nm, respectively. Power for wavelengths above 2500 nm increased steadily from 63 mW to 744 mW with a maximum power conversion efficiency of 42.3%. At the maximum pump power of 6 W, up to 333 mW of power was achieved over the spectral window from 3500 nm and above. The corresponding power conversion efficiency continued to increase and reached the maximum of 18.9%.
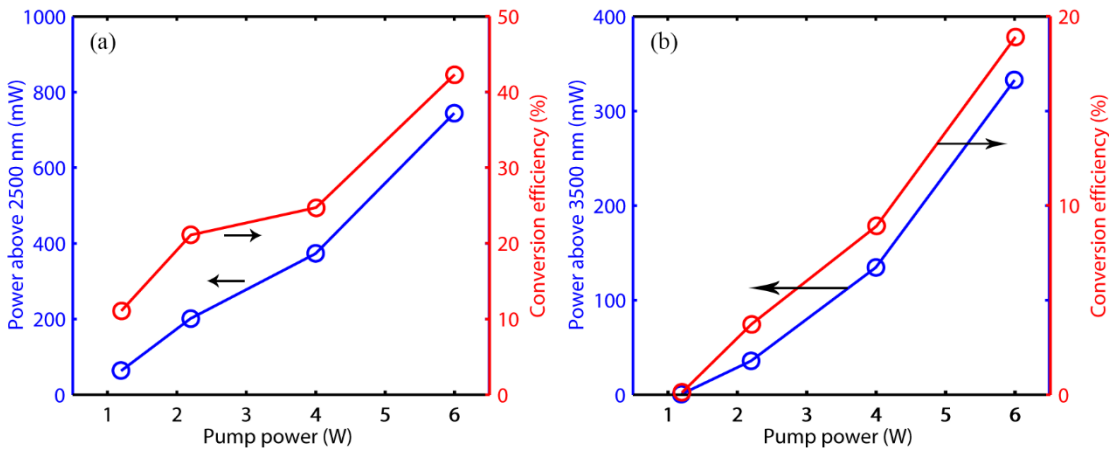
Figure 4.15. Power and conversion efficiency for wavelengths above (a) 2500nm and (b) 3500 nm.

4.4   Conclusion

In this chapter, I presented the work on mid-infrared SC generation in fluoride fibres pumped by high-power picosecond pulses at 2 μm. By pumping a 7-m-long ZBLAN fibre with the three-stage thulium doped fibre MOPA system, SC generation spanning from 925 nm to 3750 nm was achieved with a total output power of 0.746 W and an excellent 1.5-dB spectral flatness from 2200 nm to 3000 nm. However, the power conversion efficiencies for wavelengths above 2500 and 3000 nm were merely 12.8% and 5.3% due to continuous energy transfer from the long wavelengths to the short wavelengths by means of dispersive wave.

Fluoroindate fibres were then used to replace ZBLAN fibres for more efficient spectral broadening into the mid-infrared. A 4.5-m-long indium fluoride fibre pumped by the four-stage thulium doped fibre MOPA has demonstrated 20-dB SC bandwidth extending from 880 nm to 4150 nm, which suggests the potential of fluoroindate fibres for generating mid-infrared laser sources beyond 4 μm. The employment of a 10-m-long indium fluoride fibre has successfully produced ultra-broadband SC generation from 750 nm to 5 μm with a remarkable 3-dB spectral flatness covering 2500–4370 nm. The maximum pump power yielded a total average output power of 1.76 W with 0.74 W and 0.33 W obtained for wavelengths above 2500 nm and 3500 nm, respectively. The power conversion efficiencies were 42.3% (≥2500 nm) and 18.9% (≥3500 nm), respectively.
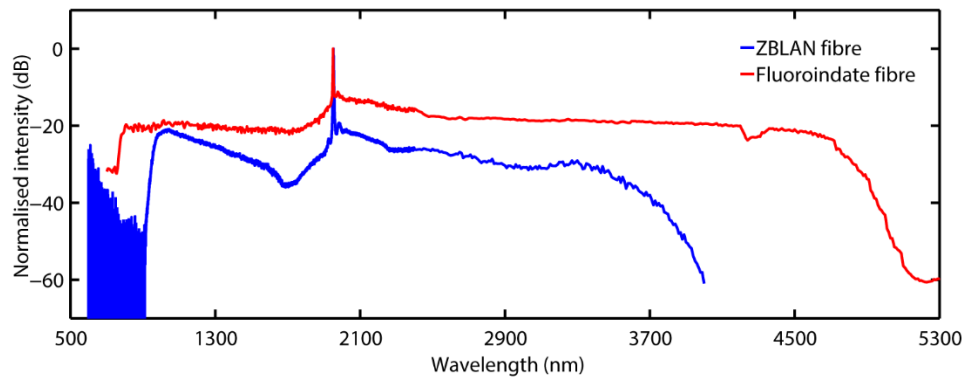
Figure 4.16. Comparison between ZBLAN-fibre- and fluoroindate-fibre-based SC generations.

Output spectra achieved from the ZBLAN fibre and the fluoroindate fibre are plotted in figure 4.16 for direct comparison between the two. ZBLAN fibres remain a strong competitor on the market for SC generation up to 4 µm because of low cost, mature fabrication technology and satisfactory performance. However, fluoroindate fibres would be a better choice for applications which demand >4-µm sources with decent output power.

Chapter 5 Frequency up-conversion of the picosecond thulium doped fibre MOPA

5.1 Introduction

Nonlinear optics is also extensively studied in transparent crystal materials which exhibit many kinds of optical nonlinearities. For example, $\chi^{(2)}$ nonlinearity which does not exist in silica fibres can be utilised in crystal materials lacking inversion symmetry for parametric nonlinear frequency conversion. Nonlinear frequency conversion offers a convenient route to generate coherent radiation where direct laser sources are not available or existing laser sources are complicated and inefficient.

Frequency doubling, also known as second-harmonic generation, is a frequently used technique to produce light emission at shorter wavelengths. Since thulium doped fibre amplifiers and lasers have a broad gain bandwidth covering 1.65–2.1 µm, frequency doubling of such systems can generate laser wavelengths ranging from 825 nm to 1050 nm, which traditional solid-state lasers may find hard to achieve [98, 99]. Ti:sapphire laser can be tuneable from 650 nm to 1100 nm, but it usually requires changing the mirror sets or employing ultrabroadband chirped mirrors in order to cover the wide wavelength range, which complicates the system operation [100]. InGaAs-based near-infrared laser diodes operating between 900 nm and 1100 nm are either power limited or with poor beam quality. However, short-pulsed 9xx-nm laser is appealing to many applications such as remote sensing and bioimaging [101-103].

Several solutions have been proposed to meet the demand of such laser systems. A ridge waveguide power amplifier seeded by a distributed Bragg reflector (DBR) laser was demonstrated to generate nanosecond pulses at 976 nm but with only watt-level peak power [104]. Ytterbium doped fibre laser is another option since it presents high emission cross-section around 976–980 nm when pumped at ~915 nm [105]. Nevertheless, it proves challenging for laser operation on this zero-phonon line because pure three-level transition around 975 nm competes for gain against quasi-four-level transition at longer wavelengths. To overcome this problem, ytterbium doped fibres with specially designed geometries are required [105,106]. However, ytterbium doped fibre lasers cannot be operated at wavelengths much lower than 970 nm due to very low emission cross-sections.

On the other hand, frequency quadrupling of thulium doped fibre laser, which is also referred to as fourth harmonic generation (FHG), can be achieved by cascading the frequency doubling process. Hence power from the thulium doped fibre lasers can be converted into the visible wavelengths from 415 nm to 525 nm. Laser emitting in the blue and violet spectral region is useful for data recording, laser microscopy, laser printing and so on [107]. Argon ion lasers can generate blue light at discrete wavelengths like 458 nm and 477 nm, but such lasers require high voltage supply and additional cooling system, resulting in a very poor power efficiency [108]. Blue laser diodes, typically based on InGaN, can emit around 400–480 nm but they are relatively low power and have a narrow spectral bandwidth of a few nanometres [109]. In terms of wavelength tunability, frequency quadrupling of thulium doped fibre lasers is superior to gas lasers and blue laser diodes with added benefits such as robustness.

Chapter 5 demonstrates the frequency up-conversion of the gain-switched diode-seeded thulium doped fibre MOPA system. Periodically poled lithium niobate was chosen as the nonlinear medium for frequency doubling and quadrupling. An overview of the PPLN crystal is first given in section 5.2. Section 5.3 discusses the frequency doubling process of thulium doped fibre MOPA in a single PPLN crystal, followed by demonstration of frequency quadrupling in cascaded PPLN crystals in section 5.4. Note that Dr. Lin Xu did the calculation for SHG and FHG, and I conducted the experiments with him. A short summary in section 5.5 concludes this chapter.

5.2　Overview of PPLN

The concept of phase-matching is revisited here for better illustration of the QPM material – periodically poled lithium niobate. For efficient parametric nonlinear frequency conversion, the interacting waves must be phase-matched ($\Delta k = 0$). Figure 5.1 illustrates nonlinear interaction in a crystal under different conditions. When the interacting waves are not phase-matched ($\Delta k \neq 0$), power oscillates between the waves during propagation along the crystal. At each coherence length, the accumulated phase mismatch equals π and the power flow reverses direction [110, 111]. In a perfect phase-matching case, the intensity of the generated wave increases exponentially with high efficiency. However, the inherent dispersion of crystal materials leads to frequency-dependent phase velocity and thus a varying

phase relationship inside the crystal. Although dispersion-induced phase mismatch could be offset by utilising the birefringence of the material, the rigid phase-matching requirement limits the number of crystal materials that can be explored for most nonlinear interactions of interest [110, 111]. Interestingly, the QPM technique allows engineering the material properties so that the sign of the nonlinear susceptibility is reversed at every coherence length, as shown in figure 5.1. This enables continuous constructive power contribution to the generated wave, albeit at a lower efficiency as compared to the true phase-matching case. Therefore, quasi phase-matching opens many attractive possibilities because efficient nonlinear frequency conversion can be obtained independent of the innate material properties by introducing periodic features [110, 111].
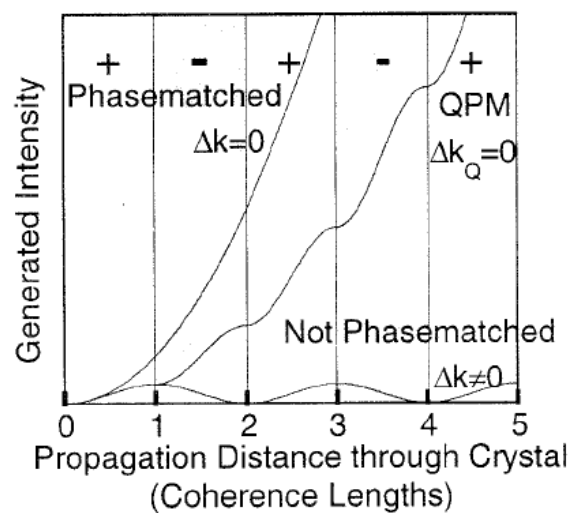
Figure 5.1. Growth of generated wave for phase-matched, not phase-matched, and QPM interactions [110].

The QPM technique was invented in 1962 [112], but it was not until the 1990s when periodic poling was successfully developed to engineer the crystal properties that lithium niobate has aroused research interests as an attractive QPM material [110, 113]. Lithium niobate is a ferroelectric crystal with a transparency range spanning from 400 nm to 4500 nm. Applying an intense electric field (~21 kV/mm) to the lithium niobate can invert the crystal structure and hence reverse the sign of the nonlinear coefficient. In order to produce PPLN, a periodic electrode delivering high voltage is deposited on the lithium niobate wafer to flip the orientation of the crystal. After periodic poling, the PPLN crystal can provide the freedom of choosing any polarisation of the interacting waves and the access to nonlinear coefficients that are unavailable to conventional birefringently phase-matched process [110].

When the interacting waves have the same extraordinary polarisation, the PPLN crystal makes use of its maximum nonlinear coefficient (d_{33} = ~27 pm/V), which is much larger than other commonly used ferroelectric materials such as KTP and LiTaO$_3$ [114]. The poling period of the PPLN crystal is determined by the wavelengths of light being used. The QPM wavelength can be tuned slightly by changing the temperature of the crystal [115].

Lithium niobate suffers from the photorefractive effect and green-induced infrared absorption, which can degrade the beam quality and conversion efficiency at high-power operation [116–118]. In order to mitigate the photorefractive effect, it is recommended to operate the PPLN crystal at an elevated temperature between 100 °C and 200 °C, thereby diffusing the free charge carriers that cause the refractive index perturbation [119]. Moreover, adding 5% of magnesium oxide (MgO) to the PPLN crystal during fabrication is another approach to increase the photorefractive resistance of the crystal while preserving its high nonlinear coefficient [120]. These measures also enhance the damage threshold of a PPLN crystal, making it more suitable for high-power operation.

5.3   Frequency doubling in a single PPLN crystal

5.3.1   Experimental setup

Figure 5.2 shows the schematic of frequency doubling of the thulium doped fibre MOPA system. As illustrated in section 3.4, the MOPA using non-PM fibres and components did not have a linearly polarised output. Therefore, the output of the MOPA was passed through an HWP and a polarisation-sensitive isolator so as to prevent any feedback into the MOPA system and to ensure a well-defined linear polarisation for efficient frequency conversion. A second HWP was then used to further optimise the input polarisation state for second harmonic generation. The 2-µm pump beam was focused into a PPLN crystal by an uncoated plano-convex lens. A focal length of 250 mm was experimentally determined to achieve the highest possible efficiency whilst avoiding beam quality degradation due to back-conversion. This resulted in a beam waist of 200 µm at the focus ($1/e^2$ radius of intensity).

The PPLN crystal (Covesion, Ltd.) was mounted inside an oven which allowed temperature tuning from 20 ℃ to 200 ℃ with a precision of 0.1 ℃. The PPLN under test was 20 mm long and had grating periods from 28.4 μm to 33.2 μm. Both end facets of the PPLN crystal were properly coated at the fundamental (1952 nm) and the second harmonic wavelengths (976 nm) with a reflectivity of less than 1%. A dichroic mirror which was highly transmissive at 1952 nm and highly reflective at 976 nm was used to separate the fundamental pump beam and the second-harmonic output beam. In this chapter, a poling period of 29 μm was chosen to demonstrate the efficient frequency doubling of the gain-switched diode-seeded thulium doped fibre MOPA.
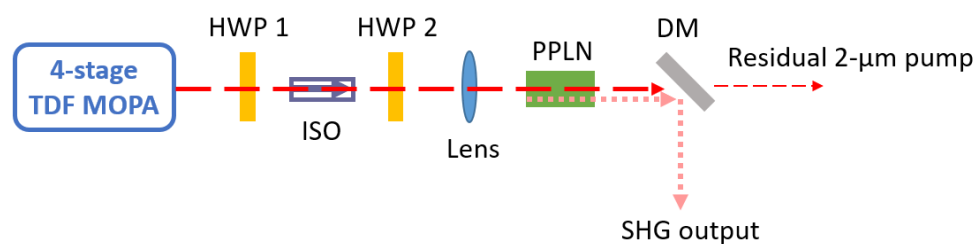
Figure 5.2. Schematic of frequency doubling of the four-stage thulium doped fibre MOPA.

5.3.2   Results and discussion

The four-stage thulium doped fibre MOPA delivered 35-ps pulses with a maximum average output power of 10.34 W and a corresponding peak power of 295 kW before the isolator. While the HWP and the polarisation-sensitive isolator turned the non-PM output of the MOPA into a linearly polarised beam, these two components introduced ~2 dB loss which led to a reduced average output power of ~6.5 W. Note that the isolator (Thorlabs, IO-4-2050-HP) in use could handle a maximum power density of 250 W/cm^2 and had an aperture for a maximum beam diameter of 3.8 mm. In order to reduce the beam intensity incident on the isolator, a pair of telescope lenses (D-coating) were used to expand the beam size, whilst silver mirrors were added to steer the beam before the HWP and the isolator which were not included in the schematic (Figure 5.2) for simplicity.

However, a reduction in output power before the isolator from 10.34 W to 8.2 W was found after hours of operation. This was attributed to the silver mirrors which was less endurable than the dichroic mirrors at high intensity. Consequently, the MOPA was operated at a lower output power (5.5 W) for long-term reliability and a maximum average output power of 3.2 W after the isolator was tested for the SHG.

According to the Sellmeier equation [121], second harmonic generation at 976 nm required a temperature of 105 °C to achieve the type 0 (ee-e interaction) phase-matching in PPLN with a poling period of 29 µm. In experiment, the SHG could be maximised when the PPLN crystal was heated to 100 °C, which was consistent with the calculated temperature of 105 °C. The output power of the SHG was measured as a function of output power from the thulium doped fibre MOPA system, which is shown in figure 5.3. At the highest pump power of 3.2 W, 1.6 W of frequency doubled power at 976 nm was generated and measured after the dichroic mirror, representing a single-pass power conversion efficiency of 50%. It was evident that the power conversion efficiency gradually increased with the increment of input pump (fundamental wave) power, reaching a peak of 67% at a pump power of 1.7 W. The conversion efficiency was saturated and then decreased at higher pump power. This roll-off behaviour was likely to be associated with the SPM-induced spectral broadening of the fibre MOPA output. Figure 5.4 characterises the pump spectra measured after the isolator. It can be seen that the 10-dB spectral bandwidth of the pump, which contained about 90% of the power, increased from 0.5 nm to 1.5 nm when the pump power was increased from 0.5 W to 3.2 W.
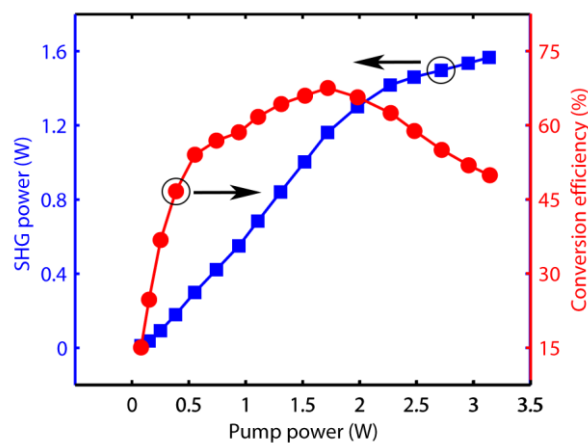
Figure 5.3. Output power and conversion efficiency of SHG (pump pulse duration: 35ps).
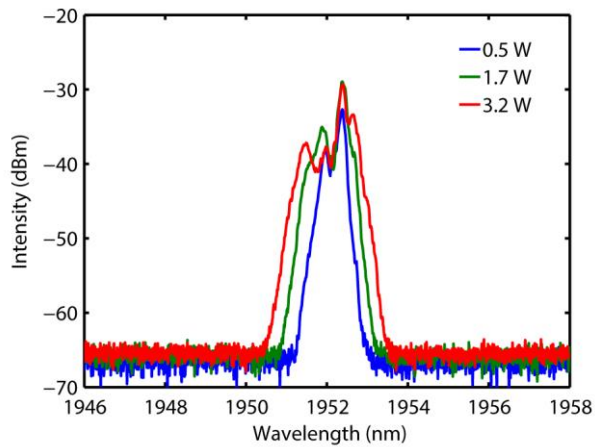
Figure 5.4. Spectra of the pump beam measured after the polarisation-sensitive isolator (pump pulse duration: 35ps).

The pump acceptance bandwidth for the SHG was then calculated so as to understand the influence of the pump spectrum on the SHG conversion efficiency. Assuming an un-depleted pump, the Jacobi elliptic function of the SHG gain can be simplified to a sinc^2 form in the low-conversion regime [122]. The pump acceptance bandwidth is defined as the bandwidth at which the second harmonic gain falls to one-half of the maximum. For frequency doubling of 1952-nm pump into 976 nm with a 20-mm-long PPLN, the pump acceptance bandwidth is 1.7 nm. Nevertheless, the simplification of the Jacobi elliptic function in the high-conversion regime becomes invalid because the width of the main lobe of the function rapidly narrows with increasing gain and thus narrows the pump acceptance bandwidth [123]. Based on a fuller calculation, the pump acceptance bandwidth for the PPLN crystal in the large-pump-depletion regime dropped to 0.5 nm for the maximum pump intensity used in the experiment. Compared to the calculated pump acceptance bandwidth of 0.5 nm, the 10-dB pump bandwidth of 1.5 nm at the highest pump power was large, which meant a less efficient utilisation of the pump power and explained the decrease in efficiency at higher pump power.

Based on the achieved results, a narrower pump bandwidth of ≤0.5 nm is requested to improve the conversion efficiency in high-power operation. In this experiment, the narrowing of the pump bandwidth was enabled by the grating-based filter in the four-stage thulium doped fibre MOPA system. The filter comprising two cascaded FBGs with the same centre wavelength but a different bandwidth acted as a narrow band pass filter, removing the out-of-band noises (see section 3.4.1). Heating up one of the two FBGs can shift its spectral window, thereby altering the

combined transmission window of the filter. Figure 5.5(a) shows the spectra of the 1952-nm beam measured at the output of the grating-based filter with two different settings. The filter operation used in section 3.4 to generate 35-ps pulses from the fibre MOPA is referred to as "filter setting-1".It can be seen from the blue line in the figure that the 1952-nm pump beam had a double-peak structure with a 10-dB spectral bandwidth of 0.6 nm.
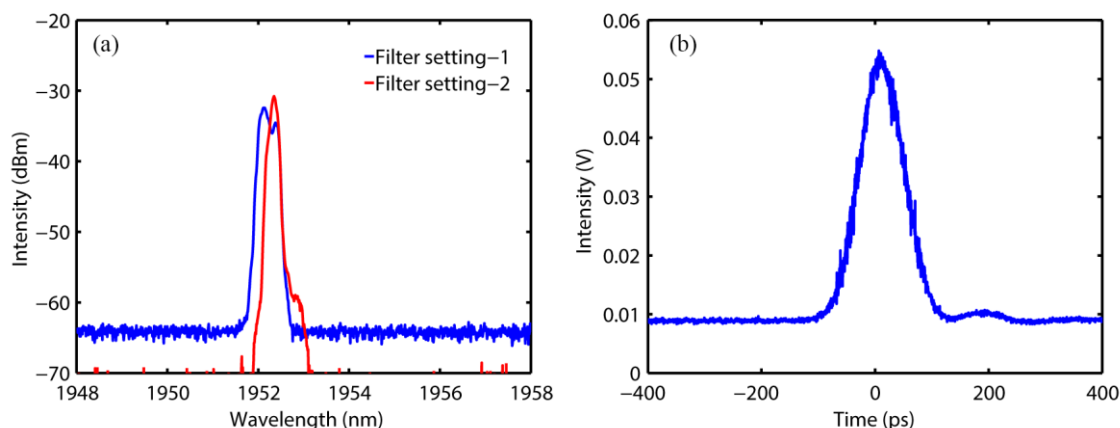
Figure 5.5. (a) Spectra of the 1952-nm pump measured after the grating-based filter with different settings; (b) Temporal profile of the pump MOPA with filter setting-2.

By heating the FBG2 in the grating-based filter from room temperature (20 ℃) to 60 ℃, the centre wavelength of this grating was shifted towards a longer wavelength. This filter operation is referred to as "filter setting-2" in the following discussion. As a result, the combined transmission window of the two FBGs was narrowed down to 0.4 nm (10-dB bandwidth) with a single peak, as indicated by the red line in figure 5.5(a). Accompanied with a reduced transmission bandwidth of the grating-based filter, the power of the 1952-nm beam after the filter decreased from 5 mW to 2.2 mW. Consequently, the third preamplifier in the thulium doped fibre MOPA system required more pump power to boost the power of 1952-nm beam to 60 mW to seed the final-stage amplifier.

The temporal profile of the 1952-nm beam changed due to the change in transmitted spectrum after passing through the grating-based filter. The pulse duration at the output of the third preamplifier was measured by a 50-GHz-bandwidth digital communications analyser (DCA) and a fast extended InGaAs photodetector with a bandwidth of >12.5 GHz. Figure 5.5(b) depicts the pulse profile, which was Gaussian-shape with a FHWM of ~80 ps. The increase in pump

pulse width was due to the interplay between the filter response and the frequency chirp of the pulses. Note that the pulse duration (80 ps) maintained at all output powers measured after the final-stage amplifier. When operating the filter with the second setting, the thulium doped fibre MOPA system could scale the output power to a similar level before the onset of MI. Therefore, a maximum pump power of 3.2 W after the isolator was still available for the SHG. The spectral evolution of the 1952-nm pump beam was plotted in figure 5.6. The 10-dB spectral bandwidth of the pump beam broadened from 0.4 nm to 0.55 nm when the pump power after the isolator increased from 0.5 W to 3.2 W.
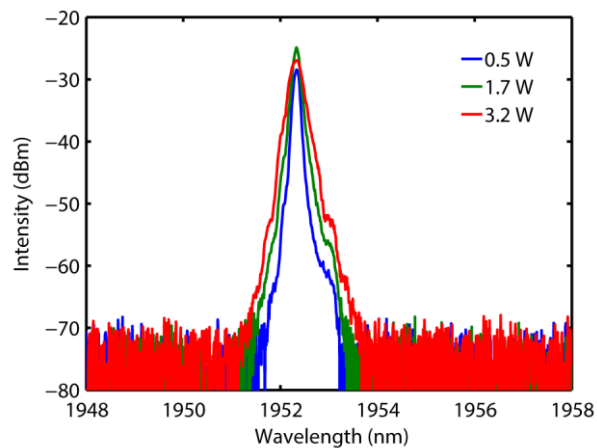
Figure 5.6. Spectra of the pump beam measured after the polarisation-sensitive isolator with filter setting-2.

In comparison with pre-temperature-tuning of the FBG, the pump spectral bandwidth was effectively reduced from 1.5 nm to 0.55 nm. This optimised pump was then used to demonstrate second harmonic generation, results of which is presented in figure 5.7. It can be seen that the generated second-harmonic power increased quadratically at low pump power and linearly at high pump power with a slope efficiency of 78%. As expected, the conversion efficiency showed no roll-off and increased steadily to the maximum at 75%, when utilising the narrow pump linewidth. At the highest pump power of 3.2 W, a maximum power of 2.4 W at 976 nm was obtained.

The spectral and temporal characteristics of the second-harmonic beam are provided in figure 5.8. The generated 976-nm beam had a 3-dB spectral bandwidth of 0.1 nm and a Gaussian pulse width of 70 ps, as measured by a 32-GHz-bandwidth InGaAs photodetector and the 50-GHz-bandwidth DCA. The maximum peak power of the generated second-harmonic pulses was estimated to be 34 kW.
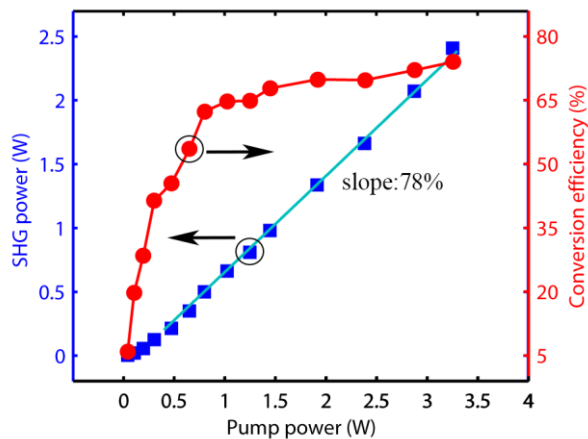
Figure 5.7. Output power and conversion efficiency of SHG as a function of pump power (pump pulse duration: 80 ps).
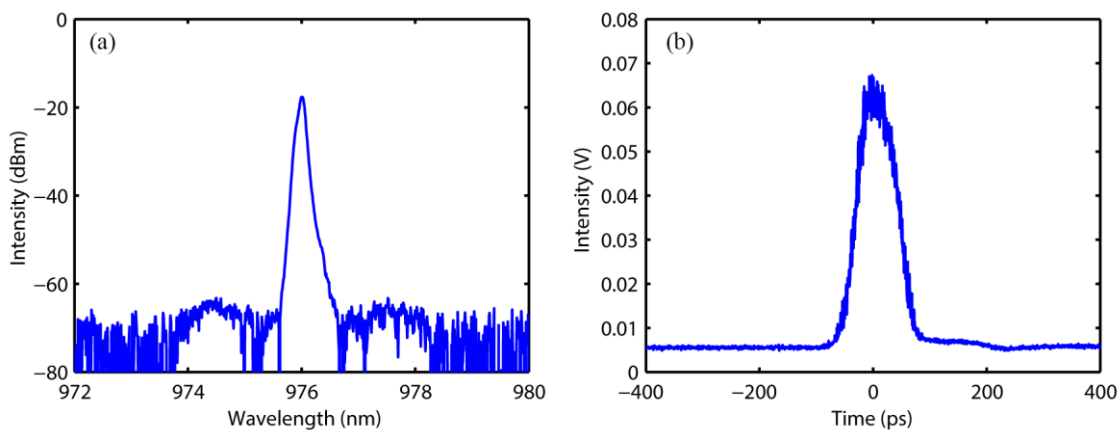
Figure 5.8. The output of SHG in the (a) spectral (0.05 nm resolution) and (b) temporal domain.

The influence of the PPLN temperature on the SHG was also studied by measuring the power of 976-nm light whilst tuning the crystal temperature. As shown in figure 5.9, the solid curve was a sinc² fit to the measured data points, confirming the expected temperature dependence of SHG. The FWHM of the curve is 7.5 ℃, which was in good agreement with the calculated value of 8 ℃ from the Sellmeier equation [124]. Figure 5.10 illustrates the beam quality of the second-harmonic beam measured by the Ophir Nanoscan. The 976-nm output had a beam quality of M²~1.7/1.8 at the x/y axis, which was slightly degraded as compared to the beam quality of the 1952-nm pump (M²~1.3). This degradation was most likely related to some back-conversion of the SHG at high-power operation with a peak pump intensity of 35 MW/cm².
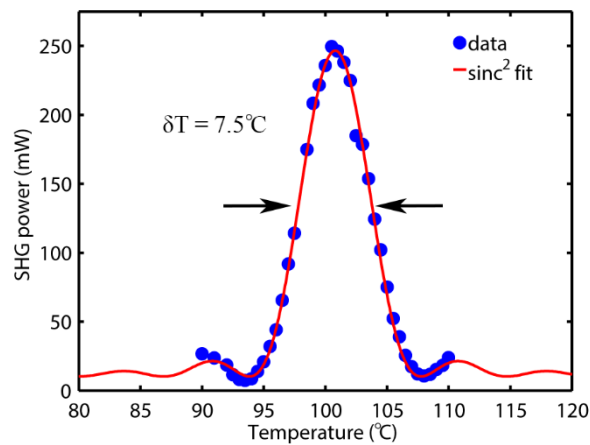
Figure 5.9. Temperature dependence of the second harmonic output and the sinc² fit.
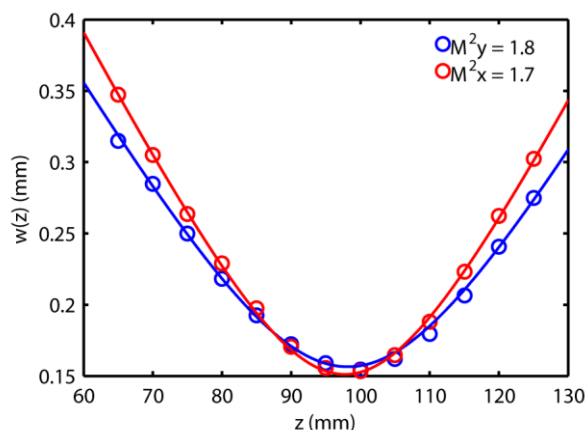
Figure 5.10. Beam profile of the SHG output.

5.4   Frequency quadrupling in cascaded PPLN crystals

5.4.1   Experimental setup

In order to achieve high-peak-power picosecond pulses at visible wavelengths for potential applications such as data storage, displays and spectroscopy [107], a frequency quadrupling stage was built by pumping another PPLN crystal with the obtained second-harmonic beam at 976 nm. The frequency quadrupling stage was highlighted in the schematic shown in figure 5.11.

The 976-nm beam was collimated by a B-coated lens with a focal length of 150 mm and then focused into the PPLN crystal by another lens with a focal length of 100 mm, resulting in a beam waist of 290 μm ($1/e^2$ radius of intensity). The PPLN crystal (Covesion, Ltd.) was 10 mm long with poling periods varying from 5.17 μm to 5.29 μm. The shorter PPLN crystal length gave a calculated acceptance bandwidth of 0.14 nm in the low-depletion regime, which was broader than the FWHM bandwidth of the 976-nm beam (0.1 nm). Both end facets of the PPLN crystal were anti-reflection (AR) coated at the fundamental (976 nm) and second-harmonic (488 nm) wavelengths. A dichroic mirror (DM3) with high transmission at 488 nm and high reflectivity at 976 nm was used to extract the fourth-harmonic beam (488 nm). Figure 5.12 shows the images of the experimental setups of frequency doubling and quadrupling.
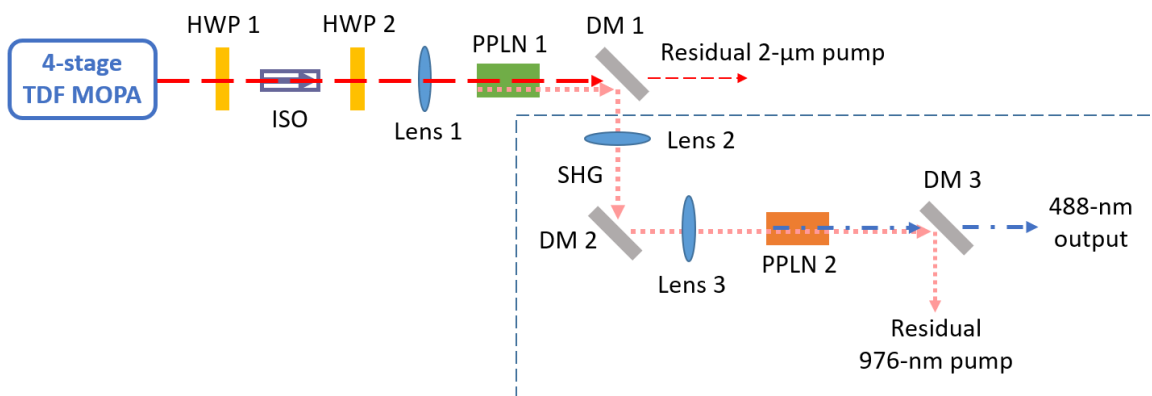
Figure 5.11. Schematic of frequency quadrupling of the four-stage thulium doped fibre MOPA.
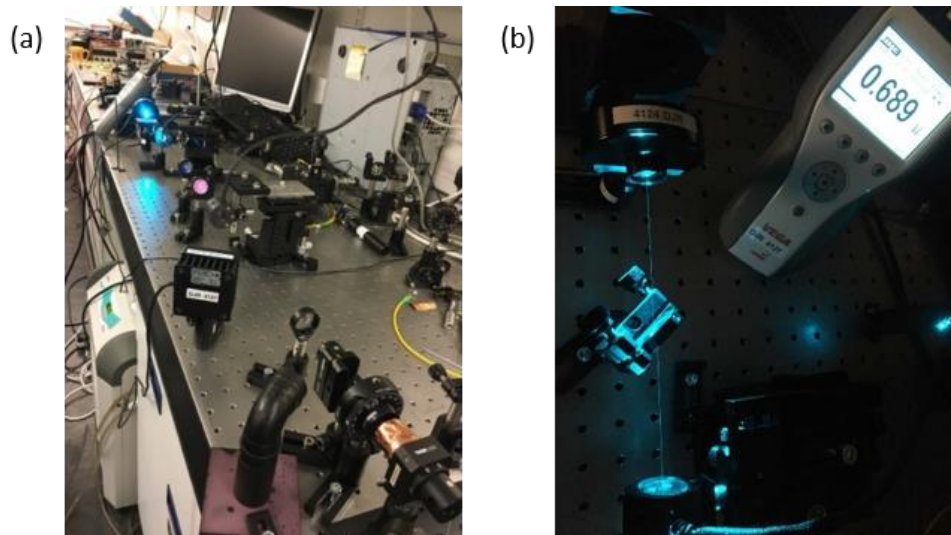
Figure 5.12. Photos of the frequency doubling and quadrupling systems.

5.4.2   Results and discussion

With a PPLN phase-matching period of 5.26 µm, frequency quadrupled blue light was observed at low pump power at a temperature of 53.2 ℃. As depicted in figure 5.13, the conversion efficiency increased rapidly to 30% at low pump powers, followed by a small drop to 27% at 0.9-W pump power, which was attributed to thermal loading via visible and induced near-infrared absorption [117, 118]. However, the downtrend could be solved by adjusting the temperature of the PPLN crystal when operating at higher pump power. By constant optimisation of the PPLN temperature, the conversion efficiency was then stabilised around 30%. The fourth-harmonic power at 488 nm was scaled up to 689 mW at a slope efficiency of 31%, with the PPLN temperature set at 52.1 ℃ and a pump power of 2.3 W at 976 nm. The lower conversion efficiency of the frequency quadrupling stage resulted from a combination of the reduced beam quality of the second-harmonic beam and the PPLN absorption.
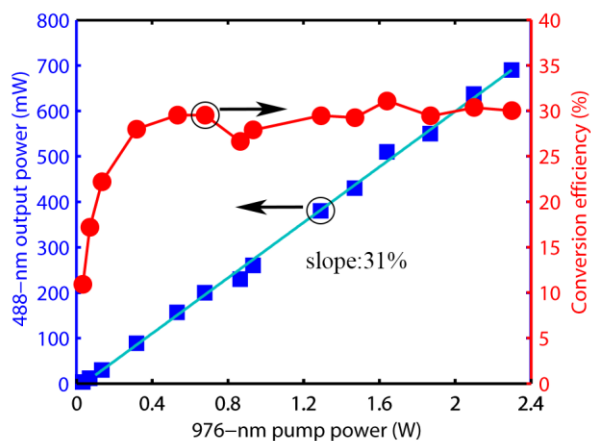
Figure 5.13. Power and conversion efficiency of frequency quadrupling.

The frequency quadrupled out had a narrow 10-dB bandwidth of 0.1 nm at 488 nm with excellent OSNR of at least 30 dB, as shown in figure 5.14. The beam quality of the 488-nm beam was characterised in figure 5.15 and measured to be M^2 ~2.1/2.0 at x/y axis. The temporal characteristics of the fourth-harmonic beam was not available due to the unavailability of fast silicon photodetectors. Assuming pulse width to be similar to that of the 976-nm beam (70 ps), the 488-nm output would have a maximum peak power of 9.8 kW.
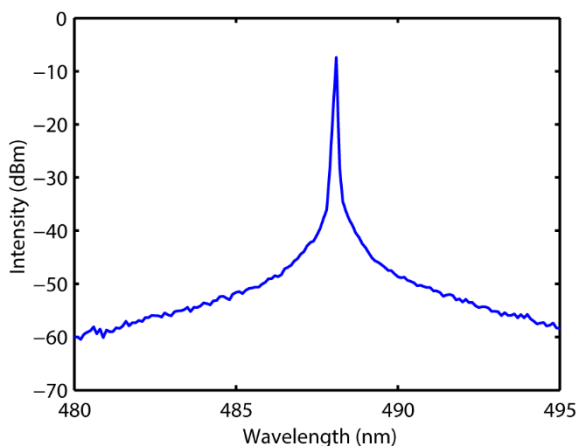
Figure 5.14. Output spectrum of the fourth harmonic generation (measured by an Ando AQ6315A OSA at 0.05 nm resolution).
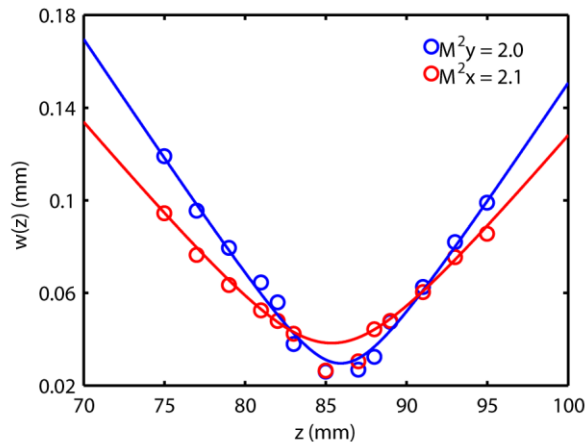
Figure 5.15. Beam profile of the frequency quadrupled output.

5.5   Conclusion

In this chapter, we have demonstrated frequency up-conversion of the picosecond thulium doped fibre MOPA system. Frequency doubling was first achieved in a single PPLN crystal with a grating period of 29 μm and a phase-matching temperature of 100 ℃. Pumped by 35-ps pulses with a highest average power of 3.2 W, the crystal generated second-harmonic beam at 976 nm with a maximum output power of 1.6 W. However, the conversion efficiency saturated and decreased with increasing pump power. The roll-off in the conversion efficiency was due to the SPM-induced spectral broadening of the fundamental beam from the thulium doped fibre MOPA.

In order to improve the conversion efficiency, the pump bandwidth was narrowed down to 0.4 nm by adjusting the transmission window of the grating-based filter in the MOPA system. As a result of a different filter response, the pump pulse duration changed from 35 ps to 80 ps with a decreased output power after the filter. Nevertheless, the thulium doped fibre MOPA system with the new filter setting could produce similar average output power for the SHG. The second-harmonic output power was increased to 2.4 W with a maximum conversion efficiency of 75%. No roll-off in the conversion efficiency was observed because of a much narrower pump linewidth. The 976-nm output had a pulse width of 70 ps, a maximum peak power of 34 kW and a beam quality of M^2~1.8. To the best of our knowledge, this is the highest efficiency ever achieved for a frequency-doubled thulium doped fibre laser.

Frequency quadrupling of the thulium doped fibre MOPA was realised by pumping a second PPLN crystal with the second-harmonic beam. Heated at 52.1℃, the 5.26-µm grating period of the 10-mm-long PPLN crystal yielded a maximum output power of 689 mW at 488 nm with a launched pump power of 2.3 W at 976 nm. A maximum conversion efficiency of 30% was achieved. The fourth-harmonic beam had a beam quality of M^2 ~2.1. Assuming a maintained pulse duration of 70 ps, the frequency quadrupled blue light would have a peak power of 9.8 kW.

Chapter 6 Optical parametric generation and amplification based on thulium-fibre-laser-pumped orientation-patterned GaAs crystals

6.1 Introduction

In addition to frequency doubling, nonlinear crystal materials can also be useful for optical parametric generation and amplification, which is often used to generate coherent light in the mid-infrared. In contrast to silica fibres with active dopants which can fulfil laser emission in the near-infrared region (1–2 μm), crystal-based parametric frequency conversion is not constrained to a narrow wavelength range defined by the laser transitions between energy levels, consequently providing flexible operation in the mid-infrared region (2–20 μm). As compared to mid-infrared SC generation in soft glass fibres which can also provide laser emission up to 10 μm, optical parametric frequency conversion based on crystals is more advantageous in terms of producing a narrow-linewidth output with high power spectral density. Furthermore, nonlinear crystal materials are suitable for high-power long-term operation because of their high damage thresholds [125]. Mid-infrared optical parametric sources with multiple merits are of great interest to a diverse range of applications such as gas detection and military countermeasures [126, 127].

Periodically poled crystals like PPLN, PPKTP and PPRTA can realise mid-infrared coherent light emission from 0.5 μm to 5 μm whilst QPM GaAs crystal is more promising for constructing long-wavelength light sources from 2 μm to beyond 10 μm, as shown in figure 6.1 [128]. GaAs crystal is an isotropic optical material without birefringent phase-matching. However, by means of molecular beam epitaxy and hydride vapor phase epitaxy, GaAs crystal can be grown with periodically inverted (orientation-patterned) structures and tailored for QPM [85, 125].

Orientation-patterned GaAs crystals possess many attractive advantages, which include a wide transparency range covering 0.9–17 μm, good thermal conductivity and a large nonlinear coefficient (d_{14} = ~94 pm/V near 4 μm) [85]. However, a primary limitation of OP-GaAs crystal is that it can only be pumped at wavelengths above 1.7 μm due to the onset of two-photon absorption [125]. Therefore, thulium

doped fibre laser is regarded as a good candidate to directly pump the OP-GaAs crystal for nonlinear frequency conversion, offering the possibility of compact footprints with high efficiency.
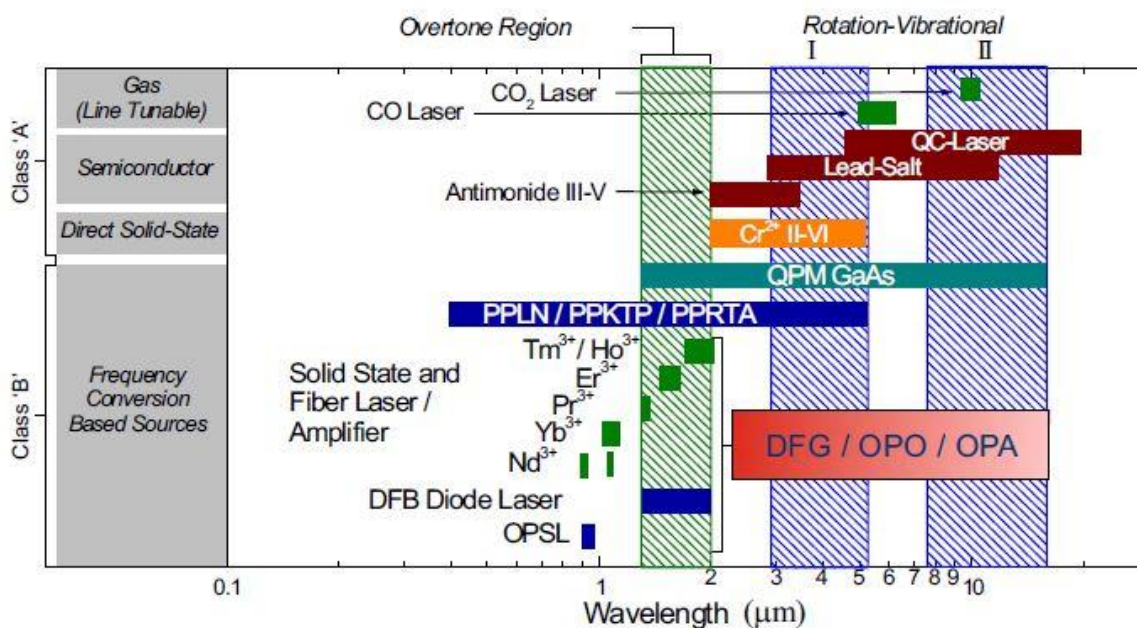
Figure 6.1. Typical operation wavelength range of various laser sources [128].

Mature fabrication and interesting characteristics of OP-GaAs crystals have driven research in this field over the past two decades, with fruitful results achieved. For instance, a nanosecond-pumped OPO using an all-epitaxially-grown OP-GaAs crystal as the parametric gain medium was demonstrated by K. L. Vodopyanov *et al.* in early 2004. Irrespective of a very low output power, the wide tuning range from 2.2 μm to 9 μm confirmed the OP-GaAs crystal as a potential material for mid-infrared lasers [85]. Since then, OP-GaAs crystal has been demonstrated in different structures for a variety of applications. Very recently, 100-ns idler pulses at 10.6 μm with a pulse energy of 16 μJ were successfully generated from an OP-GaAs OPO pumped by a thulium doped fibre laser. Average output power was as high as 800 mW in this case. However, the output peak power was low (~160 W) with a short range of tunability, which restricted the number of potential applications [129]. Using a femtosecond thulium doped fibre laser to pump the OP-GaAs crystal, a singly resonant OPO demonstrated a tuning range from 3 μm to 6 μm. With this configuration, peak power was considerably enhanced to kW level. However, strong limitation on the average output power was highlighted in this work due to the high pump intensity leading to three-photon absorption [130].

Compared to OPOs which have complex cavities and require more optical elements, optical parametric generator is an attractive alternative because of its simple single-pass nature, which allows a compact configuration with reduced cost and enhanced stability. An optical parametric generator can be modified into an optical parametric amplifier seeded by an external laser, thereby taking advantages of the spectral and spatial characteristics of the seed laser in conjunction with high parametric gain.

In 2010, G. Bloom *et al.* demonstrated the first high-gain (53 dB) OPA in OP-GaAs crystal which was seeded by a quantum-cascade laser at 4.5 μm and pumped by a Tm-fibre-laser-pumped Ho:YAG Q-switched laser. 30-ns pulses with a peak power of 580 W were obtained [131]. Another OP-GaAs OPA was lately reported to produce nanosecond pulses with a widely tuneable range in the long-wave-infrared from 8 μm to 10 μm. However, the acquired peak power was low (~140 W) and the generated beam quality was poor (M^2~3.4) [132].

This chapter presents the mid-infrared OP-GaAs-based OPG and OPA pumped by our picosecond-pulsed thulium doped fibre MOPA system. This work was led by Dr. Lin Xu with my assistance in establishing and operating the pump laser. Section 6.2 discusses the experimental setup and output results, with a brief conclusion given in section 6.3.

6.2   Picosecond-pumped optical parametric generator and amplifier

6.2.1   Experimental setup

The configuration of the single-pass OPG and OPA is shown in figure 6.2. The pump source was the four-stage thulium doped fibre MOPA described in chapter 3. Note that the grating-based filter in the pump MOPA was set to generate ~80 ps pulses with a narrow 3-dB pump linewidth of 0.5 nm for the OPG and OPA. The pump power was fixed at 4.5 W and attenuated by the first HWP and the polarising beam splitter (PBS) to avoid variation in pump linewidth as the pump power was varied.
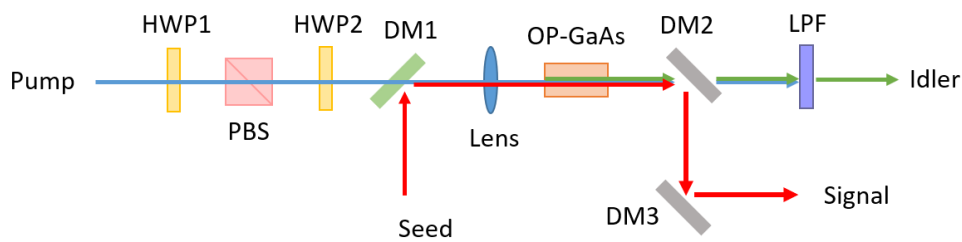
Figure 6.2. Experimental setup of the OPG (unseeded) and OPA (seeded).

The second HWP was then used to rotate the pump polarisation so as to realise the best quasi phase-matching in the OP-GaAs crystal. The pump beam and the signal beam from a tuneable Cr:ZnSe laser were combined by a dichroic mirror (DM1). The pump and signal were focused into the OP-GaAs crystal by an uncoated CaF_2 lens with a focal length of 100 mm. The beam waist at the focus was 80 μm ($1/e^2$ radius of intensity). When the OP-GaAs crystal was operated as an OPG, the Cr:ZnSe laser was off and it was turned on to deliver CW signal light when the OP-GaAs crystal was running as an OPA.

The 20-mm-long OP-GaAs crystal (BAE Systems) had five channels with different grating periods from 57 μm to 65 μm at an increment of 3 μm. Each grating had a dimension of 1-mm thickness (aligned to the [001] crystallographic axis), 5-mm width (aligned to [110]) and 20-mm length (aligned to [$1\bar{1}0$]). The pump beam propagated along the length of crystal. The crystal was mounted in an oven to allow temperature tuning. Both end facets of the crystal were AR-coated with low reflectivities at the pump (R < 1%) and signal (R < 6%) wavelengths. But the coatings had a reflection of up to 17% at the longest idler wavelength of ~8 μm.

The signal output was extracted by two dichroic mirrors (DM2, DM3) which had high transmission at the pump and idler wavelengths but high reflection at the signal wavelength. A long pass filter (LPF) with a cut-off wavelength of 4.5 μm was placed after DM2 to block the residual pump beam and measure the idler power. After passing through the various optical elements, 3.7 W of average power was available to pump the OP-GaAs crystal.

6.2.2 Optical parametric generation

With a maximum pump power of 3.7 W and a small beam waist of 80 µm, the peak intensity at the focal point inside the OP-GaAs crystal was about 230 MW/cm^2. This was well below the reported crystal damage threshold in the literature [133]. However, a higher pump intensity would cause significant three-photon absorption effects, leading to pump loss and thermal issues [130].

Results of the OP-GaAs-based OPG is first discussed. At a pump threshold of about 1.6 W, generation of signal and idler was observed without seed laser injection. The pump polarisation was set to an angle of 58 ℃ with respect to the horizontal axis (e.g. at 58 ℃ to [110]), which produced the maximal QPM in the crystal. The output power of the generated idler was measured against the angle of the input pump polarisation to further investigate the influence of the pump polarisation on the nonlinear interactions inside the OP-GaAs crystal.

As stated in literatures [85, 134, 135], the nonlinear frequency conversion is strongly dependent on the orientation of the crystallographic axes with respect to the polarisation direction of the pump, signal and idler waves. The effective nonlinear coefficient is predicted to reach the maximum value when the pump polarisation is aligned to the [111] direction (35 ℃ to the [110] axis), according to the theoretical model [134, 135].

However, the measured results in figure 6.3 showed a global maximum idler output power when the polarisation was oriented at an angle of 58 ℃ to the [110] axis. This discrepancy in polarisation could be explained by the presence of stress or thermally induced birefringence in the OP-GaAs crystal or the non-optimal optical coating for the idler [129, 135].
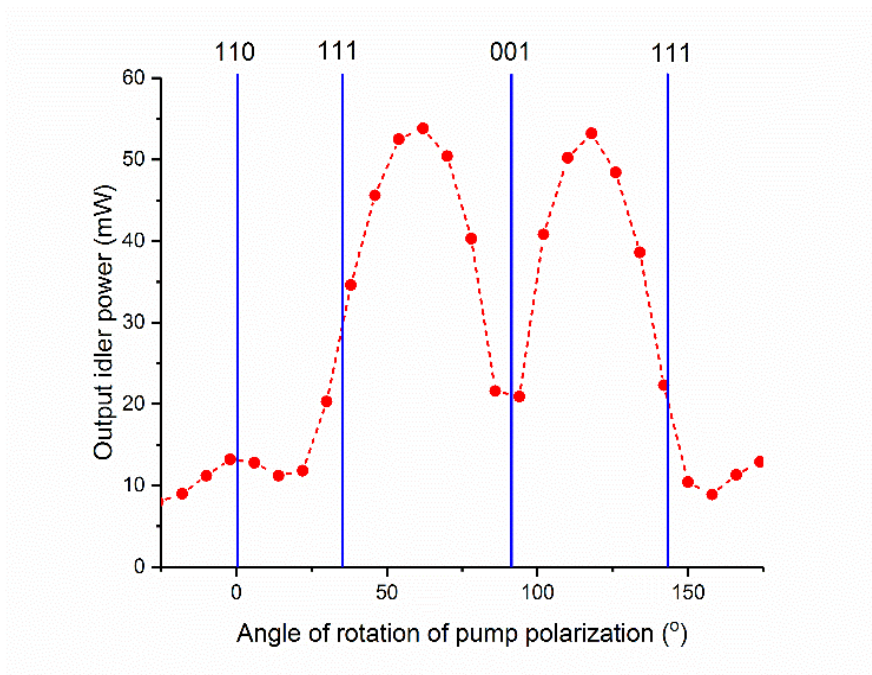
Figure 6.3. Idler average output power versus the angle of pump polarization angle and the corresponding crystal axis.

When pumped at 3.5 W, the OP-GaAs OPG yielded a maximum signal (2930 nm) and idler (5860 nm) output power of 260 mW and 160 mW respectively, with a grating period of 57 μm and an oven temperature of 50 ℃. Note that the signal and idler power reported here and in the following discussions corresponded to the powers immediately after the crystal, taking into account the losses of the DMs and LPF.

Considering the total output power of both signal and idler, the overall power conversion efficiency of the OPG was 12%. With 1-MHz repetition rate, the pulse energies were 0.26 μJ and 0.16 μJ for the signal and idler, respectively. Due to the lack of suitable equipment, the pulse durations of the signal and idler could not be measured. However, an equal or slightly shorter pulse width in comparison with the pump pulse (80 ps) was expected in the OPG process [133]. Therefore, the peak powers of the signal and idler pulses were at least 3 kW and 2 kW, respectively.

The wavelength tunability of the OPG was achieved by switching the grating periods and operating the crystal at different temperatures. Figure 6.4 shows the spectral coverage of the signal and idler from the tuneable OPG, which was measured by a monochromator with a liquid-nitrogen-cooled HgCdTe photodetector.
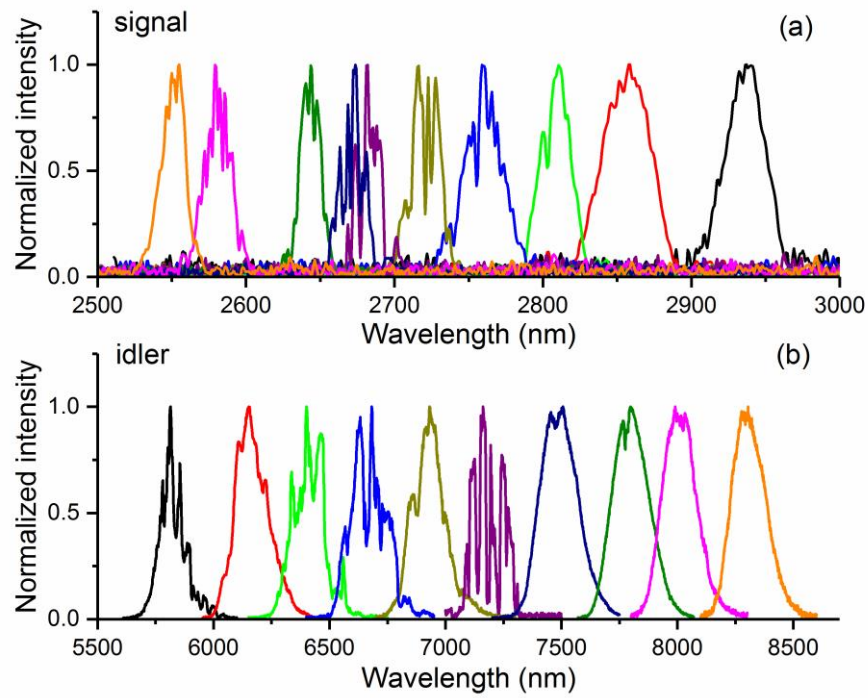
Figure 6.4. Measured spectra for (a) signal and (b) idler from the OPG.

The OPG signal wavelength could be tuned from 2550 nm to 2940 nm while the OPG idler had a much broader spectral coverage from 5800 nm to 8300 nm. The measured spectra exhibited multiple absorption lines, which was associated with strong water absorption at ~2.7 μm and 5–7 μm in air. The measured wavelengths of the OPG signal and idler matches well with our simulation data, which is depicted in figure 6.5.
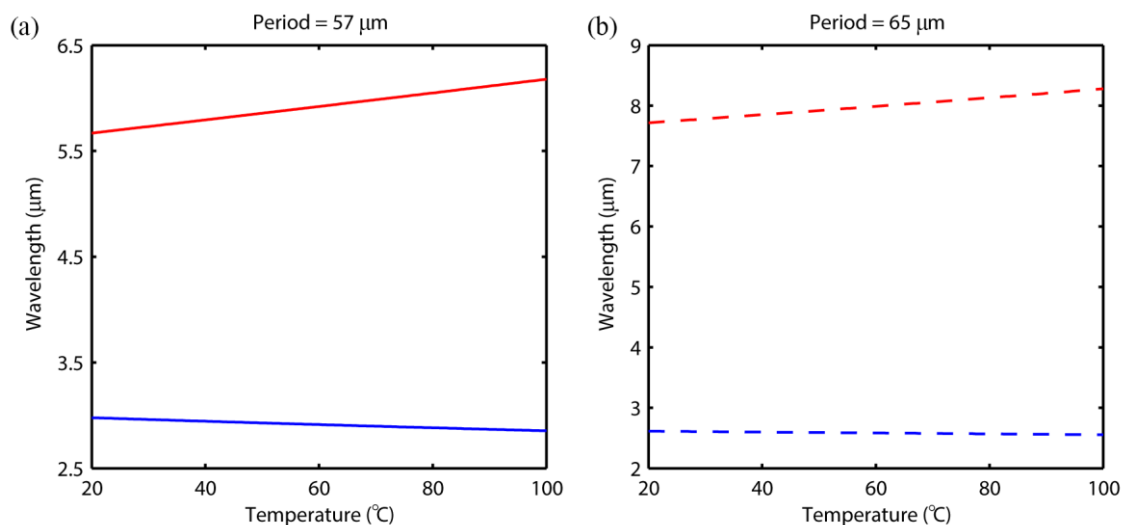
Figure 6.5. Simulated signal and idler wavelengths of an OP-GaAs OPA as a function of crystal temperature (blue lines: signal, red lines: idler).

Signal and idler wavelengths with their corresponding crystal temperatures were calculated for the shortest and longest grating periods, respectively. We can see from figure 6.5 that wavelengths of OPG signal and idler can be continuously tuned over a wide wavelength range, and that the idler wavelength is more temperature-sensitive than the signal wavelength.

The gain bandwidth, defined by the bandwidth at which the gain falls to one half of the maximum, was calculated to be ~20 cm^{-1} for the signal and idler [136]. However, the measured FWHM spectral linewidth of the OPG was relatively broader, with a signal linewidth of 29 cm^{-1} (20 nm) and an idler linewidth of 33 cm^{-1} (200 nm), as shown in figure 6.4. This linewidth broadening was possibly related to fabrication errors in gratings pitch, temperature variance along the crystal and focusing effects.

The beam quality of the signal and idler generated from the OPG was measured by the Ophir Nanoscan and characterised in figure 6.6. As shown, the signal beam had a beam quality of $M_x^2 \sim 1.7$ and $M_y^2 \sim 1.8$, whereas the beam quality of the idler was measured to be $M_x^2 \sim 2.3$ and $M_y^2 \sim 2.4$.
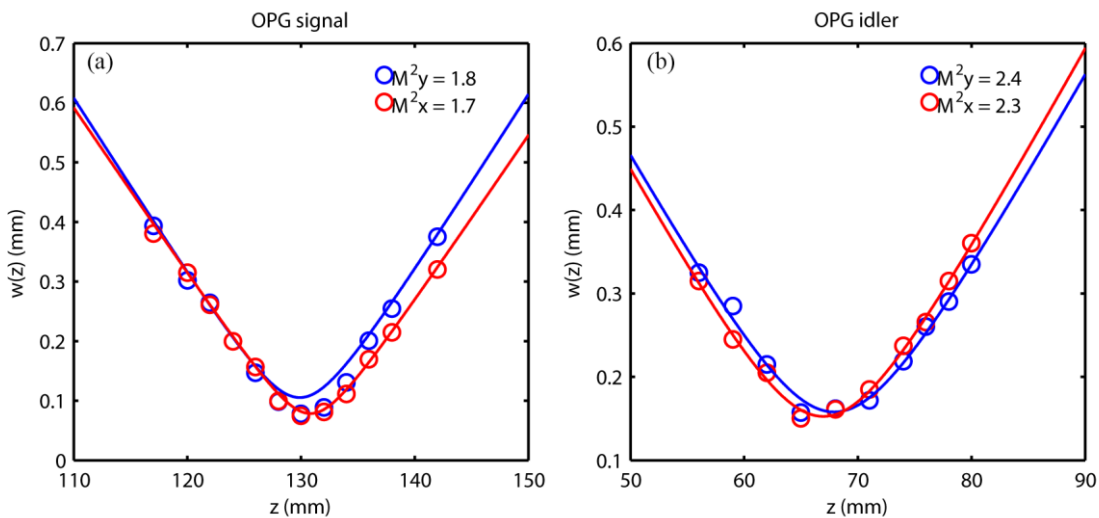
Figure 6.6. Beam quality of the OP-GaAs OPG.

6.2.3   Optical parametric amplification

To cater for some sensing applications which demand high spectral resolution, the OP-GaAs crystal was operated as an OPA seeded by the CW Cr:ZnSe laser with a narrow linewidth of 0.6 cm⁻¹. This seed laser was tuneable from 1.9 µm to 2.7 µm with an elliptical output beam, which resulted in a focusing spot size of 140 µm by 80 µm in radius. However, the pump beam was circular with an 80-µm beam waist. Therefore, good spatial overlap between the pump and signal could only be achieved in one direction.

Ideally, the conversion efficiency would be maximised when polarisations of both the pump and signal were aligned to an angle of 58 ℃ to [110]. However, the signal had a horizontally linearly polarised output (aligned to [110]), as measured directly from the seed laser output. Half-wave plates for signal wavelengths around 2.7 µm were not available in the lab at that time. Consequently, the pump polarisation was adjusted to be parallel to the seed for a maximum conversion efficiency.

The seed wavelength was set to 2650 nm to demonstrate the maximum attainable output power from the OP-GaAs OPA. It can be seen from figure 6.7 that the pump threshold decreased to approximately 1 W when 280 mW of seed power (CW) was injected into the OP-GaAs crystal.
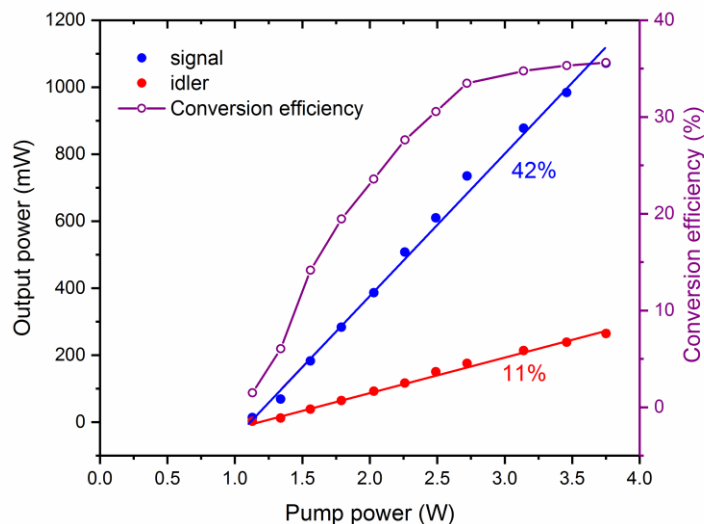
Figure 6.7. (Left) Signal and idler output power as a function of pump power in OPA operation. (Right) Total power conversion efficiency versus pump power.

The output powers of the signal (CW background excluded) and idler increased linearly with slope efficiencies of 42% and 11%, respectively. At the highest pump power of 3.7 W, a maximum signal power of 1.07 W at 2650 nm and a maximum idler power of 0.26 W at 7440 nm were obtained from the OPA.

The maximum overall power conversion efficiency was 36%. Considering a pump pulse duration of 80 ps and a 1-MHz repetition rate, only 22.4 µW out of the 280-mW CW seed power can be effectively amplified by the OPA. Hence, the 1.07-W signal output power represented a gain of 46 dB. The maximum pulse energies for the signal and idler were 1.07 µJ and 0.26 µJ, respectively. This corresponded to highest peak powers of 13.3 kW and 3.2 kW for the signal and idler, assuming that they had the same pulse width as the pump (80 ps).

Figure 6.8 compares the spectra of the signal and idler generated from the OPG and OPA respectively. As compared to the OPG operation, the OPA signal had a reduced spectral linewidth of 0.5 nm while the idler linewidth was also narrowed down to 8.5 nm. The OPA resulted in more than twenty times increase in spectral density. As expected, the frequency bandwidth was essentially transferred from the pump (1.3 cm^{-1}) to the idler (1.4 cm^{-1}) in the OPA operation, with the narrower seed bandwidth (0.56 cm^{-1}) being transferred to the amplified signal (0.71 cm^{-1}) [137].
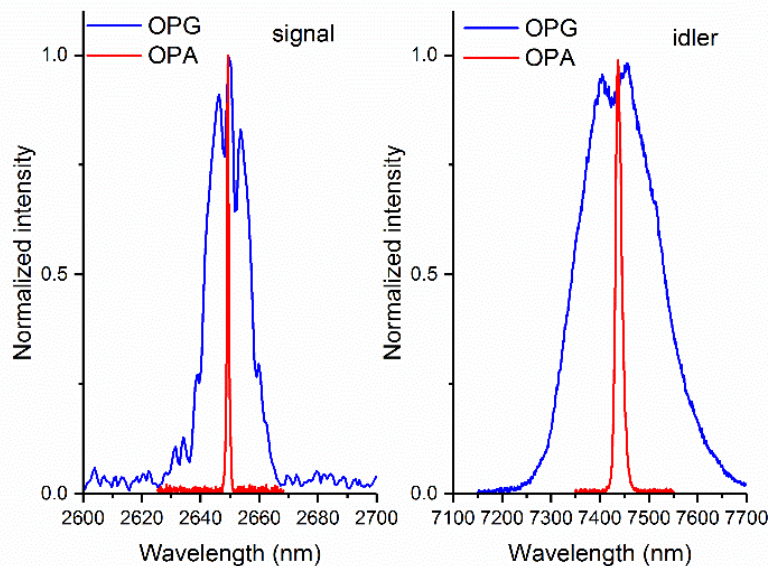
Figure 6.8. Measured spectra for signal (left) and idler (right) in both OPG and OPA mode.

By tuning the seed wavelength and working with different grating periods and temperatures, the OPA demonstrated a tuneable output signal from 2557 nm to 2684 nm and a tuneable idler from 7168 nm to 8267 nm. The wavelength tunability of the OPA was limited by the accessible wavelengths of the seed laser, which can be further improved to a spectral coverage as broad as that of the OPG by replacing the seed laser.

Figure 6.9 illustrates the beam qualities of the signal and idler from the OP-GaAs OPA. In the OPA operation, the signal beam quality degraded to $M_x^2 \sim 2.8$ and $M_y^2 \sim 2.7$ as compared to that in the OPG case. This was most likely due to the poor spatial overlap between the circular pump beam and the elliptical seed beam. However, the idler beam quality was improved to $M_x^2 \sim 1.9$ and $M_y^2 \sim 1.8$.
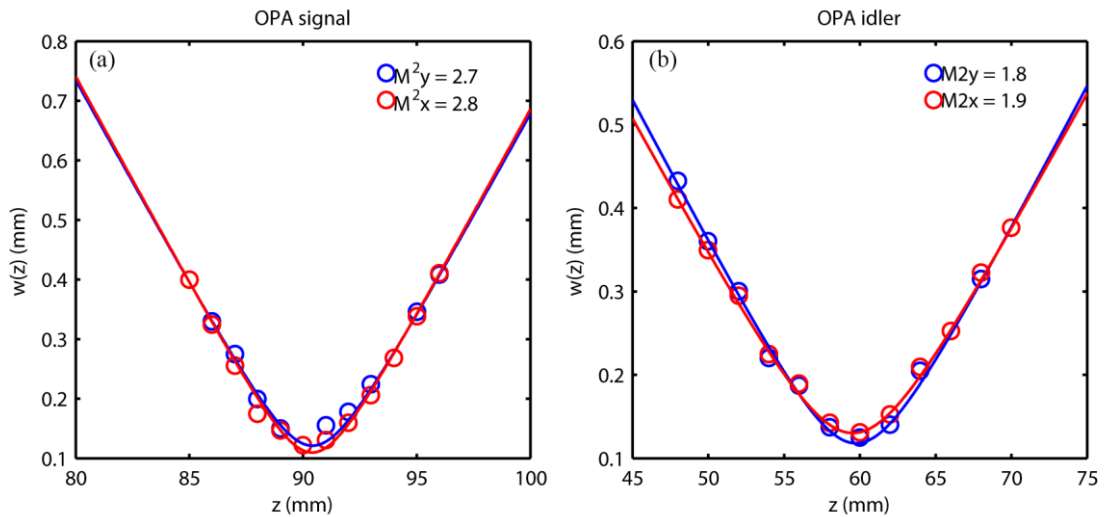
Figure 6.9. Beam quality of the OP-GaAs OPA.

To explore the influence of the seed power on the parametric gain in the single-pass OPA, signal output power and gain were measured as a function of the effective average seed power. Pump power was fixed at 3 W in this test. As illustrated by figure 6.10, a small-signal gain of up to 60 dB could be achieved. When the effective average seed power exceeded 10 µW, the extractable power from the OPA started to saturate and reached the maximum at ~0.75 W.
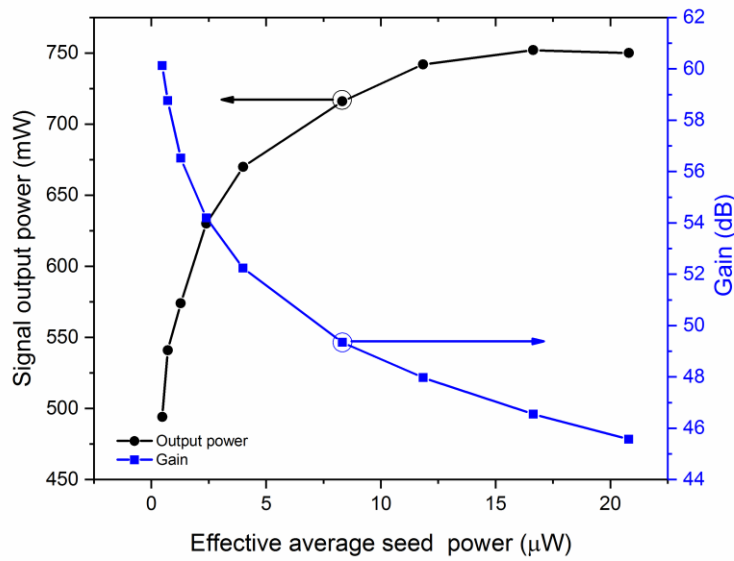
Figure 6.10. Signal output power and gain as a function of different seeding power in OPA.

6.3   Conclusion

This chapter has investigated optical parametric generation and amplification based on an OP-GaAs crystal pumped by the high-power gain-switched diode-seeded thulium doped fibre MOPA. The picosecond-pumped OPG demonstrated a widely tuneable wavelength range of 2550–2940 nm (signal) and 5800–8300 nm (idler), owing to a combination of temperature tuning and the multi-grating-periods structure of the crystal. With 3.5 W of pump power, the OPG generated a maximum signal power of 260 mW at 2930 nm and a maximum idler power of 160 mW at 5860 nm respectively, representing a total power conversion efficiency of 12%. The corresponding peak powers were 3 kW and 2 kW for the signal and idler, assuming a maintained pulse width of 80 ps during the nonlinear process. The generated signal and idler beam had a broad spectral linewidth of 20 nm (29 cm^{-1}) and 200 nm (33 cm^{-1}), respectively.

The OP-GaAs crystal was also demonstrated in an OPA configuration by employing a tuneable Cr:ZnSe laser as the seed laser. The OPA offered signal amplification for wavelengths between 2557 nm and 2684 nm, producing a corresponding idler from 7168 nm to 8267 nm. When the OPA was seeded with 280 mW of power (CW) and pumped at 3.7 W, the signal and idler powers were scaled up to 1.07 W and 0.26 W respectively, with an overall power conversion efficiency of 36%. The peak

powers were calculated to be 13.3 kW (signal) and 3.2 kW (idler) respectively, which are record mid-infrared peak powers ever reported from an OP-GaAs crystal. Seed injection to the OPA successfully narrowed the spectral linewidth to 0.5 nm and 8.5 nm for the signal and idler, leading to a pronounced enhancement of spectral density. Hence, the OPA generating tuneable signal and idler pulses with a narrow linewidth, high peak power and decent beam quality are potentially suitable for applications such as LIDAR and molecular fingerprinting.

Chapter 7 Conclusions and future work

7.1   Introduction

In this thesis, I present the development of high-power picosecond-pulsed thulium doped fibre lasers for those applications requiring high-peak-power pulses. To realise a compact device, gain-switching technique was used to generate short picosecond pulses in conjunction with power amplification in LMA thulium doped fibres. The high-power thulium doped fibre MOPAs I built were employed as a powerful pump source to demonstrate different nonlinear frequency conversion applications, which included mid-infrared SC generation, frequency up-conversion into the visible and near-infrared, and mid-infrared OPG and OPA. Experimental results of chapter 3–6 are summarised in section 7.2 and possible future areas of research are discussed in section 7.3.

7.2   Summary of the thesis

Chapter 3 elaborates the high-peak-power pulse generation from a gain-switched diode-seeded thulium doped fibre MOPA system. I have generated sub-hundred picosecond pulses by gain-switching a 1952-nm laser diode at 1-MHz repetition rate. I have also built and characterised the two core-pumped preamplifiers, which were carefully designed to provide high-gain amplification and suppress potential nonlinearities such as MI. In a three-stage MOPA structure, ASE in between amplifiers were effectively removed by a "time-gating" EOM and a commercial tuneable band pass filter, resulting in a signal power of 22 mW with a 20-dB in-band OSNR to seed the third-stage amplifier. Finally, I obtained 52-ps pulses with a maximum average output power of 3.94 W, a maximum peak power of 76 kW and a beam quality of $M^2 \sim 1.6$ from this three-stage thulium doped fibre MOPA. However, the signal OSNR was degraded to ~15 dB at the final output due to the rapid growth of ASE in the LMA amplifier as well as FWM, which was induced by the sidebands from the gain-switched seed.

Later, I proposed a four-stage configuration to address the problems existing in the three-stage MOPA and further exploit the power scalability of LMA thulium doped fibres. A main feature of this configuration was an in-house built grating-

based filter, which substituted for the commercial band pass filter in the three-stage system. While removing the ASE generated from preamplifiers, this narrow-band filter also eliminated the sidebands from the diode that could seed the nonlinearities (FWM, MI) in the subsequent amplifiers. As a result, the in-band OSNR of the signal measured after the second preamplifier was greatly improved to 55 dB.

I also added a new cladding-pumped third-stage amplifier to the system so as to boost the signal power after the grating-based filter. I reorganised the LMA-TDF-based amplifier in a way that the nonlinear threshold of the system was significantly enhanced along with an improved slope efficiency. Thanks to the larger nonlinear threshold, the average output power was successfully scaled up to 10.34 W at a slope efficiency of 29.5% in the final-stage amplification of the four-stage MOPA. The corresponding maximum peak power was 295 kW for the generated 35-ps pulses, which is the current highest peak power achieved from a picosecond-pulsed thulium doped fibre laser based on an LMA fibre. The output of this four-stage had an excellent OSNR of at least 40 dB and a near-diffraction-limited beam quality of $M^2 \sim 1.3$.

In chapter 4, I have demonstrated mid-infrared SC generation in ZBLAN fibres and fluoroindate fibres respectively. A two-octave-spanning supercontinuum from 925 nm to 3750 nm was obtained from a 7-m-long ZBLAN fibre pumped by the three-stage thulium doped fibre MOPA system, with a total output power of 0.746 W. Fluoroindate fibre was selected to extend mid-infrared SC generation to beyond 4 μm, owing to its lower attenuation in the 4–5.5 μm region as compared to ZBLAN fibres.

As requested by frequency conversion into longer wavelengths (>4μm), I used the high-peak-power four-stage thulium doped fibre MOPA to pump the fluoroindate fibres. With a 10-m-long fluoroindate fibre, I have demonstrated ultra-broadband SC generation from 750 nm to 5 μm with a 3-dB spectral flatness from 2500 nm to 4370 nm. A total output power of 1.76 W was achieved, with 0.74 W and 0.33 W for wavelengths above 2500 nm and 3500 nm, respectively. The corresponding power conversion efficiencies were 42.3% (≥2500 nm) and 18.9% (≥3500 nm). To the best of our knowledge, this is the first reported watt-level SC generation in a fluoroindate fibre.

Chapter 5 investigates frequency doubling and quadrupling of the picosecond thulium doped fibre MOPA with PPLN crystals. When the four-stage thulium doped fibre MOPA operated at high output power, the pump spectrum experienced SPM-induced spectral broadening, which became wider than the pump acceptance bandwidth of the SHG. The grating-based filter in the MOPA system was tuned to produce a narrower pump bandwidth of 0.4 nm for the SHG, resulting in a longer pump pulse duration of 80 ps. We have accomplished second harmonic generation by pumping a PPLN crystal with a grating period of 29 μm at 100 °C, which produced a maximum output power of 2.4 W at 976 nm and a maximum conversion efficiency of 75%. To the best of our knowledge, this is the highest efficiency ever reported from a frequency-doubled TDFL.

The second-harmonic output had a measured pulse width of 70 ps, a maximum peak power of 34 kW and a beam quality of M^2~1.8. Then we used the 976-nm output to pump another PPLN crystal with a poling period of 5.26 μm so as to demonstrate fourth-harmonic generation. At a crystal temperature of 52.1 ℃, up to 0.69 W of 488 nm was generated with a maximum conversion efficiency of 30% and a beam quality of M^2 ~2.1. A minimum peak power of 9 kW was obtained from the frequency quadrupled output.

In chapter 6, optical parametric generation and amplification were achieved by pumping an OP-GaAs crystal with the high-power thulium doped fibre MOPA. By tuning the crystal temperature and changing the grating periods, the thulium-laser-pumped OPG demonstrated excellent wavelength tunability, with a signal range from 2550 nm to 2940 nm and an idler range from 5800 nm to 8300 nm. With a total power conversion efficiency of 12%, a maximum signal power of 260 mW and a maximum idler power of 160 mW were generated, respectively.

A picosecond-TDFL-pumped OPA was demonstrated to accommodate applications which require mid-infrared coherent sources with a narrow linewidth and high-peak-power pulses. Seeded by a tuneable Cr:ZnSe laser, the OPA yielded a tuneable signal from 2557 nm to 2684 nm with a corresponding idler from 7168 nm to 8267 nm. The output powers for the signal and idler were scaled up to 1.07 W and 0.26 W respectively, with an overall conversion efficiency of 36%. This corresponded to maximum peak powers of 13.3 kW and 3.2 kW for the signal and idler, which are record peak powers reported from OP-GaAs-based OPAs.

Briefly, I have achieved peak power scaling to 295 kW in a picosecond thulium doped fibre MOPA seeded by a gain-switched laser diode, by virtue of effective measures to enhance the nonlinear threshold of the system. This high-peak-power thulium doped fibre MOPA was utilised to demonstrate different types of nonlinear frequency conversion, thereby creating laser sources at wavelengths inaccessible to conventional solid-state lasers. Pumped by our high-power 2-µm fibre laser, the obtained mid-infrared SC generation (0.75–5 µm), mid-infrared OPG and OPA (2.5-8.3 µm), and frequency up-conversion (488 nm, 976 nm) can meet the demand of a wide range of applications such as spectroscopy, chemical sensing and data storage.

7.3   Future work

7.3.1   Further power scaling of thulium doped fibre lasers

It is clear that nonlinear effects are the fundamental limitations on scaling up the peak power of pulsed thulium doped silica fibre lasers. Hence, thulium doped fibres with higher nonlinear thresholds are required to increase the power scaling capability. One common approach is using Tm-doped PCFs to reduce nonlinearities in high power systems, but very recently thulium doped germanate fibres [138-144] and normal dispersion thulium doped silica fibres [60, 61, 145] are also proposed to address the nonlinearity issue.

As compared to silica glass, germanate glass can provide a much higher rare-earth ion solubility which is in the order of 10^{21} ions/cm^3 [138]. Thulium doped germanate fibres with a doping concentration as high as 5.1 wt.% have been demonstrated by C. Yang *et al.* [139]. Such high concentration of thulium ions results in strong absorption and enables efficient cross relaxation. For example, C. Yang *et al.* reported a measured cladding absorption of >11.5 dB/m near 800 nm with their double-clad thulium doped germanate fibre, which is about twice as much as that of the commercial Nufern double-clad TDF (~5 dB/m at 793 nm) [139]. Thus, thulium doped germanate fibres with stronger absorption can significantly reduce the device length, thereby effectively suppressing the nonlinear effects.

Several demonstrations of cm-long thulium doped germanate fibre lasers have shown their great potential for power scaling [139-143]. In early 2007, J. Wu *et al.* successfully scaled the output power of a 40-cm-long thulium doped germanate fibre laser to 104 W at a slope efficiency of 52.5% [140]. Thulium doped germanate fibre was also lately demonstrated in MOPA structure. The germanate gain fibre was used throughout the MOPA, from the DBR seed laser to the two-stage amplifiers. The total gain fibre length used in this MOPA was less than 42 cm, which helps in obtaining a stable single-frequency output. C. Yang *et al.* reported an output power of 11.7 W at 1.95 µm and they suggested feasible power scaling to >100 W with optimised system configuration and careful thermal management [139]. At the moment, there are ongoing studies in LMA thulium doped germanate fibres in the Optoelectronics Research Centre (University of Southampton) [138]. Initial results show prospects of replacing the current LMA thulium doped silica fibre with an even shorter LMA thulium doped germanate fibre in the high-power 2-µm MOPA, which should further increase the maximum attainable output peak power.

On the other hand, normal dispersion thulium doped fibre has been recently developed to overcome the MI-induced pulse breakup in thulium doped fibre amplifiers and lasers [60, 61, 145]. Conventional thulium doped fibres have anomalous dispersion in the 2-µm region, where MI is inevitable in high power fibre lasers. Nevertheless, special fibre design can turn a fibre into normally dispersive at 2 µm. In 2018, Y. Chen *et al.* reported a W-type thulium doped silica fibre with normal dispersion at 2 µm. This fibre was used to demonstrate a mode-locked laser which yielded ultra-short pulses with a pulse width of 727 fs and a pulse energy of ~0.6 nJ [60]. In 2013, C. Baskiotis *et al.* proposed an LMA fibre design in which the Tm-doped core was surrounded by a ring of highly-doped germanium rods. They have numerically proved that such fibre structure exhibits normal dispersion at 2 µm [145]. With progressing studies in normal dispersion thulium doped fibre, it is believed that further power scaling of TDFLs can be realised in the future.

7.3.2   Development of short-wavelength TDFL

In addition to power scaling, more interesting characteristics of thulium doped fibre lasers can be investigated, such as the short-wavelength operation of a TDFL. Numerous lasers have been demonstrated in the central gain bandwidth of thulium doped fibres (1800–2000 nm) [13-18], but very few report laser operation at

wavelengths below 1750 nm [43, 98, 146, 147]. Thulium doped fibre lasers emitting around 1700 nm are very attractive for sensing, surgery and polymer processing applications since many chemical bonds (e.g. O-H, C-O, and C-H in particular) show strong absorption features in this spectral window [148, 149].

Laser emission at shorter wavelengths from thulium doped fibres is difficult since a higher population inversion is required by the three-level nature of this transition. To date, several thulium doped fibre sources operating in the 1650–1750 nm waveband have been reported, with resorts to ASE filtering and wavelength locking by FBG [42, 98].

By employing highly reflective FBGs, cavity loss at signal wavelength was minimised in a core-pumped TDFL demonstrated by J. M. O. Daniel *et al*. This TDFL was widely tuneable from 1660 nm to 1750 nm. At 1726 nm, a maximum output power of 12.6 W was produced with a slope efficiency of >60% [98]. S. Chen *et al.* utilised a Tm/Ge co-doped silica fibre in conjunction with wavelength selective FBGs to demonstrate ultra-short wavelength operation in the 1620–1660 nm region, owing to a blue-shifted operation window in the Tm/Ge co-doped fibre [43]. Irrespective of the low output power (<22 dBm) and low efficiency (~6%) reported in this work, there shows scope for achieving higher output power in this waveband by optimising the fibre glass composition and the laser configuration. The scheme of our gain-switched diode-seeded MOPA at 1.95 µm can be easily transferred to this wavelength range (1.65–1.75 µm) by changing the seed wavelength and optimising the gain fibre length.

List of References

[1] P. B. Mauer, "Laser Action in Neodymium-Doped Glass at 1.37 Microns," *Appl. Opt.* **3**(1), 153-153 (1964).

[2] H. W. Gandy, R. Ginther and J.Weller, "Laser oscillations in erbium activated silicate glass," *Phys. Lett.* **16**(3), 266-267 (1965).

[3] H. W. Gandy, R. J. Ginther and J. F. Weller, "Stimulated emission of Tm^{3+} radiation in silicate glass," *J. Appl. Phys.* **38**(7), 3030-3031 (1967).

[4] C. J. Koester and E. Snitzer, "Amplification in a fiber laser," *Appl. Opt.* **3**(10), 1182-1186 (1964).

[5] D. J. Richardson, J. Nilsson and W. A. Clarkson, "High power fiber lasers: current status and future perspectives," *J. Opt. Soc. Am. B* **27**(11), B63-B92 (2010).

[6] J. Hecht, "Photonic Frontiers: Fiber Lasers: Novel fiber lasers offer new capabilities," *LaserFocusWorld* **50**(5) (2015).

[7] K. Scholle, S. Lamrini, P. Koopmann and P. Fuhrberg, "2 µm laser sources and their possible applications," in *Frontiers in Guided Wave Optics and Optoelectronic*, InTech (2010).

[8] S. D. Jackson, "Towards high-power mid-infrared emission from a fiber laser," *Nat. Photonics* **6**(7), 423-431 (2012).

[9] G. Stevens and A. Robertson, "Fibre laser component technology for 2-micron laser systems," Proc. SPIE **9135**, 91350N (2014).

[10] A. Sincore, J. D. Bradford, J. Cook, L. Shah and M. C. Richardson, "High average power thulium-doped silica fiber lasers: Review of systems and concepts," *IEEE J. Sel. Top. Quantum. Electron.* **24**(3), 1-8 (2018).

[11] T. Ehrenreich, R. Leveille, I. Majid, K. Tankala, G. Rines and P. Moulton, "1-kW, all-glass Tm: Fiber laser," Proc. SPIE **7580**, 758016 (2010).

[12] T. S. McComb, R. A. Sims, C. Willis, P. Kadwani, V. Sudesh, L. Shah and Martin Richardson, "High-power widely tunable thulium fiber lasers," *Appl. Opt.* **49**(32), 6236-6242 (2010).

List of References

[13] K. Yin, R. Zhu, B. Zhang, G. Liu, P. Zhou and J. Hou, "300 W-level, wavelength-widely-tunable, all-fiber integrated thulium-doped fiber laser," *Opt. Express* **24**(10), 11085-11090 (2016).

[14] X. Wang, X. Jin, P. Zhou, X. Wang, H. Xiao and Z. Liu, "High power, widely tunable, narrowband superfluorescent source at 2 µm based on a monolithic Tm-doped fiber amplifier," *Opt. Express* **23**(3), 3382-3389 (2015).

[15] J. Liu, H. Shi, Chen Liu, and Pu Wang, "Widely-tunable high-power narrow-linewidth thulium-doped all-fiber superfluorescent source," in Conference on Lasers and Electro-Optics, pp.1-2 (2015).

[16] M. Eichhorn and S. D. Jackson, "High-pulse-energy actively Q-switched Tm^{3+}-doped silica 2 µm fiber laser pumped at 792 nm," *Opt. Lett.* **32**(19), 2780-2782 (2007).

[17] Y. Tang, L. Xu, Y. Yang and J. Xu, "High-power gain-switched Tm^{3+}-doped fiber laser," *Opt. Express* **18**(22), 22964-22972 (2010).

[18] Z. Li, A. M. Heidt, P. S. Teh, M. Berendt, J.K. Sahu, R. Phelan, B. Kelly, S. U. Alam and D. J. Richardson, "High-energy diode-seeded nanosecond 2 µm fiber MOPA systems incorporating active pulse shaping," *Opt. Lett.* **39**(6), 1569-1572 (2014).

[19] X. Wang, X. Jin, P. Zhou, X. Wang, H. Xiao and Z. Liu, "All-fiber high-average power nanosecond-pulsed master-oscillator power amplifier at 2 µm with mJ-level pulse energy," *Appl. Opt.* **55**(8), 1941-1945 (2016).

[20] L. Li, B. Zhang, K. Yin, L. Yang and J. Hou, "1 mJ nanosecond all-fiber thulium-doped fiber laser at 2.05 µm," *Opt. Express* **23**(14), 18098-18105 (2015).

[21] J. Yang, Y. Wang, G. Zhang, Y. Tang and J. Xu, "High-power highly linear-polarized nanosecond all-fiber MOPA at 2040 nm," *IEEE Photonics. Technol. Lett.*, **29**(9) 986-989 (2015).

[22] C. Gaida, M. Gebhardt, P. Kadwani, L. Leick, J. Broeng, L. Shah and M. Richardson, "Amplification of nanosecond pulses to megawatt peak power levels in Tm^{3+}-doped photonic crystal fiber rod," *Opt. Lett.* **38**(5), 691-693 (2013).

[23] G. Imeshev and M. E. Fermann, "230-kW peak power femtosecond pulses from a high power tunable source based on amplification in Tm-doped fiber," *Opt. Express* **13**(19), 7424-7431 (2005).

[24] D. Strickland and G. Mourou, "Compression of amplified chirped optical pulses," *Opt. Commun.* **55**(6), 447-449 (1985).

[25] P. Wan, L. Yang and J. Liu, "156 micro-J ultrafast Thulium-doped fiber laser," in SPIE Photonics West, pp. 8601-117 (2013).

[26] M. Gebhardt, C. Gaida, F. Stutzki, S. Hädrich, C. Jauregui, J. Limpert and A. Tünnermann, "High average power nonlinear compression to 4 GW, sub-50 fs pulses at 2 µm wavelength," *Opt. Lett.* **42**(4), 747-750 (2017).

[27] F. Stutzki, C. Gaida, M. Gebhardt, F. Jansen, A. Wienke, U. Zeitner, F. Fuchs, C. Jauregui, D. Wandt, D. Kracht, J. Limpert and A. Tünnermann, "152 W average power Tm-doped fiber CPA system," *Opt. Lett.* **39**(16), 4671-4674 (2014).

[28] P. Hübner, C. Kieleck, S. D. Jackson and M. Eichhorn, "High-power actively mode-locked sub-nanosecond Tm^{3+}-doped silica fiber laser," *Opt. Lett.* **36**(13), 2483-2485 (2011).

[29] J. Liu, Q. Wang and P. Wang, "High average power picosecond pulse generation from a thulium-doped all-fiber MOPA system," *Opt. Express* **20**(20), 22442-22447 (2012).

[30] A. M. Heidt, Z. Li and D. J. Richardson, "High Power Diode-Seeded Fiber Amplifiers at 2 µm – From Architectures to Applications," *IEEE J. Sel. Top. Quantum Electron.* **20**(5), 525-536 (2014).

[31] S. Guillemet, Y. Hernandez, D. Mortag, F. Haxsen, A. Wienke, D. Wandt, L. Leick, and W. Richter, "High energy sub-nanosecond thulium-doped all-fibre laser based on a rod-type photonic-crystal fibre amplifier," in Advanced Solid State Lasers, paper ATh2A.27 (2015).

[32] J. Liu, C. Liu, H. Shi, and P. Wang, "High-power linearly-polarized picosecond thulium-doped all-fiber master-oscillator power-amplifier," *Opt. Express* **24**(13), 15005-15011 (2016).

[33] S. Ishii, K. Mizutani, H. Fukuoka, T. Ishikawa, B. Philippe, H. Iwai, T. Aoki, T. Itabe, A. Sato, and K. Asai, "Coherent 2 micron differential absorption and wind lidar with conductively cooled laser and two-axis scanning device," *Appl. Opt.* **49**(10), 1809-1817 (2010).

[34] I. Mingareev, F. Weirauch, A. Olowinsky, L. Shah, P. Kadwani, and M. Richardson, "Welding of polymers using a 2µm thulium fiber laser," *Optics & Laser Technol.* **44**(7), 2095-2099 (2012).

[35] N. M. Fried and K. E. Murray, "High-power thulium fiber laser ablation of urinary tissues at 1.94 µm," *Journal of endourology* **19**(1), 25-31 (2005).

List of References

[36] L. Xu, Q. Fu, S. Liang, D. P. Shepherd, D. J. Richardson, and S.-U. Alam, "Thulium-fiber-laser-pumped, high-peak-power, picosecond, mid-infrared orientation-patterned GaAs optical parametric generator and amplifier," *Opt. Lett.* **42**(19), 4036-4039 (2017).

[37] A. M. Heidt, J. H. V. Price, C. Baskiotis, J. S. Feehan, Z. Li, S. U. Alam, and D. J. Richardson, "Mid-infrared ZBLAN fiber supercontinuum source using picosecond diode-pumping at 2 μm," *Opt. Express* **21**(20), 24281-24287 (2013).

[38] J. P. Cariou, B. Augere and M. Valla, "Laser source requirements for coherent lidars based on fiber technology," *Comptes Rendus Physique* **7**(2), 213-223 (2006).

[39] D. J. Richardson, "Filling the Light Pipe," *Science* **330**(6002), 327–328 (2010).

[40] Z. Li, A. M. Heidt, N. Simakov, Y. Jung, J. M. O. Daniel, S. U. Alam and D. J. Richardson, "Diode-pumped wideband thulium-doped fiber amplifiers for optical communications in the 1800 – 2050 nm window," *Opt. Express* **21**(22), 26450–26455 (2013).

[41] Z. Li, S. U. Alam, J. M. O. Daniel, P. C. Shardlow, D. Jain, N. Simakov, A. M. Heidt, Y. Jung, J. K. Sahu, W. A. Clarkson, and D. J. Richardson, "90 nm Gain Extension Towards 1.7 μm for Diode-Pumped Silica-Based Thulium-Doped Fiber Amplifiers," in Proc. ECOC, p. Tu.3.4.2 (2014).

[42] Z. Li, Y. Jung, J. M. O. Daniel, N. Simakov, P. C. Shardlow, A. M. Heidt, W. A. Clarkson, S. U. Alam, and D. J. Richardson, "Extreme short wavelength operation (1.65–1.7 μm) of silica-based Thulium-doped fiber amplifier," in Optical Fiber Communication Conference, pp. Tu2C-1 (2015).

[43] S. Chen, Y. Jung, S. U. Alam, S. Jain, M. Ibsen, R. Sidharthan, D. Ho, S. Yoo and David J. Richardson, "Ultra-short Wavelength Operation of a Thulium Doped Fiber Laser in the 1620–1660nm Wavelength Band," In IEEE Optical Fiber Communications Conference and Exposition, pp.1-3 (2018).

[44] W. Yang, B. Zhang, K. Yin, X. Zhou and J. Hou, "High power all fiber mid-IR supercontinuum generation in a ZBLAN fiber pumped by a 2 μm MOPA system," *Opt. Express* **21**(17), 19732-19742 (2013).

[45] J. Swiderski, M. Michalska, C. Kieleck, M. Eichhorn and Gwenael Maze, "High Power Supercontinuum Generation in Fluoride Fibers Pumped by 2 μm Pulses," *IEEE Photonics Technol. Lett.* **26**(2), 150-153 (2014).

[46] K. Yin, B. Zhang, L. Yang and J. Hou, "15.2 W spectrally flat all-fiber supercontinuum laser source with> 1 W power beyond 3.8 μm," *Opt. Lett.* **42**(12), 2334-2337 (2017).

[47] J. Swiderski, "High-power mid-infrared supercontinuum sources: current status and future perspectives," *Progress in Quantum Electronics* **38**(5), 189-235 (2014).

[48] F. K. Tittel, "Mid-IR semiconductor lasers enable sensors for trace-gas-sensing applications," *Photonics Spectra*, 52-56 (2014).

[49] C. L. Hagen, J. W. Walewski and S. T. Sanders, "Generation of a continuum extending to the midinrared by pump ZBLAN fiber with an ultrafast 1550-nm source," *IEEE Phtonics Technol. Lett.* **18**(1), 91-93 (2006).

[50] C. Xia, Z. Xu, M. N. Islam, F. L. Terry Jr., M. J. Freeman, A. Zakel and J. Mauricio, "10.5 W Time-Averaged Power Mid-IR Supercontinuum Generation Extending Beyond 4µm With Direct Pulse Pattern Modulation," *IEEE J. Sel. Top. Quantum. Electron* **15**(2), 422-434 (2009).

[51] K. Liu, J. Liu, H. Shi, F. Tan and P. Wang, "High power mid-infrared supercontinuum generation in a single-mode ZBLAN fiber with up to 21.8 W average output power," *Opt. Express* **22**(20), 24384-24391 (2014).

[52] P. Moselund, C. Petersen, L. Leick, J. S. Dam, P. T. Lichtenberg and C. Pedersen, "Highly Stable, All-fiber, High Power ZBLAN Supercontinuum Source Reaching 4.75 µm used for Nanosecond mid-IR Spectroscopy," In Mid-Infrared Coherent Sources, pp. JTh5A-9 (2013).

[53] F. Théberge, J. Daigle, D. Vincent, P. Mathieu, J. Fortin, B. E. Schmidt, N. Thiré and F. Légaré, "Mid-infrared supercontinuum generation in fluoroindate fiber," *Opt. Lett.* **38**(22), 4683-4685 (2013).

[54] J. C. Gauthier, V. Fortin, J. Y. Carrée, S. Poulain, M. Poulain, R. Vallée, and M. Bernier, "Mid-IR supercontinuum from 2.4 to 5.4 µm in a low-loss fluoroindate fiber," *Opt. Lett.* **41**(8), 1756-1759 (2016).

[55] M. Michalska, J. Mikolajczyk, J. Wojtas and J. Swiderski, "Mid-infrared, super-flat, supercontinuum generation covering the 2-5µm spectral band using a fluoroindate fibre pumped with picosecond pulses," *Sci. Rep.* **6**, 39138 (2016).

[56] G.P. Agrawal, *Fiber-optic communication systems (3rd edition)*, John Wiley & Sons, 2012.

[57] M. Born and E. Wolf, *Principles of Optics (7th edition)*, Cambridge University Press, 1999.

List of References

[58] D. K. Mynbaev and L. L. Scheiner, *Fiber-Optic Communications Technology*, Prentice Hall, 2001.

[59] G.P. Agrawal, *Nonlinear Fiber Optics (5th edition)*, Academic Press, 2013.

[60] Y. Chen, S. Raghuraman, D. Ho, D. Tang and S. Yoo, "Normal dispersion thulium fiber for ultrafast near-2 µm fiber laser," in Conference on Lasers and Electro-Optics, paper AM2M.2 (2018).

[61] Y. Chen, S. Chen, K. Liu, Q. Wang, D. Tang and S. Yoo, "All-Fiber 2 µm Amplifier Using a Normal Dispersion Thulium Fiber," in Conference on Lasers and Electro-Optics, paper ATu4I.6 (2019).

[62] S. D. Jackson, "The spectroscopic and energy transfer characteristics of the rare earth ions used for silicate glass fibre lasers operating in the shortwave infrared," *Laser & Photonics Reviews* **3**(5), 466-482 (2009).

[63] D. A. Simpson, *Spectroscopy of Thulium Doped Silica Glass*, PhD thesis, Victoria University, 2008.

[64] P. Peterka, I. Kasik, A. Dhar, B. Dussardier and Wilfried Blanc, "Theoretical modeling of fiber laser at 810 nm based on thulium-doped silica fibers with enhanced $^3H_4$ level lifetime," *Opt. Express* **19**(3), 2773-2781 (2011).

[65] E. Desurvire, *Erbium-Doped Fiber Amplifiers: Principles and Applications*, Wiley, 1994.

[66] G. Frith, B. Samson, A. Carter, J. Farroni, and K. Tankala, "High power, high efficiency monolithic FBG based fiber laser operating at 2 µm," In Proc. SPIE **6453**, p. 64532B (2007).

[67] S.D. Jackson, "Cross relaxation and energy transfer upconversion processes relevant to the functioning of 2 µm Tm^{3+}-doped silica fibre lasers," *Opt. Commun.* **230**(1-3), 197-203 (2004).

[68] S. D. Jackson and S. Mossman, "Efficiency dependence on the Tm^{3+} and Al^{3+} concentrations for Tm^{3+}-doped silica double-clad fiber lasers," *Appl. Opt.* **42**(15), 2702-2707 (2003).

[69] P. C. Becker, N. A. Olsson and J. R. Simpson, *Erbium-Doped Fiber Amplifier – Fundamentals and Technology*, Academic Press, 1999.

[70] M. A. Khamis and K. Ennser, "Theoretical Model of a Thulium-Doped Fiber Amplifier Pumped at 1570 nm and 793 nm in the Presence of Cross Relaxation," *J. Light. Technol.* **34**(24), 5675-5681 (2016).

[71] https://www.fiberlabs-inc.com/glossary/core-pumping-and-cladding-pumping/

[72] E. Snitzer, H. Po, F. Hakimi, R. Tumminelli and B. B. McCollum, "Double-clad, offset core Nd fiber laser," in Optical Fiber Sensors, paper PD5 (1988).

[73] S. Saraf, K. Urbanek and R. L. Byer, "Quantum noise measurements in a continuous-wave laser-diode-pumped Nd:YAG saturated amplifier," *Opt. Lett.* **3**(10), 1195-1197 (2005).

[74] S. Kharitonov, A. Billat and C. S. Brès, "Kerr nonlinearity and dispersion characterization of core-pumped thulium-doped fiber at 2 μm," *Opt. Lett.* **41**(14), 3173-3176 (2016).

[75] G. P. Agrawal, "Modulation instability in erbium-doped fiber amplifiers," *IEEE Photonics Technol. Lett.* **4**(6), 562-564 (1992).

[76] R. G. Smith, "Optical power handling capacity of low loss optical fibers as determined by stimulated Raman and Brillouin scattering," *Appl. Opt.* **11**(11), 2489-2494 (1972).

[77] R. R. Alfano and S. L. Shapiro, "Emission in the region 4000 to 7000 Å via four-photon coupling in glass," *Phys. Rev. Lett.* **24**(11), 584 (1970).

[78] C. Lin and R. H. Stolen, "New nanosecond continuum for excited-state spectroscopy," *Appl. Phys. Lett.* **28**(4), 216-218 (1976).

[79] J. M. Dudley and J. R. Taylor (Eds), *Supercontinuum generation in optical fibers*, Cambridge University Press, 2010.

[80] I. Basaldua, R. Kuis, P. Burkins, Z. Jiang and A. M. Johnson, "Measurements of the Nonlinear Refractive Index (n_2) for Indium Fluoride (InF_3) Bulk Glass and Fiber," in Frontiers in Optics / Laser Science, paper JTu3A.38 (2018).

[81] R. W. Boyd, *Nonlinear Optics (3rd edition)*, Academic Press, 2008.

[82] G. New, *Introduction to Nonlinear Optics*, Cambridge University Press, 2011.

[83] https://www.covesion.com/support/covesion-guide-to-ppln/principles-of-nonlinear-frequency-conversion.html

List of References

[84] https://refractiveindex.info/?shelf=main&book=GaAs&page=Skauli

[85] K. L. Vodopyanov, O. Levi, P. S. Kuo, T. J. Pinguet, J. S. Harris, M. M. Fejer, B. Gerard, L. Becouarn and E. Lallier, "Optical parametric oscillation in quasi-phase-matched GaAs," *Opt. Lett.* **29**(16), 1912-1914 (2004).

[86] F. Stutzki, C. Gaida, M. Gebhardt, F. Jansen, C. Jauregui, J. Limpert and A. Tünnermann, "Tm-based fiber-laser system with more than 200 MW peak power," *Opt. Lett.* **40**(1), 9-12 (2015).

[87] A. M. Heidt, Z. Li, J. Sahu, P. C. Shardlow, M. Becker, M. Rothhardt, M. Ibsen, R. Phelan, B. Kelly, S. U. Alam and D. J. Richardson, "100 kW peak power picosecond thulium-doped fiber amplifier system seeded by a gain-switched diode laser at 2 μm," *Opt. Lett.* **38**(10), 1615-1617 (2013).

[88] K. Y. Lau, "Gain switching of semiconductor injection lasers," *Appl. Phys. Lett.* **52**(4), 257-259 (1988).

[89] D. M. Pataca, P. Gunning, M. L. Rocha, J. K. Lucek, R. Kashyap, K. Smith, D. G. Moodie, R. P. Davey, R. F. Souza and A. S. Siddiqui, "Gain-switched DFB lasers," *Journal of Microwaves, Optoelectronics and Electromagnetic Applications (JMOe)* **1**(1), 46-63 (1997).

[90] R. Phelan, J. O'Carroll, D. Byrne, C. Herbert, J. Somers and Brian Kelly, "In$_{0.75}$Ga$_{0.25}$As/InP Multiple Quantum-Well Discrete-Mode Laser Diode Emitting at 2 μm," *IEEE Photonics Technol. Lett.* **24**(8), 652-654 (2012).

[91] Z. Li, *Thulium-doped fiber sources for novel applications*, PhD thesis, University of Southampton, 2015.

[92] J. Lee, U. Ryu, S. J. Ahn and N. Park, "Enhancement of power conversion efficiency for an L-band EDFA with a secondary pumping effect in the unpumped EDF section," *IEEE Photonics Technol. Lett.* **11**(1), 42-44 (1999).

[93] http://leverrefluore.com/

[94] P. Horak, K. K. Chen, S. Alam, S. Dasgupta and D. J. Richardson, "High-Power Supercontinuum generation with picosecond pulses," in IEEE 12th International Conference on Transparent Optical Networks, pp. 1-4 (2010).

[95] F. M. Mitschke and L. F. Mollenauer, "Discovery of the soliton self-frequency shift," *Opt. Lett.* **11**(10), 659-661 (1986).

[96] S. Roy, S. K. Bhadra and Govind P. Agrawal, "Dispersive wave generation in supercontinuum process inside nonlinear microstructured fibre," *Current Science* **100**(3), 321-342 (2011).

[97] D. R. Austin, C. M. de Sterke, B. J. Eggleton and T. G. Brown, "Dispersive wave blue-shift in supercontinuum generation," *Opt. Express* **14**(25), 11997-12007 (2006).

[98] J. M. O. Daniel, N. Simakov, M. Tokurakawa, M. Ibsen and W. A. Clarkson, "Ultra-short wavelength operation of a thulium fibre laser in the 1660–1750 nm wavelength band," *Opt. Express* **23**(14), 18269-18276 (2015).

[99] J. Wang, S. Liang, Q. Kang, Y. Jung, S. Alam and D. J. Richardson, "Broadband silica-based thulium doped fiber amplifier employing multi-wavelength pumping," *Opt. Express* **24**(20), 23001-23008 (2016).

[100] E. J. Mayer, J. Möbius, A. Euteneuer, W. W. Rühle, and R. Szipőcs, "Ultrabroadband chirped mirrors for femtosecond lasers," *Opt. Lett.* **22**(8), 528-530 (1997).

[101] C. Canal, A. Laugustin, A. Kohl and O. Rabot, "Novel high-energy short-pulse laser diode source for 3D lidar systems," in Electro-Optical Remote Sensing XII **10796**, p. 1079605 (2018).

[102] R. Aviles-Espinosa, G. Filippidis, C. Hamilton, G. Malcolm, K. J. Weingarten, T. Südmeyer, Y. Barbarin, U. Keller, S. I.C.O Santos, D. Artigas and P. Loza-Alvarez, "Compact ultrafast semiconductor disk laser: targeting GFP based nonlinear applications in living organisms," *Biomed. Opt. Express* **2**(4), 739-747 (2011).

[103] R.D. Niederriter, B. N. Ozbay, G. L. Futia, E. A. Gibson and Juliet T. Gopinath, "Compact diode laser source for multiphoton biological imaging," *Biomed. Opt. Express* **8**(1), 315-322 (2017).

[104] A. Klehr, H. Wenzel, J. Fricke, F. Bugge, A. Liero, Th Hoffmann, G. Erbert and G. Tränkle, "Generation of spectrally-stable continuous-wave emission and ns pulses at 800 nm and 975 nm with a peak power of 4 W using a distributed Bragg reflector laser and a ridge-waveguide power amplifier," in Novel In-Plane Semiconductor Lasers XIV **9382**, p. 93821I (2015).

[105] R. Selvas, J. K. Sahu, L. B. Fu, J. N. Jang, J. Nilsson, A. B. Grudinin, K. H. Ylä-Jarkko, S. Alam, P. W. Turner and J. Moore, "High-power, low-noise, Yb-doped, cladding-pumped, three-level fiber sources at 980nm," *Opt. Lett.* **28**(13), 1093-1095 (2003).

List of References

[106] J. Boullet, Y. Zaouter, R. Desmarchelier, M. Cazaux, F. Salin, J. Saby, R. Bello-Doua and Eric Cormier, "High power ytterbium-doped rod-type three-level photonic crystal fiber laser," *Opt. Express* **16**(22), 17891-17902 (2008).

[107] D. Creeden, D. Creeden, J. Blanchard, J. Blanchard, H. Pretorius, H. Pretorius, J. Limongelli, J. Limongelli, Scott D. Setzler AND Scott D. Setzler, "486nm blue laser operating at 500 kHz pulse repetition frequency," in Proc. SPIE **9728**, pp. 972829 (2016).

[108] https://www.rp-photonics.com/argon_ion_lasers.html

[109] https://www.rp-photonics.com/blue_lasers.html?s=ak

[110] L. E. Myers, "Review of quasi-phasematching and periodically poled lithium niobate," in Proceedings of the IEEE National Aerospace and Electronics Conference, pp. 733-739 (1996).

[111] D. S.Hum, M. M. Fejer, "Quasi-phasematching," *Comptes Rendus Physique* **8**(2), 180-198 (2006).

[112] J. A. Armstrong, "Interactions between light waves in a nonlinear dielectric," *Phys. Rev.* **127**(6), 1918 (1962).

[113] G. D. Miller, *Periodically Poled Lithium Niobate: Modeling, Fabrication, and Nonlinear-Optical performance*, PhD thesis, Stanford University, 1998.

[114] H. Chan, *Novel Systems via Nonlinear Frequency Conversion of Fibre-Amplified Ultrafast Semiconductor Lasers*, PhD thesis, University of Southampton, 2016.

[115] https://www.covesion.com/support/covesion-guide-to-ppln/how-to-use-ppln.html

[116] A. Ashkin, G. D. Boyd, J. M. Dziedzic, R. G. Smith, A. A. Ballman, J. J. Levinstein and K. Nassau, "Optically-induced refractive index inhomogeneities in $LiNbO_3$ and $LiTaO_3$," *Appl. Phys. Lett.* **9**(1), 72–74 (1966).

[117] F. Jermann, M. Simon and E. Krätzig, "Photorefractive properties of congruent and stoichiometric lithium niobate at high light intensities," *J. Opt. Soc. Am. B* **12**(11), 2066–2070 (1995).

[118] Y. Furukawa, K. Kitamura, A. Alexandrovski, R. K. Route, M. M. Fejer and G. Foulon, "Green-induced infrared absorption in MgO doped $LiNbO_3$," *Appl. Phys. Lett.* **78**(14), 1970–1972 (2001).

[119] L. E. Myers, R. C. Eckardt, M. M. Fejer, R. L. Byer, W. R. Bosenberg and J. W.Pierce, "Quasi-phase-matched optical parametric oscillators in bulk periodically poled LiNbO₃," *J. Opt. Soc. Am. B* **12**(11), 2102–2116 (1995).

[120] T. Andres, P. Haag, S. Zelt, J. P. Meyn, A. Borsutzky, R. Beigang, and R. Wallenstein, "Synchronously pumped femtosecond optical parametric oscillator of congruent and stoichiometric MgO-doped periodically poled lithium niobate," *Appl. Phys. B* **76**(3), 241–244 (2003).

[121] D. H. Jundt, "Temperature-dependent Sellmeier equation for the index of refraction, ne, in congruent lithium niobate," *Opt. Lett.* **22**(20), 1553-1555 (1997).

[122] R. Eckardt and J. Reintjes, "Phase matching limitations of high efficiency second harmonic generation," *IEEE J. Quantum Electron.* **20**(10), 1178-1187 (1984).

[123] K. R. Parameswaran, J. R. Kurz, R. V. Roussev and M. M. Fejer, "Observation of 99% pump depletion in single-pass second-harmonic generation in a periodically poled lithium niobate waveguide," *Opt. Lett.* **27**(1), 43-45 (2002).

[124] O. Gayer, Z. Sacks, E. Galun and A. Arie, "Temperature and wavelength dependent refractive index equations for MgO-doped congruent and stoichiometric LiNbO₃," *Appl. Phys. B* **91**(2), 343-348 (2008).

[125] P. G. Schunemann, "New Nonlinear Optical Crystals for the Mid-Infrared," in Advanced Solid State Lasers, paper AM2A.2 (2015).

[126] R. Demur, A. Grisard, E. Lallier, L. Morvan, N. Treps and C. Fabre, "High sensitivity mid-infrared detection at room temperature by upconversion in orientation-patterned GaAs," in Conference on Lasers and Electro-Optics Europe & European Quantum Electronics Conference, pp. 1-1 (2017).

[127] L. Maidment, P. G. Schuneman and D. T. Reid, "Molecular fingerprint-region spectroscopy from 5 to 12 μm using an orientation-patterned gallium phosphide optical parametric oscillator," *Opt. Lett.* **41**(18), 4261-4264 (2016).

[128] F.K. Tittel, D. Richter and A. Fried, "Mid-Infrared Laser Applications in Spectroscopy," *Solid-State Mid-Infrared Laser Sources* **89**, 458-529 (2003).

[129] J. Wueppen, S. Nyga, B. Jungbluth and Dieter Hoffmann, "1.95 μm-pumped OP-GaAs optical parametric oscillator with 10.6 μm idler wavelength," *Opt. Lett.* **41**(18), 4225-4228 (2016).

List of References

[130] O.H. Heckl, B. J. Bjork, G. Winkler, P. B. Changala, B. Spaun, G. Porat, T. Q. Bui, K. F. Lee, J. Jiang, M. E. Fermann, P. G. Schunemann and Jun Ye, "Three-photon absorption in optical parametric oscillators based on OP-GaAs," Opt. Lett. 41(22), 5405-5408 (2016).

[131] G. Bloom, A. Grisard, E. Lallier, C. Larat, M. Carras and X. Marcadet, "Optical parametric amplification of a distributed feedback quantum cascade laser in orientation-patterned GaAs," in Conference on Lasers and Electro-Optics, paper CFN1 (2010).

[132] F. Gutty, A. Grisard, C. Larat, D. Papillon, M. Schwarz, B. Gérard, R. Ostendorf, M. Rattunde, J. Wagner and Eric Lallier, "100 W-level peak-power laser system tunable from 8 to 10 μm," in Lasers and Electro-Optics Europe & European Quantum Electronics Conference, pp. 1-1 (2017).

[133] C. Kieleck, M. Eichhorn, A. Hirth, D. Faye and E. Lallier, "High-efficiency 20–50 kHz mid-infrared orientation-patterned GaAs optical parametric oscillator pumped by a 2 μm holmium laser," *Opt. Lett.* **34**(3), 262-264 (2009).

[134] W. C. Hurlbut, Yun-Shik Lee, K. L. Vodopyanov, P. S. Kuo, and M. M. Fejer, "Multiphoton absorption and nonlinear refraction of GaAs in the mid-infrared," *Opt. Lett.* **32**(6), 668-670 (2007).

[135] P. S. Kuo, K. L. Vodopyanov, M. M. Fejer, X. Yu, A. C. Lin, J. S. Harris, D. F. Bliss and Candace L. Lynch, "GaAs Optical Parametric Oscillator with a Circularly Polarized Pump," In Conference on Lasers and Electro-Optics, p. CMJ2 (2007).

[136] L. Xu, H.-Y. Chan, S.-U. Alam, D. J. Richardson, and D. P. Shepherd, "Fiber-laser-pumped, high-energy, mid-IR, picosecond optical parametric oscillator with a high-harmonic cavity," *Opt. Lett.* **40**(14), 3288-3291 (2015).

[137] J. Prawiharjo, H. S. S. Hung, D. C. Hanna and D. P. Shepherd, "Theoretical and numerical investigations of parametric transfer via difference-frequency generation for indirect mid-infrared pulse shaping," *J. Opt. Soc. Am. B* **24**(4), 895-905 (2007).

[138] F. B. Slimen, S. Chen, J. Lousteau, Y. Jung, S. Alam, N. White, D. Richardson and F. Poletti, "Tm^{3+} Doped Germanate Large Mode Area Single Mode Fiber for 2 μm Lasers and Amplifiers," in Specialty Optical Fibers, pp. SoTu4H-2 (2018).

[139] C. Yang, D. Chen, S. Xu, H. Deng, W. Lin, Q. Zhao, Y. Zhang, K. Zhou, Z. Feng, Q. Qian and Z. Yang, "Short all Tm-doped germanate glass fiber MOPA single-frequency laser at 1.95 μm," *Opt. Express* **24**(10), 10956-10961 (2016).

[140] J. Wu, Z. Yao, J.Zong and S. Jiang, "Highly efficient high-power thulium-doped germanate glass fiber laser," *Opt. Lett.* **32**(6), 638-640 (2007).

[141] J. Geng, J. Wu, S. Jiang and J. Yu, "Efficient operation of diode-pumped single-frequency thulium-doped fiber lasers near 2 μm," *Opt. Lett.* **32**(4), 355-357 (2007).

[142] X. He, S. Xu, C. Li, C. Yang, Q. Yang, S. Mo, D. Chen and Z. Yang, "1.95 μm kHz-linewidth single-frequency fiber laser using self-developed heavily Tm^{3+}-doped germanate glass fiber," *Opt. Express* **21**(18), 20800-20805 (2013).

[143] X. Guan, C. Yang, T. Qiao, W. Lin, Q. Zhao, G. Tang, G. Qian, Q. Qian, Z. Yang and S. Xu, "High-efficiency sub-watt in-band-pumped single-frequency DBR Tm^{3+}-doped germanate fiber laser at 1950 nm," *Opt. Express* **26**(6), 6817-6825 (2018).

[144] N. P. Barnes, B. M. Walsh, D. J. Reichle and S. Jiang, "Tuning And Q-switching Tm:germanate Fiber Laser," in Advanced Solid-State Photonics, paper WB8 (2007).

[145] C. Baskiotis, A. M. Heidt, S. Alam and D. J. Richardson, "LMA effectively single-mode thulium doped fibre with normal dispersion at wavelengths around 2um," in Conference on Lasers & Electro-Optics Europe & International Quantum Electronics Conference, pp. 1-1 (2013).

[146] D. Y. Shen, J. K. Sahu and W. A. Clarkson, "High-power widely tunable Tm:fibre lasers pumped by an Er,Yb co-doped fibre laser at 1.6μm," *Opt. Express* **14**(13), 6084-6090 (2006).

[147] S. Chen, Y. Jung, S. Alam, J. Wang, R. Sidharthan, D. Ho, S. Jain, S. Yoo and D. J. Richardson, "Ultra-wideband Operation of a Tunable Thulium Fibre Laser offering Tunability from 1679–1992 nm," in European Conference on Optical Communication, pp. 1-3 (2017).

[148] J. W. Jr and L. Weyer, *Practical Guide and Spectral Atlas for Interpretive Near-Infrared Spectroscopy*, CRC Press, 2012.

[149] V. V. Alexander, K. Ke, Z. Xu, M. N. Islam, M. J. Freeman, B. Pitt, M. J. Welsh, and J. S. Orringer, "Photothermolysis of sebaceous glands in human skin ex vivo with a 1,708nm Raman fiber laser and contact cooling," *Lasers Surg. Med.* **43**(6), 470–480 (2011).

List of Publications

Journal Publications

1. <u>S. Liang</u>, L. Xu, Q. Fu, Y. Jung, D. P. Shepherd, D. J. Richardson and S. Alam, "295-kW peak power picosecond pulses from a thulium-doped-fiber MOPA and the generation of watt-level >2.5-octave supercontinuum extending up to 5 µm," *Opt. Express*, **26**(6), 6490-6498 (2018).

2. L. Xu, <u>S. Liang</u>, Q. Fu, D. P. Shepherd, D. J. Richardson and S.Alam, "Highly efficient frequency doubling and quadrupling of a short-pulsed thulium fiber laser," *Appl. Phys. B*, **124**(4), 59 (2018).

3. Q. Fu, L. Xu, <u>S. Liang</u>, D. P. Shepherd, D. J. Richardson and S. Alam, "Widely Tunable, Narrow-Linewidth, High-Peak-Power, Picosecond Midinfrared Optical Parametric Amplifier," *IEEE J. Sel. Top. Quantum. Electron.*, **24**(5), 1-6 (2018).

4. L. Xu, Q.Fu, <u>S. Liang</u>, D. P. Shepherd, D. J. Richardson and S. Alam, "Thulium-fiber-laser-pumped, high-peak-power, picosecond, mid-infrared orientation-patterned GaAs optical parametric generator and amplifier," *Opt. Lett.*, **42**(19), 4036-4039 (2017).

5. K. Sharma, <u>S. Liang</u>, S. Alam, S. Bhattacharya, D. Venkitesh and G. Brambilla, "Fiber-Based Cavity Ring-Down Technique for Refractive Index Sensing at 1953nm Using Tapered Fibers," *IEEE sensors letters*, **1**(3), 1-4 (2017).

6. N. V. Wheeler, T. D. Bradley, J. R. Hayes, M. A. Gouveia, <u>S. Liang</u>, Y. Chen, S. R. Sandoghchi, S. M. Abokhamis Mousavi, F. Poletti, M. N. Petrovich and D. J. Richardson, "Low-loss Kagome hollow-core fibers operating from the near- to the mid-IR," *Opt. Lett.*, **42**(13), 2571-2574 (2017).

7. J. Wang, <u>S. Liang</u>, Q. Kang, Y. Jung, S. Alam and David J. Richardson, "Broadband silica-based thulium doped fiber amplifier employing multi-wavelength pumping," *Opt. Express* **24**(20), 23001-23008 (2016).

8. N. Simakov, Z. Li, Y. Jung, J. M. O. Daniel, P. Barua, P. C. Shardlow, <u>S. Liang</u>, J. K. Sahu, A. Hemming, W. A.Clarkson, S. Alam and D. J. Richardson, "High gain holmium-doped fibre amplifiers," *Opt. Express*, **24**(13), 13946-13956 (2016).

Conference Publications

1. <u>S. Liang</u>, L. Xu, Q. Fu, D. P. Shepherd, D. J. Richardson and S. Alam, "A watt-level supercontinuum source from a fiber-laser-pumped fluoroindate fiber spanning 750 nm to 5 μm," in Conference on Lasers and Electro-Optics (Optical Society of America, 2018), paper. SM4K.2.

2. L. Xu, <u>S. Liang</u>, Q. Fu, D. P. Shepherd, D. J. Richardson and S. Alam, "High-peak-power, high-efficiency, frequency doubled and quadrupled Thulium fiber laser," in Conference on Lasers and Electro-Optics (Optical Society of America, 2018), paper. SM4K.5.

3. Q. Fu, L. Xu, <u>S. Liang</u>, D. P. Shepherd, D. J. Richardson and S. Alam, "Picosecond fiber-laser-pumped widely tunable, narrow-linewidth, high-peak-power, mid-infrared OP-GaAs OPA," in Conference on Lasers and Electro-Optic (Optical Society of America, 2018), paper STh3F.2.

4. J. H. Price, <u>S. Liang</u>, L. Xu, Q. Fu, Y. Jung, K. P. Herdzik, S. Mahajan, D. P. Shepherd, D. J. Richardson and S. Alam, "The Development of Tailored Supercontinuum Sources in Silica and Non-silica Fibers," in Conference on Lasers and Electro-Optic (Optical Society of America, 2018), paper. ATu3S.3.

5. L. Xu, Q. Fu, <u>S. Liang</u>, D. P. Shepherd, D. J. Richardson and S. Alam, "High-peak-power, picosecond, mid-infrared optical parametric generator and amplifier pumped by Tm: fiber laser." In Mid-Infrared Coherent Sources (Optical Society of America, 2018), pp. MW1C.3.

6. <u>S. Liang</u>, L. Xu, Q. Fu, Y. Jung, D. P. Shepherd, D. J. Richardson and S. Alam, "High peak power picosecond pulses from an all-fiber master oscillator power amplifier seeded by a 1.95 μm gain-switched diode," In Advanced Solid State Lasers (Optical Society of America, 2017), paper. ATh3A.4.

7. J. Wang, <u>S. Liang</u>, Y. Jung, Q. Kang, S. Alam, and D. J. Richardson, "Broadband Silica-Based Thulium Doped Fiber Amplifier Employing Dual-Wavelength Pumping," in Conference on Lasers and Electro-Optics (Optical Society of America, 2016), paper SM1Q.2.

List of Accompanying Materials

Dataset for this PhD thesis can be found by https://doi.org/10.5258/SOTON/D1018.